FİZİK

Editör: Dr.Öğr.Üyesi Esra UYAR

yaz
yayınları

FİZİK

Editör

Dr. Öğr. Üyesi Esra UYAR

yaz yayınları

2024

yaz
yayınları

FİZİK

Editör: Dr. Öğr. Üyesi Esra UYAR

E_ISBN 978-625-6104-45-7

Ekim 2024 – Afyonkarahisar

Dizgi/Mizanpaj: YAZ Yayınları

Kapak Tasarım: YAZ Yayınları

YAZ Yayınları. Yayıncı Sertifika No: 73086

M.İhtisas OSB Mah. 4A Cad. No:3/3
İscehisar/AFYONKARAHİSAR

www.yazyayinlari.com

yazyayinlari@gmail.com

info@yazyayinlari.com

İÇİNDEKİLER

DIFFERENTIAL SCANNING CALORIMETRY: APPLICATIONS IN DRUG-MEMBRANE INTERACTIONS

Züleyha ÖZÇELİK ÇETİNEL[1]

1. INTRODUCTION

Calorimetry represents one of the most significant techniques for the measurement of thermal phenomena. It is the principal technique employed to ascertain the thermal characteristics of constituents, thereby establishing a correlation connecting temperature and the certain physical assets of materials. Furthermore, it is the sole technique by which the enthalpy linked with the method of interest can be directly determined (Privalov and Potekhin,1986; Hohne et al., 1996).

Calorimeters are a common tool in a number of scientific disciplines, including chemistry, biochemistry, cell biology, biotechnology, and pharmacology. Just, they have also been employed in nanoscience, where they are used to quantify the thermodynamic properties of biomolecules and nano-sized objects (Even et al.,1997; Lin et al.,1993; Protasevich et al.,1997; Ladbury and Chowdhry,1996; Von Stockar and Marison, 2005; Weber and Salemme, 2003; Varhese et al.,2008).

Among the various types of calorimeters, differential scanning calorimetry (DSC) is a particularly popular one. A DSC is a thermal analysis instrument that is used to measure the physical characteristics of a given sample as a function of time

[1] Dr., Ege Üniversitesi Fen Fakültesi Fizik Bölümü, zuleyhaozcelikcetinel@gmail.com, ORCID: 0000-0001-7811-6183.

and temperature. In essence, the instrument is a device used to analyse thermal properties and heat transfer characteristics of a material undergoing phase transitions, providing data on temperature and heat flow variations over time and temperature. In the case of a change in temperature, DSC is capable of measuring the quantity of excess heat emitted or absorbed by the sample in question, on the basis of the temperature differential between the sample and the reference material (Zambrano et al.,2024).

2. TYPES OF DSC DEVICE

DSC devices can be classified into two distinct categories: those that utilise heat conduction and those that employ power compensation.

2.1.Heat Conduction Calorimeters

Thermal equilibrium is maintained within the calorimetric vessel via the utilisation of a heat flow sensor positioned on a heat sink. The heat sink is typically composed of a thermostatically controlled bath at a constant temperature. The sample and the reference cells are indirectly subjected to the processes of heating and cooling via the medium of the heat sink, which serves as the point of contact (Figure 1a).

It is permitted for the heat generated or dissipated as a result of the calorimetric reaction to transfer to or become integrated with the heat sink that is situated in the surrounding environment. The thermopile is the instrument most frequently used to measure heat flow, situated in the configuration as shown link the sample cell and the heat sink. The disparity in temperature among the sample, reference cells, and associated heat sink gives rise to the generation of an electrical current across the thermopile. The proportion of power output produced by the heat

flow measuring device is directly correlated with the heat flow from the calorimetric vessel to the heat sink. It can be observed that the calorimeters in consideration exhibit a notable time constant with respect to the measuring system. It is therefore imperative to function at exceedingly slowed scan ratios in order to preserve thermal balance (Canadas and Casals,2013).

2.2.Power Compensation Calorimeters

The sampling and reference cells are encased in a thermally insulated jacket that maintains a temperature approximately 10–20°C lower than that of the vessel in which the calorimetric process is conducted. The reference and sample cells are exposed to heating (or cooling) via the utilisation of independent heat sources (Figure 1b). The temperature of the cells is regulated by the continuous adjustment of the power provided to an electric heating medium which is situated inside the vessel. At the commencement of the trial, the freezing capacity is in equilibrium with electrical heat.

To keep the required procedure temperature, the electrical power is regulated in accordance with the occurrence of the calorimetric result. The variation in electrical power between the initial measurement point and any ensuing interval is directly related to the heat admitted or emitted by the calorimetric procedure. The calorimeters demonstrate a significantly reduced reaction time and perform at substantially quicker scan ratios than heat transfer devices (Canadas and Casals, 2013).

Figure 1. A variety of differential scanning calorimeters are available, (a) heat conduction calorimeters and (b) power compensation calorimeters

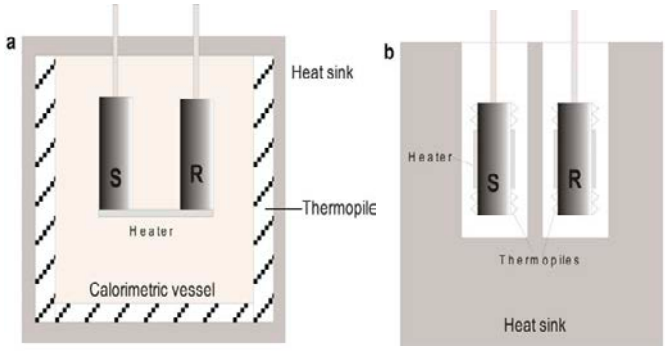

Source: (Canadas and Casals,2013).

3. THEORETICAL FUNDAMENTALS OF DSC

DSC is a thermoanalytical method that allows for the calculation of the differential heat flow (Δq) through a sample in comparison to a reference sample, as a function of temperature (T). This definition is expressed by the following equation (1):

$$\Delta q = q_{sample} - q_{reference} \quad (1)$$

In this context, the term "q_{sample}" denotes the heat flow focused toward the sample, whereas the term "$q_{reference}$" signifies the heat flow targeted toward the reference point. In DSC, the heat capacity, C_p, is a crucial physical property that must be considered. The term is expressed as the quantity of heat, represented by the variable q, that is required to elevate the temperature of the sample, T, by a specified increment, ΔT. Equation 2 provides the mathematical expression for the heat capacity.

$$C_p = \frac{\Delta q}{\Delta T} \quad (2)$$

In DSC examination, the sample and reference are exposed to a precisely regulated process that is contingent upon the thermodynamic transition rates, which are determined by exothermic or endothermic changes. The rate of transition is expressed as the change in temperature (ΔT) relation to the variation in time (Δt). This is derived from equation 3:

$$\beta = \frac{\Delta T}{\Delta t} \quad (3)$$

The discrepancy in heat flux (Δq) among the specimen and the control may be ascribed to a plethora of processes occurring within the specimen, including phase changes, physical modifications, and chemical reaction. In the event that these procedures are endothermic (heat-absorbing), the peak in the DSC thermogram will be oriented in an upward direction. In the event that the process may be exothermic (i.e. heat is released), the peak in the DSC thermogram will be downward (Candas and Casals,2013).

DSC is employed to ascertain the heat capacity at constant pressure (C_p) of the specimen solution in comparison to the reference substance, which is typically the identical buffer utilised in the formulation of the example solution. To ascertain the calorimetric enthalpy of the transition (ΔH_{cal}), it is required to participate the peak of the DSC thermogram.

$$\Delta H_{cal} = \int Cp.\, dT \quad (4)$$

The degree of disorder, or entropy, associated with the transition in question can be determined through the application of the relevant calculation, as detailed in Equation 5.

$$\Delta S = \frac{\Delta H_{cal}}{T_m} \quad (5)$$

T_m: temperature of main phase transition.

In the case of a binary transition (A ⇆ B), wherein the symmetry constant K is contingent upon the enthalpy, this can be expressed by the van't Hoff equality (Equation 6).

The van't Hoff enthalpy, symbolized by ΔH_{vH}, is defined as the enthalpy change of a process when a unit mass of a substance is transferred from the initial state (denoted as A) to a final state (denoted as B). The gas constant, symbolized by R, is stated as the ratio of the absolute temperature (in kelvins) to the universal gas constant.

The alteration in Gibbs free energy that occurs during a phase transition is dependent upon both enthalpy and entropy. The relationship between Gibbs free energy (ΔG^0) and enthalpy and entropy is expressed by equation 7.

$$\Delta G^0 = \Delta H^0 - T\,\Delta S^0 \quad (7)$$

$$\Delta G^0 = -RT\ln K \quad (8)$$

$$\ln K = -\frac{\Delta H^0}{RT} + \frac{\Delta S^0}{R} \quad (9)$$

It can be demonstrated that the plot of the natural logarithm of K against 1/T causes a straight line; The slope of the line represents the negative of the van't Hoff Enthalpy, expressed as a ratio relative to the gas constant ($-\frac{\Delta H^0}{RT}$). At the point of intersection between the curve and the axis, the standard entropy variation is equal to the ratio of the gas constant to the value in question ($\frac{\Delta S^0}{R}$).

It should be noted that the linearity observed in this graph is limited to specific, relatively simple examples and occurs within a restricted temperature range. In the majority of cases, a curved shape is observed in van't Hoff graphs as a consequence of the temperature dependence of ΔH. A non-linear least squares

analysis is required to be conducted on the data, utilising the unified formulation of the van 't Hoff equation (Equation 10).

$$\ln\frac{K}{K_0} = \frac{\Delta H^0 - T_0 \Delta C_p}{R}\left(\frac{1}{T_0} - \frac{1}{T}\right) + \frac{\Delta C_p}{R} ln \frac{T}{T_0} \quad (10)$$

The temperature-dependent change in heat capacity is represented by ΔC_p. In this context, T_0 represents an arbitrarily selected reference temperature. The equilibrium constant at this specified temperature is represented by the symbol K_0. The van 't Hoff enthalpy, ΔH^0, has been selected at this specified temperature.

The enthalpy of van't Hoff (ΔH_{vH}) has been defined as the sum of heat involved per unit of cooperativity for a phase transition to occur. A comparison of the calorimetric enthalpy with the van't Hoff enthalpy requires data concerning the nature of the transition. In the case of a first-order two-state transition, the enthalpy of van't Hoff is equivalent to the enthalpy of calorimetric. However, in approaches containing transient phases, the van't Hoff enthalpy is stated to be less than the enthalpy of calorimetric. Ultimately, in the presence of oligomers during a thermotropic transition, the enthalpy of van't Hoff has been observed to exceed that of the calorimetric enthalpy. The numerical value of the molecules per cooperative unit is established through the application of equation 11 (Canadas and Casals, 2013; Ohline et al.,2001).

$$CU = \frac{\Delta H_{vH}}{\Delta H_{cal}} \quad (11)$$

4. IMPORTANT THERMODYNAMICAL PARAMETERS FOR LIPOSOMES

The main transition temperature (Fig. 2a; T_m) is obtained at the highest of the peak of the heat capacity outline, which corresponds to the temperature at which the transitions of the

double layer membrane between the gel and the liquid crystalline phase occur.

The width of the transition (Figure 2b; $\Delta T_{1/2}$), characterized by the full width at the maximum half of the peak of heat capacity, provides information on the degree of cooperativity exhibited by the transition. It is contingent upon the quantity of molecules engaged in a corresponding transition at the same time. A narrow distribution of transition times indicates a high level of molecular cooperation, while a wide transition indicates a lower level of molecular cooperation.

The enthalpy change (ΔH) linked to the principal transition can be determined by subtracting the area below the heat capacity curve from the total area under the curve. This calculation provides insight into the energy necessitated by the transition (Figure 2b). This phenomenon is linked to the intensity of the van der Waals forces that act upon the fatty acid chains of the lipids (Hatziantoniou et al., 2005).

Figure 2. (a) Representative DSC thermogram illustrating the thermotropic phase behaviour of a phosphatidylcholine (PC) bilayer sample; (b) This magnified image of the peak of principal phase transition in a phospholipid thermogram highlights specific temperature-related changes in the calorimetric data

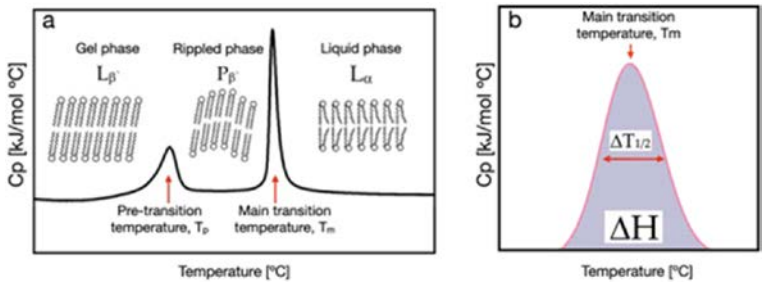

Source: (Zambrano et al.,2024).

5. THE THERMOTROPIC BEHAVIOUR OF PHOSPHOLIPIDS

Synthetic long-chain phospholipids, in their pure form, undergo a series of transitions at temperatures that are precisely defined in relation to their structure. The aforementioned transitions can be classified as follows:

1) **The process of transitioning from the gel phase through to the liquid phase:**

This change is rapid and is indicated by the temperature of the transition (T_m) (Privalov et al.,1975; Tsong,1974).

2) **The pre-transition temperature (T_p):**

This occurs at a temperature 5-10°C below that of the main phase transition (T_m). This occurs at a slower rate than the primary phase transition temperature. This alteration (from gel to wavy phase) is observed exclusively in the presence of sufficiently hydrated lipids. This type of transition is particularly susceptible to the influence of minor contaminant quantities (Cevc,1991).

3) **The subgel transition**:

This transition is observed to occur at a very slow rate, with a temperature of approximately T_m - 30°C. Its molecular characterisation remains incomplete.

Each of these transitions is characterised by a number of factors, including the temperature range over which it occurs (T_m, T_p, T_s), the enthalpy variations of the transformation (ΔH_m, ΔH_P, ΔH_S), the cleanliness of the structure and the width and form of the curve of the transition (Biltonen and Lichtenberg,1993).

6. THE EFFECTS OF TAIL AND HEAD GROUPS OF PHOSPHOLIPIDS ON THERMODYNAMIC PARAMETERS (PHASE TRANSITION TEMPERATURE AND ENTHALPY)

6.1. The Effect of Chain Length on Phase Transition Temperature and Enthalpy Changes of Phospholipids

The temperature at which a phospholipid undergoes a phase transition, with the accompanying enthalpy alteration, is strongly influenced by the length of its acyl chain. For symmetric filled 1,2-diacyl PCs, an enhancement of the size of the chain leads to a rise of T_m by 7-14 °C/carbon atom (Table 1), while the number of CH_2 groups leads to an increase in ΔH° (1-2 kcal/mol/CH_2) (Myers et al.,1987; Biltonen and Lichtenberg,1993).

Table 1. Dependence of phase transition temperature and enthalpy changes on chain length for 1,2-diacyl-sn-glycerol (3) phosphocholines in multilamellar vesicles (MLVs)

Acyl chain lenght of the phospholipis	T_m (^{0}C)	ΔH(kcal/mol)
12	-1.1	2.9
14	23.5	5.9
16	41.4	8.3
18	55.1	10.1
20	61.8	11.9
22	74.0	14.2

Source: (Biltonen and Lichtenberg,1993).

6.2. The Effect of The Head Group of the Phospholipids on Phase Transition Temperature and Enthalpy Changes

The significant correlation between T_m and length of the chain and saturation demonstrates that thermodynamic properties associated with melting are predominantly influenced by specific interactions taking place within the gel and liquid crystalline

phase, whereby non-polar acyl chains exert a dominant influence. Nevertheless, the head groups of phospholipids exert a considerable influence on the thermotropic behaviour of phospholipids (Marsh, 1990).

The precise impact of the head group on the transition is contingent upon the ion strength and the specific composition of ions present in the solution. Nevertheless, under clearly defined circumstances, the phase behavior can be reproduced. In solutions including salt concentrations under 1 M, the replacement of the choline head group by ethanolamine has been observed to result in an increase in T_m of 20-30°C and a corresponding increase in the enthalpy change ΔH° (Table 2).

The thermotropic phase behaviour of vesicular structures formed from acidic lipid molecules is dependent upon the ionisation state of the phospholipid, which in turn is contingent upon the solution pH. Consequently, for di-C_{l6} PG, the melting temperature (T_m) shifts from 57 to 41°C while the pH value rises from 1.1 to 7. Similarly, representing PA and PS, the distinct two ionisation phases may be observed as the pH value rises (once more, deprotonation results in a reduction in T_m (Blume and Tuchtenhagen,1992).

Table 2. The effect of the head group of the phospholipids on the phase transition and enthalpy of 1,2-di-C_{l6} (16:0)

Abbrevation	Head-Group of Phospholipids	pH	T_m(^{0}C)	Δ*H*(kcal/mol)
PC	Choline	7.4	41.4	8.3
PE	Ethanolamine	7.4	64	8.5
PG	Glycerol	1.1 7.0	57 41	8.9 7.5
PA	Phosphatidic acid	6.5 9.1	67 58	5.2 2.9
PS	Phosphatidylserine	12 2 7	43.1 67 54	5.7 8.1 9.0
SM	Sphingomyelin	13 7.4	32 41.3	8.0 6.8
Lyso PC	Lyso Choline	7.4	3	4

Source: (Biltonen and Lichtenberg,1993)

6.3.The Changes in Thermodynamic Parameters in Liposomes Containing Mixed Phospholipids

A significant proportion of samples with practical implications comprise phospholipids with diverse fatty acid chains. The introduction of a second lipid element into a system comprising a single lipid component can result in substantial modifications to the system's thermotropic behaviour. If the two lipid mixtures in the system under investigation exhibit similar thermotropic properties, the behaviour of the diverse system will be analogous to that of the uncontaminated system, exhibiting an asymmetric and broadened transition peak (Mabrey and Sturtevant, 1977).

The specific morphology of the transition peak will be indicative of the constituents present within the prepared mixture. The thermotropic behaviour of these binary substances is typically adequately characterised by straightforward phase diagrams, which illustrate the correlation between the melting temperature and the composition.

The leverage principle is a useful tool for determining the relative proportions of the phases present in the region where two phases coexist. In most cases, binary and ternary combinations of phospholipids exhibit a high degree of complexity in their thermotropic behaviour. The observed behaviour is largely determined by the specific composition of the preparation and the methodology employed in its creation. It is so challenging to provide a comprehensive description of the thermotropic behaviour of a complex lipid system. Nevertheless, the excess heat capacity function is replete with information concerning the characteristics of the transition and may be utilised to great advantage as an investigative instrument to evaluate the reproducibility of sample preparation.

This is particularly the case in systems where the components are prone to either lateral or macroscopic phase separation. Phase separation can frequently be observed in the phase of gel. Nevertheless, there exists a considerable temperature interval within which regions of the liquid crystalline state, gel state and lipid state coexist, exhibiting compositional disparities. In the liquid crystalline state, lipids are typically regarded as reasonably miscible. However, evidence suggests that dynamic heterogeneity may also occur in such structures (van Osdol et al., 1992).

7. THE IMPORTANCE OF DSC IN DRUG-MEMBRANE INTERACTIONS

One of the pivotal techniques employed in the investigation of interactions between drugs and biological membranes is DSC. The thermoanalytical technique in question involves measuring the differential heat flow in a given sample in comparison to a reference point, with the data presented as a function of either time or temperature. During the drug-membrane studies, DSC is utilized to investigate the phase of thermotropic activities of lipid membranes, with the objective of elucidating the impact of drug presence on this phenomenon (Chaires,2008).

Despite the considerable insights offered by DSC into drug-membrane interactions, the intricate complexity of biological membranes represents a substantial challenge. Biological structures are complex, macromolecular assemblies comprising a diverse array of lipids, proteins, and carbohydrates. The intricate and multifaceted nature of this subject matter presents a substantial challenge to the comprehensive investigation of drug-membrane interactions, regardless of whether the study is conducted in vivo or in vitro. Researchers

have found it beneficial to utilise simplified models of biological membranes to progress beyond the limitations of the existing challenge (Bruylants et al.,2005).

The aforementioned models, which may encompass everything from simple lipid bilayers to more intricate structures incorporating proteins and additional elements, provide researchers with the chance to examine drug interactions with biological membranes in a more regulated and manageable way. Phospholipid membranes are one of the most employed membrane examples in DSC investigates (Balestrieri et al.,1996).

Phospholipids constitute the primary element of biological membranes. Due to their amphipathic character, comprising a hydrophilic and hydrophobic part of membranes (a head group and a fatty acid tail), these molecules are capable of forming bilayers that closely resemble the structural configuration of cell membranes. Phospholipids can form an assembly of structures, each with distinct advantages and limitations. These include single-layer vesicles (also known as monolayer vesicles), multilayer vesicles (multilayer vesicles), and supported lipid bilayers (SLB). Single-layer vesicles offer a straightforward and uniform platform for investigating drug-membrane connections. Nevertheless, their diminutive dimension and monolayer configuration cannot wholly reflect the intricacies of biological membranes. In contrast, multilayer vesicles (MLVs) possess a further intricate formation, and in certain instances, the presence of numerous layers be able to render the explanation of DSC data challenging. Single-layer vesicles offer a straightforward and uniform structure for investigating drug-membrane interactions. Nevertheless, their diminutive dimension and unidimensional constitution may not wholly reflect the intricacies of biological membranes (Carvalho et al., 2020; Chiu and Prenner, 2011; Gaisford and Buanz,2011; Van Buren et al., 2022). Conversely, multilayer vesicles (MLVs) exhibit enhanced

stability relative to single-layer vesicles, facilitate more straightforward preparation and storage, and enable more accurate interpretation of DSC data (Zambrano et al,2024).

8. CONCLUSION

In conclusion, DSC is a thermal analysis method that is frequently employed in the pharmaceutical industry for the determination of a sample's purity, polymorphic forms and melting point. Although its principal application is in the drug improvement procedure, DSC is a valuable technique for the design of lipidic drug delivery systems, such as liposomes. It allows the cooperation of diverse elements to be determined and the optimal liposomal composition to be identified.

A significant application of DSC is the investigation of thermodynamic alterations in lipid bilayers following the incorporation of a pharmaceutical agent. Such modifications may be attributed to interactions between the pharmaceutical agent and its lipid carrier. This process may influence the drug's bioavailability. The thermodynamic properties of a substance are of great significance, exerting a profound influence on both the pharmacokinetics of the drug in question and the long-term stability of the liposomal formulation under a given set of storage environments.

REFERENCES

Balestrieri, F., Magrì, A. D., Magrì, A. L., Marini, D., & Sacchini, A. (1996). Application of differential scanning calorimetry to the study of drug-excipient compatibility. *Thermochimica acta*, *285*(2), 337-345.

Biltonen, R. L., & Lichtenberg, D. (1993). The use of differential scanning calorimetry as a tool to characterize liposome preparations. *Chemistry and physics of lipids*, *64*(1-3), 129-142.

Bruylants, G., Wouters, J., & Michaux, C. (2005). Differential scanning calorimetry in life science: thermodynamics, stability, molecular recognition and application in drug design. *Current medicinal chemistry*, *12*(17), 2011-2020.

Canadas, O. and Casals, C., 2013, Differential Scanning Calorimetry of Protein–Lipid Interactions, Lipid-Protein Interactions, 55–71p.

Carvalho, S. G., Cipriano, D. F., de Freitas, J. C. C., Junior, M. A. S., Ocaris, E. R. Y., Teles, C. B. G., ... & Villanova, J. C. O. (2020). Physicochemical characterization and in vitro biological evaluation of solid compounds from furazolidone-based cyclodextrins for use as leishmanicidal agents. *Drug Delivery and Translational Research*, *10*, 1788-1809.

Cevc, G. (1991). Polymorphism of the bilayer membranes in the ordered phase and the molecular origin of the lipid pretransition and rippled lamellae. *Biochimica et Biophysica Acta (BBA)-Biomembranes*, *1062*(1), 59-69.

Chaires, J. B. (2008). Calorimetry and thermodynamics in drug design. *Annu. Rev. Biophys.*, *37*(1), 135-151.

Chiu, M. H., & Prenner, E. J. (2011). Differential scanning calorimetry: An invaluable tool for a detailed

thermodynamic characterization of macromolecules and their interactions. *Journal of Pharmacy and Bioallied Sciences*, *3*(1), 39-59.

Doktorova, M., Heberle, F. A., Eicher, B., Standaert, R. F., Katsaras, J., London, E., ... & Marquardt, D. (2018). Preparation of asymmetric phospholipid vesicles for use as cell membrane models. *Nature protocols*, *13*(9), 2086-2101.

Even, J., Bertault, M., Girard, A., Délugeard, Y., & Marqueton, Y. (1997). Optical and calorimetric studies on the role of lattice mode softening in assisting a thermally enhanced solid-state reaction. *Chemical physics letters*, *267*(5-6), 585-589.

Gaisford, S., & Buanz, A. B. (2011). Pharmaceutical physical form characterisation with fast (> 200° C min− 1) DSC heating rates. *Journal of thermal analysis and calorimetry*, *106*(1), 221-226.

Hatziantoniou, S. and Demetzos, C., 2008, Lipids of membranes: chemistry, biological role and applications as drug carriers, Attaur-Rahman (Ed.) Studies in Natural Products Chemistry,34:173-201p.

Hope, M. J., Bally, M. B., Mayer, L. D., Janoff, A. S., & Cullis, P. R. (1986). Generation of multilamellar and unilamellar phospholipid vesicles. *Chemistry and physics of lipids*, *40*(2-4), 89-107.

Höhne, G. W. H., Hemminger, W., & Flammersheim, H. J. (2003). *Differential scanning calorimetry* (Vol. 2, pp. 9-30). Berlin: Springer.

Lin, L. N., Mason, A. B., Woodworth, R. C., & Brandts, J. F. (1993). Calorimetric studies of the N-terminal half-molecule of transferrin and mutant forms modified near

the Fe3+-binding site. *Biochemical Journal*, *293*(2), 517-522.

Ladbury, J. E., & Chowdhry, B. Z. (1996). Sensing the heat: the application of isothermal titration calorimetry to thermodynamic studies of biomolecular interactions. *Chemistry & biology*, *3*(10), 791-801.

Mabrey, S., & Sturtevant, J. M. (1977). Incorporation of saturated fatty acids into phosphatidylcholine bilayers. *Biochimica et Biophysica Acta (BBA)-Lipids and Lipid Metabolism*, *486*(3), 444-450.

Mardešić, I., Boban, Z., Subczynski, W. K., & Raguz, M. (2023). Membrane models and experiments suitable for studies of the cholesterol bilayer domains. *Membranes*, *13*(3), 320.

Myers, M., Mayorga, O. L., Emtage, J., & Freire, E. (1987). Thermodynamic characterization of interactions between ornithine transcarbamylase leader peptide and phospholipid bilayer membranes. *Biochemistry*, *26*(14), 4309-4315.

Ohline, S.M., Campbell, M.L., Turnbull, M.T., and Kohler, S.J., 2000, Differential Scanning Calorimetry of Bilayer Membrane Phase Transitions1,2,369-71, 391-395p.

Privalov, P. L., Plotnikov, V. V., & Filimonov, V. V. (1975). Precision scanning microcalorimeter for the study of liquids. *The Journal of Chemical Thermodynamics*, *7*(1), 41-47.

Privalov, P. L., & Potekhin, S. A. (1986). [2] Scanning microcalorimetry in studying temperature-induced changes in proteins. In *Methods in enzymology* (Vol. 131, pp. 4-51). Academic Press.

Protasevich, I., Ranjbar, B., Lobachov, V., Makarov, A., Gilli, R., Briand, C., ... & Haiech, J. (1997). Conformation and

thermal denaturation of apocalmodulin: role of electrostatic mutations. *Biochemistry*, *36*(8), 2017-2024.

Saito, Y., Saito, K., & Atake, T. (1986). Theoretical analysis of heat-flux differential scanning calorimetry based on a general model. *Thermochimica acta*, *99*, 299-307.

Weber, P. C., & Salemme, F. R. (2003). Applications of calorimetric methods to drug discovery and the study of protein interactions. *Current opinion in structural biology*, *13*(1), 115-121.

Van Buren, L., Koenderink, G. H., & Martinez-Torres, C. (2022). DisGUVery: a versatile open-source software for high-throughput image analysis of Giant Unilamellar Vesicles. *ACS Synthetic Biology*, *12*(1), 120-135.

van Osdol, W. W., Ye, Q., Johnson, M. L., & Biltonen, R. L. (1992). Effects of the anesthetic dibucaine on the kinetics of the gel-liquid crystalline transition of dipalmitoylphosphatidylcholine multilamellar vesicles. *Biophysical journal*, *63*(4), 1011-1017.

Varghese, N., Vivekchand, S. R. C., Govindaraj, A., & Rao, C. N. R. (2008). A calorimetric investigation of the assembly of gold nanorods to form necklaces. *Chemical Physics Letters*, *450*(4-6), 340-344.

Von Stockar, U., & Marison, I. W. (2005). The use of calorimetry in biotechnology. In *Bioprocesses and engineering* (pp. 93-136). Berlin, Heidelberg: Springer Berlin Heidelberg.

Yeagle, P. L. (2004). *The structure of biological membranes*. CRC press.

Zambrano, P., Manrique-Moreno, M., Petit, K., Colina, J. R., Jemiola-Rzeminska, M., Suwalsky, M., & Strzalka, K. (2024). Differential scanning calorimetry in drug-

membrane interactions. *Biochemical and Biophysical Research Communications*, 149806.

LASER-INDUCED GRAPHENE: A NEW FRONTIER IN MATERIALS SCIENCE

Alper ÇETİNEL[1]

1. INTRODUCTION

In recent years, the advent of laser-induced graphene (LIG) has ignited a fervor of research and development across various scientific and engineering disciplines. This innovative material, a form of graphene fabricated through the direct laser scribing of carbon-rich precursors, has rapidly gained recognition for its remarkable properties, versatility, and potential to revolutionize numerous applications (Kwak et al., 2024). Laser-induced graphene is a porous, three-dimensional network of graphene sheets produced by the rapid heating and carbonization of a suitable precursor material using a focused laser beam. The laser energy causes the precursor to undergo a series of transformations, including pyrolysis, graphitization, and exfoliation, resulting in the formation of a interconnected graphene structure (John Jeya Kamaraj et al., 2024). The morphology, properties, and performance of LIG can be tailored by controlling various parameters such as laser power, scanning speed, precursor type, and environmental conditions (Movaghgharnezhad et al., 2023).

The importance of LIG stems from its unique combination of characteristics that set it apart from other graphene fabrication methods. The direct laser writing process allows for the rapid and maskless fabrication of LIG patterns on a variety of substrates,

[1] Dr. Öğr. Üyesi, Ege Üniversitesi Fen Fakültesi Fizik Bölümü, alper.cetinel@ege.edu.tr, ORCID: 0000-0003-0626-8721.

including polymers, ceramics, and even paper (Guo et al., 2023). This versatility enables the integration of LIG into complex devices and systems without the need for expensive and time-consuming lithographic techniques. LIG production can be readily scaled up for large-area applications, making it a promising candidate for industrial manufacturing. The ability to produce LIG on flexible substrates further expands its potential for applications in wearable electronics and flexible displays. The porous structure of LIG provides ample opportunities for surface modification and functionalization, enabling the tailoring of its properties for specific applications. This opens up new avenues for the development of LIG-based sensors, energy storage devices, and biomedical applications (Avinash & Patolsky, 2023).

The unique properties of LIG have led to its exploration in a wide range of applications, with new possibilities emerging constantly. The high surface area and electrical conductivity of LIG make it an attractive material for electrodes in supercapacitors and batteries. LIG-based electrodes exhibit excellent electrochemical performance, including high specific capacitance, long cycle life, and fast charge-discharge rates. LIG's sensitivity to changes in its environment makes it an ideal platform for the development of various sensors (Yao et al., 2023). LIG-based sensors have been demonstrated for the detection of gases, biomolecules, strain, and temperature. The ability to fabricate LIG patterns directly on flexible substrates allows for the development of wearable and conformal sensors. The biocompatibility and electrical conductivity of LIG have sparked interest in its use for biomedical applications, such as neural interfaces, biosensors, and tissue engineering scaffolds. LIG's ability to promote cell adhesion and proliferation makes it a promising material for regenerative medicine. LIG's porous structure and high adsorption capacity make it a potential

candidate for water purification and air filtration. LIG-based filters have been shown to effectively remove heavy metals, organic pollutants, and even bacteria from contaminated water (Ouedraogo et al., 2023). The ability to fabricate LIG on flexible substrates opens up exciting opportunities for the development of wearable electronics, flexible displays, and soft robotics. LIG's electrical conductivity and mechanical flexibility make it an ideal material for interconnects, electrodes, and sensors in these applications (Yang et al., 2023).

2. PRODUCTION METHODS

2.1.Laser Wavelengths and Types

The choice of laser wavelength and type plays a crucial role in determining the efficiency, quality, and properties of the resulting LIG.

2.2.Common Laser Wavelengths

2.2.1. 1064 nm (Near-Infrared)

This wavelength, often generated by Nd:YAG lasers, is widely used for LIG production due to its efficient absorption by many carbon-rich precursors, such as polyimide. The 1064 nm laser provides a good balance between energy deposition and penetration depth, enabling the formation of high-quality LIG with controlled morphology. Many carbon-rich precursors, like polyimide, readily absorb 1064 nm radiation. This leads to efficient energy deposition and localized heating at the laser focus. The moderate penetration depth allows for precise control over the LIG thickness and morphology. LIG produced with 1064 nm lasers typically exhibits a well-defined, porous structure with interconnected graphene sheets. The porosity can be tuned by adjusting laser parameters like power and scanning speed. The LIG formed using 1064 nm lasers often shows high electrical

conductivity due to the efficient graphitization process. This makes it suitable for applications like electrodes and sensors. The mechanical properties of LIG produced with 1064 nm lasers are generally good, with moderate flexibility and strength. This makes it useful for applications where some degree of mechanical robustness is required (Mostaccio et al., 2023).

2.2.2. 10.6 µm (Mid-Infrared)

CO_2 lasers emitting at this wavelength are also commonly used for LIG fabrication, particularly for precursors with high absorption in the mid-infrared region. The longer wavelength of the CO_2 laser allows for deeper penetration into the precursor material, facilitating the formation of thicker LIG structures. CO_2 lasers emitting at 10.6 µm are well-absorbed by certain precursors, especially those with high oxygen content. The longer wavelength allows for deeper penetration into the material, leading to thicker LIG structures. LIG produced with 10.6 µm lasers often has a more layered and less porous structure compared to that produced with 1064 nm lasers. The increased thickness can be beneficial for applications requiring high mechanical strength or improved electrochemical performance. The electrical conductivity of LIG formed using 10.6 µm lasers can be lower than that produced with 1064 nm lasers, potentially due to incomplete graphitization or the presence of amorphous carbon. However, it can still be sufficient for many applications. The thicker LIG structures produced with 10.6 µm lasers often exhibit enhanced mechanical strength and stiffness. This makes them suitable for applications demanding robust mechanical performance (de la Roche et al., 2023).

2.2.3. 355 nm and 532 nm (Ultraviolet and Visible)

These shorter wavelengths, typically generated by solid-state lasers, are less commonly used for LIG production due to their lower absorption by many carbon-rich precursors. However,

they can be effective for specific precursors or applications where precise control of the LIG morphology is desired. These shorter wavelengths are less efficiently absorbed by many common precursors. This can lead to less efficient energy deposition and lower graphitization efficiency. However, they offer precise control over the laser spot size, enabling the fabrication of fine LIG features. LIG produced with UV and visible lasers often has a less porous and more compact structure compared to that produced with longer wavelengths. This can be advantageous for applications requiring high resolution or smooth surfaces. The electrical conductivity of LIG formed using UV and visible lasers can vary depending on the precursor and laser parameters. However, it can be improved through post-processing techniques like thermal annealing. The mechanical properties of LIG produced with UV and visible lasers can be influenced by the resulting morphology and degree of graphitization. Generally, they exhibit moderate flexibility and strength (Y. Wang et al., 2023).

2.2.4. 450 nm

Utilizing a 450 nm wavelength laser for LIG production shares certain similarities with the effects observed with UV (355 nm) and visible (532 nm) lasers, but also presents some unique characteristics due to its position on the boundary between the visible and UV spectrum. The absorption of 450 nm radiation by common LIG precursors like polyimide is generally lower than that of 1064 nm or 10.6 µm but can be higher than for deeper UV wavelengths like 355 nm. This results in a moderate penetration depth, offering a balance between precise control of LIG features and the ability to produce thicker structures compared to deeper UV lasers. Similar to UV and visible lasers, LIG produced with 450 nm lasers tends to have a less porous and more compact structure (Coelho et al., 2023). This can be beneficial for applications where a smoother surface or higher density is

desired. The moderate penetration depth can lead to the formation of LIG structures with thicknesses intermediate between those produced with near-infrared and deep UV lasers. The electrical conductivity of 450 nm LIG can be influenced by factors like precursor material, laser parameters, and post-processing techniques. It may require optimization to achieve high conductivity comparable to that of LIG produced with 1064 nm lasers. However, studies have shown that 450 nm LIG can exhibit good electrical conductivity suitable for various applications, particularly after post-processing treatments. The mechanical properties of 450 nm LIG are influenced by its morphology and degree of graphitization. Generally, it exhibits moderate flexibility and strength, similar to LIG produced with UV and visible lasers. The ability to produce thicker LIG structures with 450 nm lasers can potentially enhance its mechanical robustness compared to deeper UV lasers (Wanjari et al., 2023).

The 450 nm wavelength lies in a region where some precursors may exhibit photochemical reactions in addition to thermal effects. This can influence the LIG formation process and its properties. The interaction of 450 nm laser radiation with the substrate material needs to be carefully considered, as it can lead to substrate modification or damage in some cases. Research on LIG produced with 450 nm lasers is still ongoing, and further studies are needed to fully understand its unique characteristics and potential applications. Using a 450 nm laser for LIG production offers a compromise between the precise control of UV lasers and the deeper penetration of near-infrared lasers. It enables the fabrication of moderately thick LIG structures with less porosity and potentially good electrical conductivity. Further research and optimization of laser parameters and post-processing techniques can unlock the full potential of 450 nm LIG for various applications (Q. Zhang et al., 2023).

2.3.Laser Types

Pulsed lasers, such as Q-switched Nd:YAG lasers and pulsed CO2 lasers, are commonly used for LIG fabrication due to their ability to deliver high peak power in short pulses. This enables rapid heating and carbonization of the precursor material, minimizing thermal damage to the surrounding areas (Hong et al., 2023). **Continuous-wave (cw) lasers**, such as fiber lasers and diode lasers, can also be used for LIG production, although they typically require higher power densities to achieve the same level of carbonization as pulsed lasers. CW lasers can be advantageous for applications where large-area or continuous LIG patterns are desired (Zou et al., 2023).

The optimal laser wavelength and type for LIG fabrication depend on several factors, including **precursor material, desired lig properties, and substrate compatibility.** The absorption characteristics of the precursor material play a crucial role in determining the suitable laser wavelength. Precursors with strong absorption in the near-infrared region are well-suited for 1064 nm lasers, while those with high absorption in the mid-infrared region may benefit from CO_2 lasers. The desired properties of the LIG, such as thickness, porosity, and electrical conductivity, can also influence the choice of laser wavelength and type. Shorter wavelengths may be preferred for applications requiring fine features or precise control of the LIG morphology. The laser wavelength and type should also be compatible with the substrate material to avoid damage or undesirable interactions (Hong et al., 2023; L. Wang et al., 2020).

In conclusion, the selection of laser wavelength and type is a critical consideration in the fabrication of laser-induced graphene. The most common wavelengths used are 1064 nm and 10.6 μm, generated by Nd:YAG and CO_2 lasers, respectively. Pulsed lasers are typically preferred for their ability to deliver

high peak power in short pulses, enabling efficient and controlled carbonization of the precursor material (Hong et al., 2023; L. Wang et al., 2020).

The optimal laser parameters for LIG production depend on various factors, including the precursor material, desired LIG properties, and substrate compatibility. Understanding these factors and their interplay is crucial for achieving high-quality LIG with tailored properties for specific applications. Besides wavelength, other laser parameters like power density, scanning speed, and pulse duration also significantly affect the LIG properties. Optimizing these parameters is crucial for achieving the desired LIG characteristics. The choice of precursor material also influences the LIG properties, regardless of the laser wavelength used. Different precursors exhibit varying degrees of graphitization and lead to different LIG morphologies. Post-processing techniques like thermal annealing or chemical doping can further modify the properties of LIG produced with different laser wavelengths (H. Liu et al., 2023).

3. APPLICATION AREAS

Laser-induced graphene (LIG) has garnered significant attention for its potential in a broad spectrum of scientific applications, owing to its unique properties and versatile fabrication process.

3.1.Sensors and Biosensors

LIG's high surface area and electrical conductivity make it sensitive to changes in its environment, enabling the detection of various gases, including toxic gases and volatile organic compounds. LIG can be functionalized with biomolecules, such as antibodies or enzymes, to create highly sensitive and selective biosensors for the detection of biomarkers or pathogens. LIG's

electrical resistance changes under strain, allowing it to function as a flexible and wearable strain or pressure sensor. LIG exhibits a temperature-dependent resistance, enabling its use as a temperature sensor with potential applications in healthcare and industrial monitoring (Wanjari et al., 2023).

3.2.Gas Sensors

LIG's high surface area and electrical conductivity allow it to readily adsorb gas molecules, leading to changes in its electrical resistance. By measuring these resistance changes, the presence and concentration of specific gases can be detected. LIG-based gas sensors have been demonstrated for the detection of various toxic gases, such as carbon monoxide, nitrogen dioxide, and ammonia, with high sensitivity and selectivity. This enables their use in environmental monitoring, industrial safety, and even wearable devices for personal protection. LIG sensors can also detect VOCs, which are emitted from various sources like paints, adhesives, and cleaning products. This has applications in indoor air quality monitoring, food safety, and medical diagnostics, as certain VOCs can be indicative of diseases(Kwak et al., 2024).

3.3.Biosensors

LIG can be functionalized with biorecognition elements, like antibodies, enzymes, or DNA probes, which specifically bind to target biomolecules. The binding event triggers a change in LIG's electrical properties, enabling the detection of the target analyte. LIG-based biosensors have been developed for the detection of various biomarkers associated with diseases like cancer, diabetes, and infectious diseases. This allows for rapid and point-of-care diagnostics, potentially enabling early disease detection and treatment. LIG biosensors can be used to detect environmental pollutants, such as pesticides, heavy metals, and toxins, providing valuable information for environmental

protection and risk assessment. LIG biosensors can be employed for the detection of foodborne pathogens and contaminants, ensuring food safety and preventing outbreaks of foodborne illnesses (Aparicio-Martínez et al., 2023; Wanjari et al., 2023).

3.4.Strain and Pressure Sensors

When LIG is subjected to strain or pressure, its electrical resistance changes due to the deformation of the graphene network. This change in resistance can be measured and correlated to the applied strain or pressure. LIG-based strain sensors can be integrated into wearable devices to monitor physiological signals like heart rate, respiration, and muscle activity, providing valuable health data for individuals and healthcare professionals. LIG strain sensors can be embedded in structures like bridges or buildings to monitor their structural integrity and detect any signs of damage or deformation. LIG pressure sensors can be used in robotics and prosthetics to provide tactile feedback, enabling robots and prosthetic limbs to interact with their environment more effectively (Zou et al., 2023).

3.5.Temperature Sensors

LIG's electrical resistance exhibits a temperature dependence, meaning its resistance changes with variations in temperature. This property allows LIG to function as a temperature sensor. LIG temperature sensors can be used for continuous temperature monitoring in healthcare settings, providing accurate and real-time data for patient care and fever detection. LIG temperature sensors can be deployed in environmental monitoring systems to track temperature changes in various ecosystems, contributing to climate research and environmental protection efforts (Yang et al., 2023).

These are just a few examples of the diverse applications of LIG in sensors and biosensors. The ability to fabricate LIG directly on various substrates, including flexible and even

wearable materials, further expands its potential in these fields, enabling the development of innovative and impactful sensing technologies (Yang et al., 2023).

3.6.Energy Storage and Conversion

LIG's high surface area and excellent electrical conductivity make it an attractive material for electrodes in supercapacitors, offering high energy and power densities. LIG has been explored as an anode material for lithium-ion batteries, showing improved capacity and cycling stability compared to conventional graphite anodes. LIG can be used as a transparent conductive electrode in solar cells, potentially offering advantages over traditional indium tin oxide (ITO) electrodes in terms of flexibility and cost (Guo et al., 2023).

3.6.1. Supercapacitors

Supercapacitors store energy through the electrostatic adsorption of ions at the electrode-electrolyte interface. LIG's high surface area provides ample space for ion adsorption, while its excellent electrical conductivity facilitates rapid charge transfer. The combination of high surface area and conductivity enables LIG-based supercapacitors to achieve both high energy density (amount of energy stored per unit mass) and high power density (rate at which energy can be delivered). LIG's robust structure and chemical stability contribute to long cycle life, meaning the supercapacitor can be charged and discharged many times without significant performance degradation. The high conductivity of LIG allows for rapid charge and discharge, making it suitable for applications requiring quick energy delivery or storage. LIG-based supercapacitors can be used in portable electronics like smartphones and laptops to provide fast charging and longer battery life. Supercapacitors can complement batteries in electric vehicles, providing quick bursts of power for acceleration and regenerative braking. Large-scale LIG-based

supercapacitors could be used for grid energy storage, helping to balance supply and demand and integrate renewable energy sources into the grid (Li et al., 2023; Yao et al., 2023).

3.6.2. Batteries

Batteries store energy through chemical reactions at the electrodes. LIG can be used as an anode material in lithium-ion batteries, where lithium ions are intercalated into the graphene layers during charging and released during discharge. The high surface area of LIG can accommodate more lithium ions, leading to increased battery capacity compared to traditional graphite anodes. LIG's robust structure can withstand the volume changes associated with lithium intercalation and deintercalation, leading to improved cycling stability and longer battery life. The high conductivity of LIG facilitates faster lithium-ion diffusion, enabling faster charging and discharging of the battery. LIG-based batteries could offer increased range and faster charging times for electric vehicles, making them more attractive to consumers. Higher capacity and faster charging LIG batteries could benefit portable electronics like smartphones and laptops, providing longer usage times and shorter charging durations. Large-scale LIG batteries could be used for grid energy storage, similar to supercapacitors, but with potentially higher energy density (Avinash & Patolsky, 2023).

3.6.3. Solar Cells

Solar cells convert sunlight into electricity through the photovoltaic effect. LIG can be used as a transparent conductive electrode in solar cells, replacing traditional indium tin oxide (ITO) electrodes. LIG's flexibility allows for the fabrication of flexible and even wearable solar cells, opening up new possibilities for solar energy harvesting. LIG can be produced using low-cost laser scribing techniques, potentially making solar cells more affordable. LIG can be tuned to have high

transparency, allowing more light to reach the active layer of the solar cell and potentially increasing its efficiency. Flexible LIG-based solar cells can be integrated into building facades, windows, or rooftops, generating electricity while maintaining aesthetic appeal. LIG solar cells can be incorporated into clothing or accessories, providing power for wearable electronics or even charging personal devices on the go. Flexible LIG solar panels can be used in portable solar chargers, providing a convenient and sustainable way to charge electronic devices outdoors (Y. Wang et al., 2023).

These examples showcase the potential of LIG in revolutionizing energy storage and conversion technologies. Ongoing research and development in this field are expected to lead to further advancements and new applications for LIG in the quest for sustainable and efficient energy solutions (L. Wang et al., 2020).

3.7. Other Applications

3.7.1. Biomedical Applications

LIG's biocompatibility and electrical conductivity make it a promising material for neural interfaces, enabling improved communication between the brain and external devices (Bhaiyya et al., 2021). LIG scaffolds can promote cell adhesion and proliferation, making them useful for tissue engineering and regenerative medicine applications. LIG can be loaded with drugs and used for targeted drug delivery, potentially offering improved therapeutic efficacy and reduced side effects (S. Zhang et al., 2023; Zhu et al., 2021).

3.7.2. Environmental Applications

LIG's porous structure and high adsorption capacity allow it to effectively remove pollutants like heavy metals and organic compounds from contaminated water. LIG-based filters can

capture particulate matter and harmful gases, contributing to air purification and pollution control efforts (Kwak et al., 2024; X. Liu et al., 2023).

3.7.3. Flexible Electronics and Wearables

LIG's flexibility and sensitivity make it suitable for wearable sensors for health monitoring, fitness tracking, and other applications. LIG can be used as a transparent conductive electrode in flexible displays, enabling the development of foldable or rollable screens. LIG can be integrated into textiles to create smart fabrics with embedded sensors or actuators for various applications (Guo et al., 2023; Li et al., 2023; Zou et al., 2023).

LIG can be used to create microfluidic channels and devices for various biological and chemical assays. LIG's thermoacoustic properties allow it to convert heat into sound waves, opening up possibilities for applications like loudspeakers and acoustic sensors. LIG surfaces can be modified to exhibit antimicrobial properties, potentially useful for preventing infections in healthcare settings (Nag et al., 2017).

4. CONCLUSION

Laser-induced graphene's unique combination of properties and ease of fabrication has opened up a vast array of scientific applications. As research in this field continues to advance, we can anticipate even more innovative and impactful uses of LIG in the future, contributing to advancements in various scientific disciplines and ultimately improving our lives.

The choice of laser wavelength plays a pivotal role in determining the properties of laser-induced graphene. Each wavelength offers unique advantages and disadvantages, influencing the LIG morphology, electrical conductivity, and

mechanical properties. By carefully selecting the laser wavelength and optimizing the laser parameters, researchers and engineers can tailor the LIG properties to suit specific applications, expanding the potential of this versatile material in various fields.

Remember that the information presented here is a general overview. The specific effects of different laser wavelengths on LIG properties can vary depending on the precursor material, laser parameters, and post-processing techniques employed.

REFERENCES

Aparicio-Martínez, E. P., Vega-Rios, A., Osuna, V., & Dominguez, R. B. (2023). Salivary Glucose Detection with Laser Induced Graphene/AgNPs Non-Enzymatic Sensor. *Biosensors*, *13*(2). https://doi.org/10.3390/bios13020207

Avinash, K., & Patolsky, F. (2023). Laser-induced graphene structures: From synthesis and applications to future prospects. In *Materials Today* (Vol. 70, pp. 104–136). Elsevier B.V. https://doi.org/10.1016/j.mattod.2023.10.009

Bhaiyya, M., Pattnaik, P. K., & Goel, S. (2021). Simultaneous detection of Vitamin B12 and Vitamin C from real samples using miniaturized laser-induced graphene based electrochemiluminescence device with closed bipolar electrode. *Sensors and Actuators A: Physical*, *331*, 112831. https://doi.org/10.1016/j.sna.2021.112831

Coelho, J., Correia, R. F., Silvestre, S., Pinheiro, T., Marques, A. C., Correia, M. R. P., Pinto, J. V., Fortunato, E., & Martins, R. (2023). Paper-based laser-induced graphene for sustainable and flexible microsupercapacitor applications. *Microchimica Acta*, *190*(1). https://doi.org/10.1007/s00604-022-05610-0

de la Roche, J., López-Cifuentes, I., & Jaramillo-Botero, A. (2023). Influence of lasing parameters on the morphology and electrical resistance of polyimide-based laser-induced graphene (LIG). *Carbon Letters*, *33*(2), 587–595. https://doi.org/10.1007/s42823-022-00447-2

Guo, W., Xia, Y., Zhu, Y., Han, S., Li, Q., & Wang, X. (2023). Laser-induced graphene based triboelectric nanogenerator for accurate wireless control and tactile

pattern recognition. *Nano Energy*, *108*. https://doi.org/10.1016/j.nanoen.2023.108229

Hong, S., Kim, J., Jung, S., Lee, J., & Shin, B. S. (2023). Surface Morphological Growth Characteristics of Laser-Induced Graphene with UV Pulsed Laser and Sensor Applications. *ACS Materials Letters*, *5*(4), 1261–1270. https://doi.org/10.1021/acsmaterialslett.2c01222

John Jeya Kamaraj, J. J., Rajaji, U., Perumal, S., Muthu, S. P., Perumalsamy, R., & Liu, T. Y. (2024). Smart electrochemical determination of food additive (Propyl gallate) in edible oil and chicken samples based on CoSe2@FeS2 nanocomposite modified laser induced graphene electrode. *Journal of the Taiwan Institute of Chemical Engineers*, *162*. https://doi.org/10.1016/j.jtice.2024.105601

Kwak, D., Kim, H., Jang, S., Kim, B. G., Cho, D., Chang, H., & Lee, J. O. (2024). Investigation of Laser-Induced Graphene (LIG) on a Flexible Substrate and Its Functionalization by Metal Doping for Gas-Sensing Applications. *International Journal of Molecular Sciences*, *25*(2). https://doi.org/10.3390/ijms25021172

Li, Y., Peng, S., Zhu, T., Kong, S., Li, H., Cui, J., Niu, B., & Wu, D. (2023). Laser-induced reduction and pattern regulation of graphene oxide film with high biosafety for wearable micro-supercapacitors. *Journal of Alloys and Compounds*, *969*. https://doi.org/10.1016/j.jallcom.2023.172285

Liu, H., Chen, K., Wu, R., Pan, S., & Zhang, C. (2023). Laser-Induced Graphene-based Flexible Substrate with Photothermal Conversion and Photoresponse Performance on Polyimide Film. *ACS Applied Materials*

and Interfaces, *15*(39), 46550–46558. https://doi.org/10.1021/acsami.3c10729

Liu, X., Wang, X., Li, J., Qu, M., Kang, M., & Zhang, C. (2023). Nonmodified Laser-Induced Graphene Sensors for Lead-Ion Detection. *ACS Applied Nano Materials*, *6*(5), 3599–3607. https://doi.org/10.1021/acsanm.2c05307

Mostaccio, A., Antonelli, G., Bragaglia, M., Martinelli, E., & Marrocco, G. (2023). Comparative Evaluation of Laser-Induced Graphene (LIG) Traces on Polyimide Under Soft and Hard Stress for IoT Applications. *IEEE Journal on Flexible Electronics*, *2*(3), 256–264. https://doi.org/10.1109/jflex.2023.3265356

Movaghgharnezhad, S., Kim, M., Min Lee, S., Jeong, H., Kim, H., Gak Kim, B., & Kang, P. (2023). Highly sensitive photodetector based on laser-generated graphene with 3D heterogeneous multiscale porous structures. *Materials and Design*, *231*. https://doi.org/10.1016/j.matdes.2023.112019

Nag, A., Mukhopadhyay, S. C., & Kosel, J. (2017). Sensing system for salinity testing using laser-induced graphene sensors. *Sensors and Actuators, A: Physical*, *264*, 107–116. https://doi.org/10.1016/j.sna.2017.08.008

Ouedraogo, B., Baachaoui, S., Tall, A., Tapsoba, I., & Raouafi, N. (2023). Laser-induced graphene electrodes on polyimide membranes modified with gold nanoparticles for the simultaneous detection of dopamine and uric acid in human serum. *Microchimica Acta*, *190*(8). https://doi.org/10.1007/s00604-023-05909-6

Wang, L., Wang, Z., Bakhtiyari, A. N., & Zheng, H. (2020). A comparative study of laser-induced graphene by co2 infrared laser and 355 nm ultraviolet (Uv) laser.

Micromachines, *11*(12), 1–9. https://doi.org/10.3390/mi11121094

Wang, Y., Han, C., Zhou, Y., Ke, C., Fan, Y., Yang, Y., Chen, Z., & Wang, Y. (2023). Laser direct writing of graphene photodetector with a wide spectral detection from the visible to the infrared. *Carbon Trends*, *11*. https://doi.org/10.1016/j.cartre.2023.100255

Wanjari, V. P., Reddy, A. S., Duttagupta, S. P., & Singh, S. P. (2023). Laser-induced graphene-based electrochemical biosensors for environmental applications: a perspective. In *Environmental Science and Pollution Research* (Vol. 30, Issue 15, pp. 42643–42657). Springer Science and Business Media Deutschland GmbH. https://doi.org/10.1007/s11356-022-21035-x

Yang, L., Yan, J., Meng, C., Dutta, A., Chen, X., Xue, Y., Niu, G., Wang, Y., Du, S., Zhou, P., Zhang, C., Guo, S., & Cheng, H. (2023). Vanadium Oxide-Doped Laser-Induced Graphene Multi-Parameter Sensor to Decouple Soil Nitrogen Loss and Temperature. *Advanced Materials*, *35*(14). https://doi.org/10.1002/adma.202210322

Yao, J., Liu, L., Zhang, S., Wu, L., Tang, J., Qiu, Y., Huang, S., Wu, H., & Fan, L. (2023). Metal-incorporated laser-induced graphene for high performance supercapacitors. *Electrochimica Acta*, *441*. https://doi.org/10.1016/j.electacta.2022.141719

Zhang, Q., Zhang, F., Liu, X., Yue, Z., Chen, X., & Wan, Z. (2023). Doping of Laser-Induced Graphene and Its Applications. In *Advanced Materials Technologies* (Vol. 8, Issue 16). John Wiley and Sons Inc. https://doi.org/10.1002/admt.202300244

Zhang, S., Zhao, W., Zeng, J., He, Z., Wang, X., Zhu, Z., Hu, R., Liu, C., & Wang, Q. (2023). Wearable non-invasive glucose sensors based on metallic nanomaterials. In *Materials Today Bio* (Vol. 20). Elsevier B.V. https://doi.org/10.1016/j.mtbio.2023.100638

Zhu, J., Liu, S., Hu, Z., Zhang, X., Yi, N., Tang, K., Dexheimer, M. G., Lian, X., Wang, Q., Yang, J., Gray, J., & Cheng, H. (2021). Laser-induced graphene non-enzymatic glucose sensors for on-body measurements. *Biosensors and Bioelectronics*, *193*. https://doi.org/10.1016/j.bios.2021.113606

Zou, Y., Zhong, M., Li, S., Qing, Z., Xing, X., Gong, G., Yan, R., Qin, W., Shen, J., Zhang, H., Jiang, Y., Wang, Z., & Zhou, C. (2023). Flexible Wearable Strain Sensors Based on Laser-Induced Graphene for Monitoring Human Physiological Signals. *Polymers*, *15*(17). https://doi.org/10.3390/polym15173553

MEASUREMENT OF RF RADIATION POLLUTION LEVEL IN THE CORRIDORS OF KSÜ MEDICAL FACULTY HOSPITAL AND CALCULATION OF RADIATION DOSE INDEX

Ömer SÖĞÜT[1]

Esra Demirkol ÖZTAŞ[2]

1. INTRODUCTION

Non-ionizing electromagnetic field radiation (EMF) has wave-like properties and consists of a combination of electric and magnetic fields. All living things are exposed to natural electromagnetic radiation as well as artificial radiation from birth to death. With the development of various electronic systems due to developing science and technology, people have been increasingly exposed to electromagnetic fields (EMF). The dizzying developments in communication technology, especially in the field of mobile communication, have increased radiofrequency (RF) radiation exposure. The worldwide proliferation of global systems for mobile communication (GSM) has caused also concern regarding the possible adverse health effects of RF electromagnetic fields (Remondini et al., 2006). Smart mobile phones are devices that are part of every moment of life and are used for countless purposes such as communication, entertainment, navigation, education, all

[1] Prof. Dr., Kahramanmaraş Sütçü İmam University, Faculty of Science, Department of Physics, 46100 Kahramanmaraş, osogut@ksu.edu.tr, ORCID: 0000-0003-1987-1116.

[2] Kahramanmaraş Sütçü İmam University, Faculty of Science, Department of Physics, 46100 Kahramanmaraş, dmrkolesra@gmail.com, ORCID: 0000-0002-2761-4120.

banking transactions and controlling some electronic devices. However, every technology has its negatives as well as its positive benefits. One of the most important questions to be resolved has been whether such devices emit radiation and cause adverse health effects.

Despite the concerns, research into improving mobile communications has not stopped. In mobile communication, the abbreviation G, which means generation in English, was used to represent cellular communication technology. The first cellular communication technology used in mobile communication was 1G and this technology was called global system for mobile communications or in short GSM. GSM technology has evolved from 1G to 5G to create a faster and higher quality communication standard from past to present. Today, the frequencies of mobile phones used are in the frequency band of electromagnetic fields called RF and microwaves, which are between 3 kHz and 300 GHz. However, 5G technology uses higher frequency and therefore higher energy millimetres waves (MMW) and terahertz frequency waves (Sacco et. al., 2021; Küçükbağrıaçık and Büyükatalay, 2021). That is, the mobile communication technologies up to 4G use sub-3 GHz frequency bands. However, in 5G, frequency bands are divided into two as FR1 and FR2. FR1 expresses the band between 410 MHz and 7.125 GHz, while FR2 refers to the band between 24.25 GHz and 52.5 GHz (web1). The development of communication technologies, especially the use of higher frequencies and energies for communication in mobile phones and their broadcasting towers (base stations), causes people to be exposed to more RF radiation (i.e. non-ionizing radiation) (Ali and Al-Naamany, 2002). The potential health risks of radiofrequency electromagnetic fields emitted by electromagnetic devices are still not fully understood by the public (Kotb et. al., 2018). For this reason, the number of studies conducted to determine the

negative effects of electromagnetic fields on human health has increased rapidly. On May 31, 2011, the World Health Organization reported that continuous mobile phone use may pose a long-term health risk and may have dangerous carcinogenic effects (WHO, 2011). In a study conducted by Goldwein and Aframian in 2010, the effects of mobile phones on subauricular salivary gland secretion were investigated and it was reported that high saliva rates and decreased protein secretion occurred in the glands after exposure (Goldwein and Aframian, 2010). In 2008, Djeridane et al. investigated the effects of RF radiation from GSM-900 mobile phones on the circadian patterns of pituitary, adrenal and gonadal hormones in men and the growth hormone and cortisol were reported to decrease in the hormones by 28% and 12% at approximately maximum levels after a period of radiation exposure compared with the pre-exposure period (Djeridane et al., 2008). In 2013, the SAR and temperature distributions of the human eye were investigated with EM field exposure (Wessapan and Rattanadecho P., 2013). This study examined the relationship between two mobile phone usage activities and initial mobile phone use and subsequent headache and reported that headaches and migraines were triggered because of exposure to radiofrequency electromagnetic fields (RF-EMFs) due to long-term mobile phone use, especially text messaging (Traini et al., 2024). There have been many studies in the literature on headache, tinnitus, and hearing loss. (Auvinen et al., 2019; Oftedal et al., 2007; Frei et al., 2012; Schüz et al., 2009; Vahedi and Saiphoo, 2018; Smitherman et. al., 2013; Sudan et. al., 2013). There are various studies in the literature regarding the adverse effects of exposure to RF radiation due to mobile phone use on human health (Jung and Rogers, 2024; Auvinen et al., 2024; Elwood et. al., 2022; Schüz et al., 2006; Jayarajua et. al., 2023; Durusoy and Hassoy, 2019; Ta-Chiu et al., 2015; Söğüt

and Eyicil, 2021; Fattahi-Asl et al., 2012; Roosli and Hug, 2011).

The aim of this research is to measure the RF radiation pollution level in the corridors of KSU Medical Faculty hospitals and to calculate the dose index. One of its important goals is also to raise awareness about RF-based non-ionizing radiation pollution and its adverse effects.

2. MATERIAL AND METHODS

2.1. Making Measurements

Kahramanmaraş Sütçü İmam University (KSÜ) Faculty of Medicine is built on a closed area of 98.562 square meters; it consists of 5 polyclinics, 9 dormitory blocks, a conference hall, and an administrative building. KSÜ Faculty of Medicine has a bed capacity of approximately 600 and it can be said that the number of patients visiting the polyclinics on a daily basis is around 3000 people. In order to define the level of RF-induced electromagnetic field pollution in the polyclinic corridors of KSÜ Faculty of Medicine Hospital, equivalent plane wave power density (S), electric field strength (E) and magnetic field strength (H) measurements were made. Each corridor was divided into three equal parts, and three measurement points were determined. The measurements were made on Mondays, Tuesdays, Wednesdays, Thursdays, and Fridays at 08:00-09:01, 10:00-11:01, 12:00-13:01, 14:00-15:01 and 16:00-17:01. In the measurements, NARDA NBM-550 electromagnetic field meter with a frequency range of 100kHz-6GHz and a probe coded EF0691 were used. A photograph of the NARDA NBM-550 electromagnetic field meter and a probe coded EF0691 is given in Figure 1. Measurements were made three times at each point for statistical purposes, and as suggested by the Information and Communication Technologies Authority (BTK) and the

International Commission on Non-Ionizing Radiation Protection ICNIRP, each measurement time should be at least 6 minutes for a meaningful result. However, in this study, the measurement period was selected as 8 minutes (BTK, 2011; ICNIRP, 2009).

Figure 1. NARDA NBM-550 Electromagnetic Field Meter and Its Probe Coded EF0691

2.2. Making Calculations

Using the measured E value, the values of H and S were calculated with the following equations (IEEE Std C95.1, 1999).

$$S = \frac{E^2}{377} \quad (1)$$

$$H = \sqrt{\frac{S}{377}} \quad (2)$$

where S(W/m^2) represents the equivalent plane wave power density and H (A/m) represents the magnetic field strength. 377 represent the resistance of empty space (medium) and its unit is Ohm. the E, H and S values are given in Tables 1-3, respectively. The radiation dose index was calculated using the average values of the electric field strength measured or the average values of the calculated equivalent plane wave power density in the corridors of the KSU Faculty of Medicine (Szmigielski and Kubacki, 2000). For employees of KSÜ Faculty of Medicine, the T period was taken as 8 hours (equal to working hours). The average value of E at time T can be calculated by using the following equation.

$$\mathrm{E_{or}} = \sqrt{\frac{1}{\mathrm{T}}} \sum \mathrm{E_i}\, \mathrm{t_i} \quad (3)$$

where E_i is the rms (root mean square) electric field intensity measured at time t_i, and t_i is the sampling time. Radiation dose (D) can be calculated using the following equations depending on the S_i or E_i values in the unit (Wxh)/m^2 (Szmigielski ve Kubacki, 2000).

$$D = \sum S_i\, t_i \quad (4)$$

$$D = \frac{1}{Z_0} \sum E_i^2 t_i \quad and\ Z_0 = 377\Omega \quad (5)$$

$$D = S_{ort}T \quad (6)$$

$$D = \frac{1}{Z_0} E_{ort}^2 \, T \quad (7)$$

$$RDI = \frac{D}{D_n} \quad (8)$$

D_n represents the maximum allowable radiation dose and it can be calculated in the following the equations:

$$D_n = S_n T \; or \; D_n = \frac{1}{Z_0} E_n^2 T \quad (9)$$

where S_n and E_n are the respective values of S or E defined in safety standards for the electromagnetic field frequencies at which the RDI is calculated or measured.

$$RDI = \frac{\sum S_i t_i}{S_n \, T} \; or \; RDI = \frac{\sum E_i^2 t_i}{E_n T} \quad (10)$$

3. RESULTS AND DISCUSSION

To determine the level of RF-induced electromagnetic field pollution in the polyclinic corridors of KSÜ Faculty of Medicine Hospital, the electric field strength (E) measurements were made. Using the measured electric field strength data, the magnetic field strength and equivalent plane wave power density values were calculated. The measured E, and calculated H and S values are given in Table 1-3, respectively.

Table 1. Electric Field Strength, E (V/m) (mean±σ, n=3)

Hour	Monday		Tuesday		Wednesday		Thursday		Friday	
	E_{mean}	E_{maxs}	E_{mean}	E_{maxs}	E_{mean}	E_{maxs}	E_{mean}	E_{maxs}	E_{mean}	E_{maxs}
08:00-09:01	1.65 ±0.34	1.98 ±0.34	1.67 ±0.54	2.49 ±0.54	1.61 ±0.24	1.96 ±0.24	1.48 ±0.34	2.13 ±0.34	1.42 ±0.25	1.85 ±0.25
10:00-11:01	1.65 ±0.23	2.00 ±0.23	1.67 ±0.29	2.05 ±0.29	1.73 ±0.36	2.13 ±0.36	1.92 ±0.41	2.25 ±0.41	2.19 ±0.30	2.58 ±0.30
12:00-13:01	1.66 ±0.35	2.01 ±0.35	1.41 ±0.50	1.99 ±0.50	1.85 ±0.52	2.54 ±0.52	1.27 ±0.29	1.56 ±0.29	1.31 ±0.31	1.78 ±0.31
14:00-15:01	1.87 ±0.20	2.10 ±0.20	1.67 ±0.42	2.21 ±0.42	2.24 ±0.36	2.67 ±0.36	1.95 ±0.24	2.12 ±0.24	1.66 ±0.52	2.05 ±0.52
16:00-17:01	0.90 ±0.22	1.25 ±0.22	0.96 ± 0.34	1.49 ±0.34	0.89 ±0.16	1.01 ±0.16	0.95 ±0.27	1.31 ±0.27	1.41 ±0.53	2.17 ±0.53
Mean	**1.55**	**1.86**	**1.47**	**2.05**	**1.66**	**2.06**	**1.51**	**1.87**	**1.59**	**2.09**

Table 2. Magnetic Field Strength, H (A/m) (mean±σ, n=3)

Hour	Monday		Tuesday		Wednesday		Thursday		Friday	
	H_{mean} $x10^{-3}$	H_{maxs} $x10^{-3}$	H_{mean} $x10^{-3}$	H_{maxs} $x10^{-3}$	H_{mean} $x10^{-3}$	H_{maxs} $x10^{-3}$	H_{mean} $x10^{-3}$	H_{maxs} $x10^{-3}$	H_{mean} $x10^{-3}$	H_{maxs} $x10^{-3}$
08:00-09:01	4.38 ±0.10	5.25 ±0.92	4.43 ±0.82	6.61 ±0.97	4.27 ±0.13	5.20 ±0.17	3.93 ±0.11	5.65 ±0.12	3.77 ±0.94	4.91 ±0.84
10:00-11:01	4.38 ±0.10	5.31 ±0.92	4.43 ±0.82	5.44 ±0.97	4.59 ±0.13	5.65 ±0.17	5.09 ±0.11	5.97 ±0.12	5.81 ±0.94	6.84 ±0.84
12:00-13:01	4.41 ±0.10	5.33 ±0.92	3.74 ±0.82	5.28 ±0.97	4.91 ±0.13	6.74 ±0.17	3.37 ±0.11	4.14 ±0.12	3.48 ±0.94	4.72 ±0.84
14:00-15:01	4.97 ±0.10	5.57 ±0.92	4.43 ±0.82	5.86 ±0.97	5.94 ±0.13	7.08 ±0.17	5.17 ±0.11	5.62 ±0.12	4.40 ±0.94	5.44 ±0.84
16:00-17:01	2.40 ±0.10	3.32 ±0.92	2.55 ±0.82	3.95 ±0.97	2.36 ±0.13	2.68 ±0.17	2.52 ±0.11	3.48 ±0.12	3.74 ±0.94	5.76 ±0.84
Mean	4.11	4.96	3.92	5.43	4.41	5.47	4.00	4.96	4.24	5.54

Table 3. Equivalent Plane Wave Power Density, S (W/m^2) (mean±σ, n=3)

Hour	Monday		Tuesday		Wednesday		Thursday		Friday	
	S_{mean} $x10^{-3}$	S_{maxs} $x10^{-3}$	S_{mean} $x10^{-3}$	S_{maxs} $x10^{-3}$	S_{mean} $x10^{-3}$	S_{maxs} $x10^{-3}$	S_{mean} $x10^{-3}$	S_{maxs} $x10^{-3}$	S_{mean} $x10^{-3}$	S_{maxs} $x10^{-3}$
08:00-09:01	7.22 ±0.26	10.40 ±0.30	7.40 ±0.21	16.45 ±0.82	6.88 ±0.40	10.19 ±0.63	5.81 ±0.30	12.03 ±0.40	5.35 ±0.33	9.08 ±0.36
10:00-11:01	7.22 ±0.26	10.61 ±0.30	7.40 ±0.21	11.15 ±0.82	7.94 ±0.40	12.03 ±0.63	9.78 ±0.30	13.43 ±0.40	12.72 ±0.33	17.65 ±0.36
12:00-13:01	7.40 ±0.26	10.71 ±0.30	5.27 ±0.21	10.51 ±0.82	9.08 ±0.40	17.11 ±0.63	4.28 ±0.30	6.46 ±0.40	4.55 ±0.33	8.40 ±0.36
14:00-15:01	9.28 ±0.26	11.70 ±0.30	7.40 ±0.21	12.96 ±0.82	13.31 ±0.40	18.91 ±0.63	10.09 ±0.30	11.92 ±0.40	7.31 ±0.33	11.15 ±0.36
16:00-17:01	2.15 ±0.26	4.15 ±0.30	2.45 ±0.21	5.89 ±0.82	2.10 ±0.40	2.71 ±0.63	2.40 ±0.30	4.55 ±0.40	5.27 ±0.33	12.49 ±0.36
Mean	6.65	9.52	5.98	11.39	7.86	12.20	6.47	9.68	7.04	11.75

The same limit values were accepted by ICNIRP and BTK as 64 V/m for E, 0.16 A/m for H and 10 W/m^2 for S. As

seen from Table 1-3, all the measured E values, and calculated H and S values are much smaller than the limit values determined by the International Commission on Non-Ionizing Radiation Protection (ICNIRP) and the Turkish Information Technologies and Communication Authority (BTK) (ICNIRP, 1998 and 2009; BTK, 2011). In addition, the radiation dose index (RDI) for working staff at KSÜ Faculty of Medicine was calculated (RDI=0.88), and RDI was found to be < 1. Therefore, it can be said that the RF electromagnetic field exposure of employees working at KSÜ Faculty of Medicine is lower than the permissible levels. It can be said that one of the most important sources of RF-based electromagnetic pollution in corridors and work areas are mobile phones, Wi-Fi devices and base stations. As a result, in this study, the obtained values of E, H and S are lower than the limit values defined by national and international institutions and organizations. However, it should not be forgotten that in radiation exposure, the duration of exposure is also very important in addition to the size of the radiation field. Therefore, radiation exposure should be protected as much as possible. As seen in Table 1 and Figure 2, the largest maximum electric field strength was measured as 2.67 V/m on Wednesday, while the smallest maximum electric field strength was measured as 1.01 V/m on Monday.

Figure 2. Variation of Average and Maximum Average Electric Field Strength According to Days

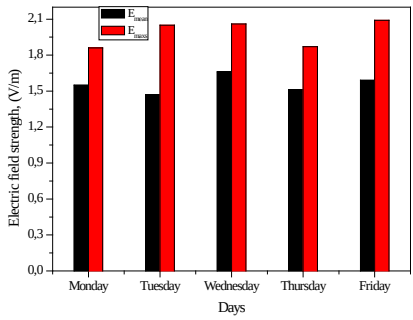

As seen in Table 2 and Figure 3, both the maximum magnetic field intensity ($7.08x10^{-3}$A/m) and the minimum maximum magnetic field intensity ($2.68x10^{-3}$A/m) were calculated for Wednesday from the data taken from the measurements made on Wednesday.

Figure 3. Variation of Average and Maximum Average Magnetic Field Strength According to Days

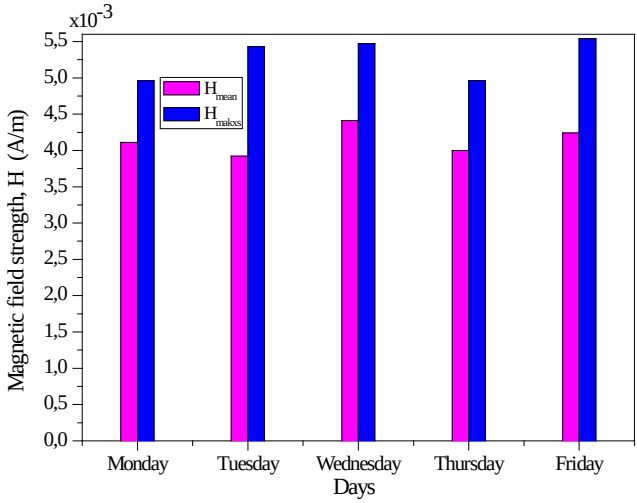

As seen in Table 3 and Figure 4, the largest maximum equivalent plane wave power density ($18.91x10^{-3}$ W/m^2) was calculated from the measurements made on Wednesday, while the smallest maximum equivalent plane wave power density ($2.71x10^{-3}$ W/m^2) was calculated from the measurements made for Monday. The reason why the values of E, H, and S are measured differently at certain hours and at different points in the corridor may be that the patients in the corridor at that moment are making phone calls. Apart from this, if there is base station signal boosters in the corridors, taking measurements at points far or close to them may also affect the measurement results.

Figure 4. Variation of Average and Maximum Average Equivalent Plane Wave Power Density According to Days

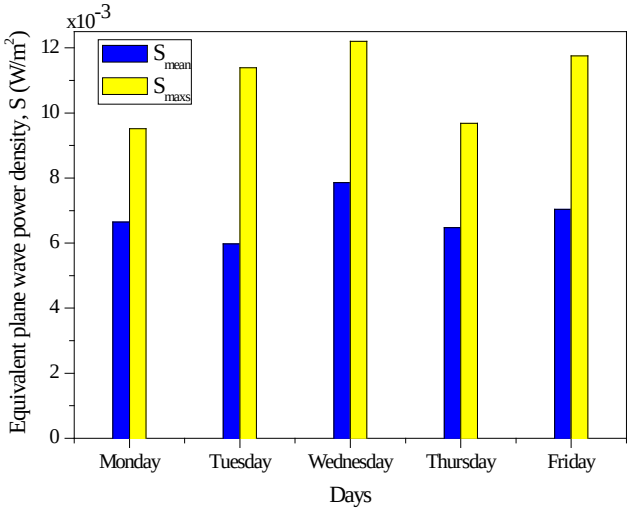

In the literature, there is research reporting that long-term exposure to electromagnetic field (EMF) radiation from mobile phones can cause health effects such as brain cancer, while there is also research reporting positive health effects such as increased bone healing and reduced toxic effects of chemotherapy (Aly et al., 2008; Makar et al., 2005; Satter et al., 1999). In addition, there are many studies in the literature that provide evidence about the adverse effects of exposure to mobile phone electromagnetic fields (Auvinen et al., 2019; Auvinen et al., 2024; Djeridane et al., 2008; Elwood et al., 2022; Jayarajua et al., 2023; Kotb et al., 2018; Ta-Chiu et al, 2015; Wessapan and Rattanadecho, 2013). For example, Hardell et al., (Harell et al., 2003) and Repacholi (Repacholi, 1997) reported that exposure to electromagnetic field radiation from mobile phones carries a risk of brain tumour formation. Another study reported that non-ionizing electromagnetic radiations can cause changes in both germ cells and nutritive environment and affect

other female reproductive parameters, which may lead to infertility. Jangid et al also reported that electromagnetic field radiation from mobile phones, laptops, Bluetooth devices, microwave ovens or wireless networks may have adverse effects on female fertility (Jangid et al., 2022). In a study conducted in 2003, Kesari et al. reported that radiofrequency electromagnetic fields emitted from mobile phones can damage the entire brain (Kesari et al., 2003).

Excessive use of wireless communication systems such as mobile phones can cause many health problems to users. Therefore, the general public, especially young users should be educated about the use of such communication tools and mass awareness campaigns should be initiated. International standardization organizations such as Institute of Electrical and Electronics Engineers(IEEE), International Committee on Electromagnetic Safety (ICES), Technical Committee 95 (TC95) and the International Commission on Non-Ionizing Radiation Protection (ICNIRP), have established safety guidelines and standards to protect people from excessive exposure to EMF. The institution that creates security guidelines and standards on this subject in our country is the Information Technologies and Communication Authority (BTK). BTK published a security guideline and standard determining the electromagnetic field intensity exposure limit values originating from electronic communication devices in the official gazette numbered 27912 on Thursday, April 21, 2011. These safety guidelines and standards set exposure limits for the general public and working in electrical and magnetic field environments such as healthcare professionals. Private and public institutions should also be informed about these security guidelines and standards. In addition, administrators of private and public educational institutions should request that radiation experts at universities hold informative meetings on the safe use of non-ionizing

radiation emitting devices such as mobile phones and protection from radiation. In this way, awareness can be raised among the general public about non-ionizing radiation exposure and protection methods.

4. CONCLUSION

Electric field strength (E), magnetic field strength (H) and equivalent plane wave power density (S) measurements of microwave-based radiation were made in all corridors of Kahramanmaraş Sütçü İmam University Medical Faculty polyclinics. Additionally, the radiation dose index was also calculated for hospital personnel serving in these corridors and for patients coming to the outpatient clinics on a daily basis. In this study, none of the measured electric field intensity (E), magnetic field intensity (H) and equivalent plane wave power density (S) values are greater than the limit values defined by neither BTK nor ICNIRP. The radiation dose index (RDI) for staff working at KSU Faculty of Medicine was calculated as 0.88 and the RDI was found to be less than 1. Since the RDI value is calculated as <1, it can be said that the RF electromagnetic field exposure of employees working at KSÜ Faculty of Medicine is lower than the permissible levels. That is, it can be said that the radiation exposure does not have any negative effects on health.

REFERENCES

Ali A.A., Al-Naamany A. M., 2002. Biological Effects of EM Radiations from Mobile Phones, Science and Technology 7, 45-53.

Aly A.A., Deris S.B., Zaki N., 2008. Research Review on the Biological Effect of Cell Phone Radiation on Human, International Conference on Innovations in Information Technology, doi:10.1109/innovations.2008.4781774

Auvinen A., Feychting M., Ahlbom A., Hillert L., Elliott P., Schüz J., Kromhout H., Toledano M.B., Johansen C., Poulsen A.H., Vermeulen R., Heinävaara S., Kojo K., Tettamanti G., 2019. Headache, tinnitus and hearing loss in the international Cohort Study of Mobile Phone Use and Health (COSMOS) in Sweden and Finland, International Journal of Epidemiology 48(5), 1567-1579.

Auvinen A., Poulsen A. H. Deltour I., Smith R. B., Heller J., Kromhout H., Huss A., Johansen C., Tettamanti G., Elliott P., 2024. Mobile phone use and brain tumour risk-COSMOS, a prospective cohort study, Feychting M., Schüz J., Toledano M.B., Vermeulen R., Environment International 185, 108552.

Avcı U., 2020. Yüksek Frekanslı Elektromanyetik Radyasyon ve Bitki Gelişimi, Recep Tayyip Erdoğan Üniversitesi Fen ve Mühendislik Bilimleri Dergisi1(1), 68-73.

Djeridane Y., Touitoua,Y., and de Seze R., 2008. Influence of Electromagnetic Fields Emitted by GSM-900 Cellular Telephones on the Circadian Patterns of Gonadal, Adrenal and Pituitary Hormones in Men, Radiation Research 169, 337-343.

Durusoy R., Hassoy H., 2019. Electromagnetic Fields from Mobile Phones and Their Base Stations-Health Effects,

Encyclopedia of Environmental Health (Second Edition), 300-314.

Elwood J.M., Win S.S., Aye P.S., Sanagou M., 2022. Trends in brain cancers (glioma) in New Zealand from 1995 to 2020, with reference to mobile phone use, Cancer Epidemiology 80, 102234.

Fattahi-Asl J., Baradaran-Ghahfarokhi M., Karbalae M., Baradaran-Ghahfarokhi H.R., 2012. Effects of Radiofrequency Radiation on Human Ferritin: An In-Vitro Enzymun Assay. J Med Signals Sens 2(4), 102-17.

Frei P., Mohler E., Braun-Fahrländer C., Fröhlich J., Neubauer G., Röösli M.,2012. Cohort study on the effects of everyday life radiofrequency electromagnetic field exposure on non-specific symptoms and tinnitus. Environ Int 38, 29-36.

Goldwein O., Aframian D.J., 2010. The influence of handheld mobile phones on human parotid gland secretion, Oral Diseases 16, 146-150.

Harell L., Carlberg M., Hansson M.K., 2006. Pooled analysis of two case-control studies on the use of cellular and cordless telephones and the risk of benign brain tumours diagnosed during 1997-2003, Int J Oncol 28, 509-518.

Information Technologies and Communication Authority (BTK), 2011. Regulation on determination, control and supervision of exposure limit values of electromagnetic field intensity originating from electronic communication devices according to international standards, prime ministry general directorate of legislation development and publication, 21 April 2011 Thursday Official Gazette Issue: 27912.

ICNIRP, 1998. Guidelines for Limiting Exposure to Time-Varying Electric, Magnetic, and Electromagnetic Fields (Up to 300 GHz), Health Physics 74(4), 494-522.

ICNIRP, 2009. International Commission on Non-Ionizing Radiation Protection (ICNIRP). Statement on the "Guidelines for limiting exposure to time-varying electric, magnetic and electromagnetic fields (up to 300 GHz).

Jangid P., Rai U., Sharma R. S., and Singh R., 2022. The role of non-ionizing electromagnetic radiation on female fertility: A review. International Journal of Environmental Health Research 33(4), 358–373.

Jayarajua N.,Kumar M. P., Sreenivasulu G.,Prasad T.L., Lakshmannad B., Nagalaksmi K., Madakka M., 2023. Mobile phone and base stations radiation and its effects on human health and environment-A review, Sustainable Technology and Entrepreneurship 2, 100031.

Jung S., Rogers M., 2024. Mobile phone adoption, deforestation, and agricultural land use in Uganda, World Development 179, 106618.

Kesari K. K., Siddiqui M.H., Meena R., Verma H.N., and Kumar S., 2003. Cell phone radiation exposure on brain and associated biological systems, Indian Journal of Experimental Biology 51, 187-200.

Küçükbağrıaçık K., Büyükatalay E.Ö., 2021. Yeni Nesil Cep Telefonu Frekansları ve Biyolojik Etkileri, Genel Tıp Dergisi 31(3), 309-312.

Kotb M.A., Ramadan H.S., Siam M.E., Abd-Elaziz M.M., Yasser I.K., 2018.Exposure to mobile phones and its biophysical, biochemical, and haematological effects, Proceeding of the 9th ICEE Conference 3-5 April 2018.

Makar V.R., Logani M.K., Bhanushali A., Kataoka M., Ziskin M.C., 2005. Effect of millimeter waves on natural killer cell activation, Bioelectromagnetics 26, 10-19.

Oftedal G., Straume A., Johnsson A., Stovner L.J., 2007. Mobile phone headache: a double-blind sham-controlled provocation study. Cephalalgia 27, 447-55.

Repacholi M.H., 1997. Lymphomas in E Mu-Pim1 Transgenic Mice Exposed to Pulsed 900 MHz Electromagnetic Fields, Radiation research 147(5), 631-40.

Remondini D., Nylund R., Reivinen J., de Gannes F. P., Veyret B., Lagroye I., Haro E., Trillo M.A., Capri M., Franceschi C., Schlatterer K., Gminski R., Fitzner R., Tauber R., Schuderer J., Kuster N., Leszczynski D., Bersani F., Maercker C., 2006. Gene expression changes in human cells after exposure to mobile phone microwaves, Proteomics 6, 4745-4754.

Roosli M., Hug K., 2011. Wireless communication fields and non-specific symptoms of ill health: a literature review. Wiener medizinische Wochenschrift 161(9-10), 240-50.

Satter S.S., Islam M.S., Rabbani K.S., Talukder M.S., 1999. Pulsed electromagnetic fields for the treatment of bone fractures, Bangladesh Med Res Counc Bull, 25, 6-10.

Smitherman T.A., Burch R., Sheikh H., Loder E., 2013.The prevalence, impact and treatment of migraine and severe headaches in the United States. Headache 53, 427-36.

Sudan M., Kheifets L., Arah O.A., Olsen J., 2013. Cell phone exposures and hearing loss in children. Paediatr Perinat Epidemiol 27, 247-57.

Schüz J., Jacobsen R., Olsen J.H., Boice Jr J.D., McLaughlin J. K., Johansen C., 2006. Cellular telephone use and cancer

risk: update of a nationwide Danish cohort, Journal of the National Cancer Institute 98 (23), 1707-1713.

Sacco G., Pisa S., Zhadobov M., 2021. Age-dependence of electromagnetic power and heat deposition in near-surface tissues in emerging 5G bands, Scientific Reports 11, 3983-3993.

Schüz P., Waldemar G., Olsen J.H., Johansen C., 2009. Risks for central nervous system diseases among mobile phone subscribers. PLoS One 24, e4389.

Söğüt Ö., Eyicil E., 2021. Measurement of Electromagnetic Pollution Level and Calculation of Radiation Dose Index throughout Malatya Street in Elbistan District of Kahramanmaraş, Erzincan University Journal of Science and Technology 14(1), 204-214.

Szmigielski S., Kubacki R. and Z. Ciolek., 2000. Radio Frequency Radiation Dosimetry and Its Relationship to the Biological Effects of Electromagnetic Fields, Application of Dosimetry in Military Epidemiologıcal Studies, Nato Science Partnership Subseries 3 (82), 459-471.

Traini E., Smith R.B., Vermeulen R., Kromhout H., Schüz J., Feychting M., Auvinen A., Poulsen A. H., Deltour I., Muller D.C., Heller J., Tettamanti G., Elliott P., Huss A., Toledano M.B., 2024. Headache in the international cohort study of mobile phone use and health (COSMOS) in the Netherlands and the United Kingdom, Environmental Research 248, 118290.

Ta-Chiu C., Chang Y.H., Chen C.C., Ko M.C., Li C.Y., 2015. Mobile phone use and health symptoms in children, Journal of the Formosan Medical Association 114, 598-604.

Vahedi Z., Saiphoo A., 2018.The association between smartphone use, stress and anxiety: a meta-analytic view. Stress Health 34, 347-58.

Wessapan T., Rattanadecho P., 2013. Specific absorption rate and temperature increase in the human eye due to electromagnetic fields exposure at different frequencies, International Journal of Heat and Mass Transfer 64, 426-435.

WHO, 2011. Danielle Dellorto, Cell phone use can increase possible cancer risk. CNN Cable News Network. Turner Broadcasting System, Inc. http://edition.cnn.com/2011/HEALTH/05/31/who.cell.phones/index.html.

web1: https://www.aselsan.com/tr/blog/detay/332/5g-nedir# (28 Ocak 2022).

FABRICATION AND CHARACTERIZATION OF METAL-POLYMER-SEMICONDUCTOR SCHOTTKY BARRIER DIODE USING A PCDTBT: F4-TCNQ INTERFACE LAYER AT DIFFERENT TEMPERATURES

H. Muzaffer ŞAĞBAN[1]

Özge TÜZÜN ÖZMEN[2]

1. INTRODUCTION

In the fields of electronics and optoelectronics, inorganic materials are extensively utilized as active components in various electronic devices, such as light-emitting diodes (LEDs), silicon-based field-effect transistors (FETs), and thin-film transistors (TFTs) [1]. However, when compared to inorganic semiconductors, organic electronic devices offer significant advantages due to several inherent benefits [2]. The primary reason for the widespread adoption of organic materials in semiconductor technologies is their ability to be easily synthesized through various techniques and their compatibility with straightforward production methods, such as spin coating and spray deposition. This versatility in manufacturing not only accelerates research and development processes but also significantly reduces production costs. Moreover, in the production of organic semiconductors with varying properties, numerous material attributes and parameters, such as molecular

[1] Asst. Prof. Opticianry, Vocational School, İstanbul Beykent Üniversitesi, 34500, İstanbul, TURKEY, huseyinsagban@beykent.edu.tr, ORCID: 0000-0001-8820-5622.

[2] Prof. Dr., Fundamental Sciences, İzmir Bakırçay Üniversitesi, 35665, İzmir, TURKEY, ozge.ozmen@bakircay.edu.tr, ORCID: 0000-0002-5204-3737.

weight, bandgap energy, molecular orbital energy levels, structural characteristics, and doping, can be altered [3,4]. This flexibility enables the cost-effective and straightforward production of organic semiconductor materials with diverse and enhanced properties. Given these advantages, the use and research of organic materials in modern optoelectronic and electronic technologies are rapidly increasing. Currently, the most prominent devices made from organic materials include organic light-emitting diodes (OLEDs), organic field-effect transistors (OFETs), organic photodiodes (OPDs), organic photovoltaics (OPVs), and Schottky barrier diodes (SBDs) [3].

One of the most widely used components in modern electronic devices is the diode. Among all types of diodes, Schottky barrier diodes (SBDs) hold particular importance due to their superior performance and ability to operate effectively at high frequencies [5]. Diodes operating at high frequencies often struggle to respond to changes in applied voltage, failing to switch between conducting and insulating states efficiently. However, SBDs excel in this regard, as they can rapidly respond to such changes even under high-frequency conditions. Another distinguishing feature of SBDs is their ability to enter the conducting state much more quickly, owing to their lower forward voltage requirement. Additionally, due to the reduced number of minority charge carriers, SBDs exhibit lower leakage current. These characteristics make SBDs more efficient compared to other diodes. Furthermore, with the advancement of organic technology, SBDs can now be produced using organic-based materials, allowing them to achieve high performance as well [6].

Metal-semiconductor (MS) contacts form the structure of Schottky barrier diodes (SBDs), with the diode's properties being influenced by factors such as the type and concentration of the semiconductor, the bandgap, and the work function of the

metal. Additionally, SBDs can be created by inserting an insulating or polymer layer between the metal and semiconductor surfaces, resulting in structures known as metal-insulator-semiconductor (MIS) or metal-polymer-semiconductor (MPS) configurations. Recently, there has been a significant increase in both experimental and theoretical studies focusing on MPS-type SBDs, particularly those incorporating a polymer layer between the metal and semiconductor surfaces [2].

MPS-type Schottky barrier diodes (SBDs) are fabricated by depositing a polymer layer onto a semiconductor substrate using various coating techniques, such as spin coating or spray coating, followed by the deposition of contacts on the front and back surfaces of the structure (Figure 1). In MPS-type SBDs, the inclusion of a polymer with a high dielectric constant between the metal and semiconductor layers allows for the regulation of charge transfer, leading to the production of higher-performance devices. The primary functions of these interfacial layers are to provide surface passivation, optimize the current-conduction mechanism, and prevent leakage currents. Metals with appropriate work functions are used to create rectifying and ohmic contacts in the preparation of MPS-type structures. If Φm represents the work function of the metal and Φs represents that of the semiconductor, a rectifying contact is formed for metal/n-type semiconductor contacts when $\Phi m > \Phi s$, while an ohmic contact is formed when $\Phi s > \Phi m$. Similarly, for metal/p-type semiconductor contacts, a rectifying contact occurs when $\Phi s > \Phi m$ and an ohmic contact is formed when $\Phi m > \Phi s$ [7-13].

Figure 1. Schematic Representation of an MPS Schottky Barrier Diode

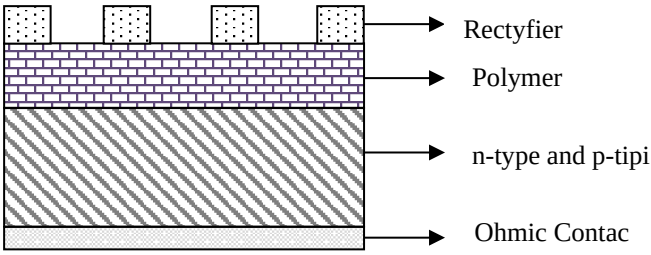

In this study, research was conducted on the fabrication and electrical characterization of MPS-structured Schottky barrier diodes (SBDs), given the advantages mentioned above. Considering these properties, PCDTBT (Poly[[9-(1-octylnonyl)-9H-carbazole-2,7-diyl]-2,5-thiophenediyl-2,1,3-enzothiadiazole-4,7-diyl-2,5-thiophenediyl], Poly[N-9′-heptadecanyl-2,7-carbazole-alt-5,5-(4′,7′-di-2-thienyl-2′,1′,3′-benzothiadiazole)]) was used as the primary material, and F4-TCNQ (2,3,5,6-Tetrafluoro-2,5-cyclohexadiene-1,4-diylidene)dimalononitrile, 7,7,8,8-Tetracyano-2,3,5,6-tetrafluoroquinodimethane) was used as the doping agent. SBDs were fabricated by preparing mixtures with a 1% doping ratio of PCDTBT to F4-TCNQ.

2. MATERIALS AND METHODS

In this study, n-type doped silicon (Si) crystals were used as the semiconductor material. The organic polymer material was deposited onto the n-type Si substrate using the spin coating technique (Figure 2). As shown in the figure, after the production of the polymer/semiconductor material, the Schottky barrier diode (SBD) was fabricated by depositing the top and bottom metal contacts using a thermal evaporation system. Gold (Au) and silver (Ag) metals were chosen for the metal contacts,

considering their work functions in relation to the doping type of the materials used.

Figure 2. Stages of the Fabrication Process for MPY Schottky Barrier Diodes

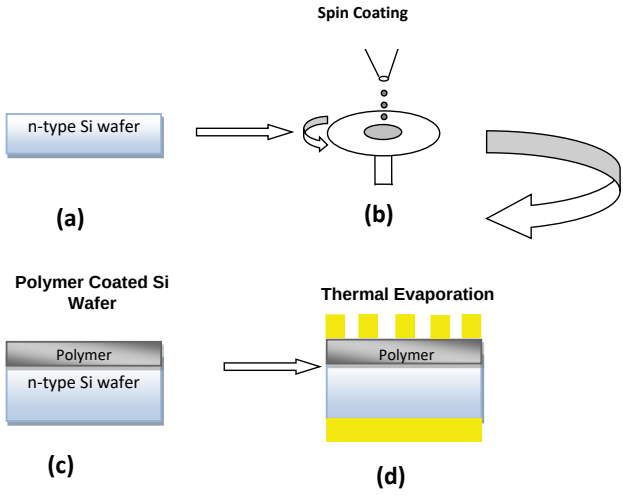

The n-type single-crystal Si wafers used as substrates were produced using the Czochralski (Cz) method with <100> orientation. The Si wafers for SBD fabrication were purchased with a thickness of 350 ± 25 μm and a resistivity of 4.8 Ω·cm. The wafers were cut into 1x1 cm squares using a diamond cutter. Subsequently, the wafers were cleaned, and a thermal evaporation system was used to deposit a high-purity Ag layer of approximately 2500 Å thickness on the matte side of the wafers to form ohmic contacts using a mask. The organic materials PCDTBT and F4-TCNQ, used as the interfacial layer, were mixed in chlorobenzene at concentrations of 20 mg/ml and 0.01 mg/ml, respectively, and stirred at 60°C for approximately 3 hours. The resulting mixtures were placed in a tube with a 1% F4-TCNQ doping ratio and stirred for 24 hours. The solutions were then spin-coated onto the shiny side of the Si wafers for 30

seconds at 1500 rpm to achieve a thickness of approximately 160 nm. Finally, rectifying contacts were deposited on top of the coated organic surfaces using a thermal evaporation method. High-purity Au was used to obtain a thickness of approximately 2500 Å for the rectifying contacts.

The analysis of the fabricated SBDs was performed through measurements conducted under both dark and illuminated conditions within a closed-circuit cryostat, at a vacuum of 1x10^-4 mbar, and across a voltage range of -5V to +5V. Measurements under illumination were carried out with a lighting intensity of 1000 W/m². Temperature-dependent I-V measurements of the SBDs were performed within the range of 200K to 325K in 25K increments. From the dark, illuminated, and temperature-dependent I-V measurements, the ideality factors, saturation currents, and barrier heights of the SBDs were determined.

3. RESULTS AND DISCUSSION

In this study, electrical characteristics of the Schottky barrier diode (SBD) produced with a 1% doping ratio of PCDTBT:F4-TCNQ polymer blend were conducted under both illumination and varying temperatures. Initially, dark and illuminated I-V measurements of the Au/PCDTBT:F4-TCNQ/n-Si heterojunction SBD were performed at room temperature under vacuum. Subsequently, temperature-dependent measurements of the SBD were carried out under vacuum within the temperature range of 200K to 325K in 25K increments. Based on the obtained data, fundamental electrical parameters such as the ideality factor (n), saturation current (I_0), and barrier height ($\emptyset_B$) were calculated to determine the characteristics of the produced SBDs.

In this study, dark and illuminated measurements of the Au/PCDTBT:F4-TCNQ/n-Si SBD were conducted within a closed-circuit cryostat at a pressure of approximately $1x10^{-4}$ mbar, across a voltage range of -5V to +5V in the dark, and under illumination of 1000 W/m². Figure 3 shows the dark and illuminated I-V curves of the diode produced using a 1% PCDTBT:F4-TCNQ doping ratio.

Figure 3. Dark and Illuminated I-V Characteristics of the Heterojunction SBD with 1% PCDTBT:F4-TCNQ Doping Ratio

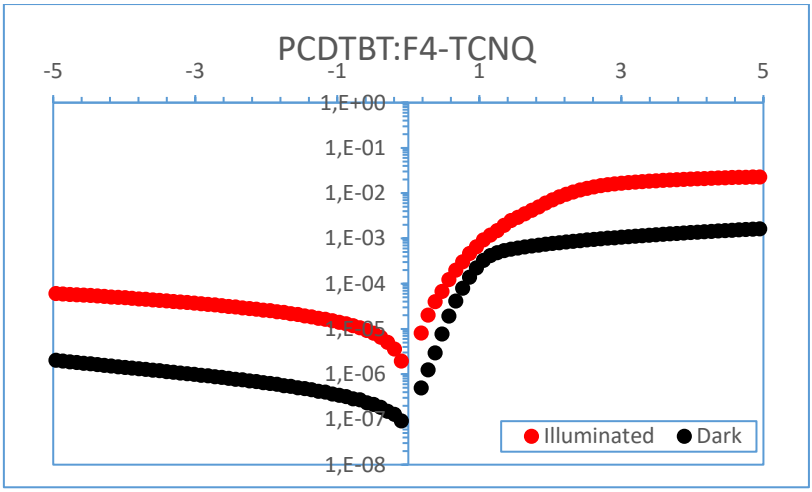

In Figure 3, it is observed that there is an increase in current values in both the negative and positive regions when the diode is exposed to light. This increase is attributed to the generation of a higher number of electron-hole pairs when light is incident on the Schottky Barrier Diode (SBD) [16]. Additionally, the increase in conductivity under illumination is partly due to the excitation of trap levels within the bandgap, which enhances the contribution of charge carriers to the conduction process [17]. The increase in conductivity is more pronounced in the negative region under illumination. This is because the minority charge carriers, generated due to the illumination, significantly contribute to the conduction when

influenced by the electric field present during reverse bias. This enhanced conductivity in the negative region further indicates that SBDs exhibit photodiode characteristics under light exposure.

The ideality factor (n), barrier height ($\emptyset_B$), and saturation current (I_o) values of the fabricated Schottky Barrier Diodes (SBDs) have been calculated. The ideality factors were determined using the slope of the linear region in the I-V characteristics, as given by the following equation [3]:

$$n = \frac{q}{kTtan\theta} \tag{3.1}$$

Based on the calculations using this equation, the ideality factor of the diode with 1% PCDTBT:F4-TCNQ doping was found to be 4.20 in the dark and 6.25 under illumination. An increase in the ideality factor was observed with the effect of illumination.

The barrier height ($\emptyset_B$) values were determined using the following equation:

$$\emptyset_B = \frac{kT}{q} \ln \left(\frac{AA^*T^2}{I_o}\right) \tag{3.2}$$

In the above equation, Io represents the saturation current, which corresponds to the current value at the point where the voltage is zero on the I-V curve. For the SBD with 1% PCDTBT:F4-TCNQ doping, the saturation current was found to be $9.49\times10{-}8$ in the dark and $1.84\times10{-}6$ under illumination.

Using the saturation current values and Equation 3.2, the barrier height ($\emptyset_B$) values were calculated. For the diode with 1% PCDTBT:F4-TCNQ doping, the $\emptyset_B$ value was found to be

0.82 eV in the dark and 0.74 eV under illumination. All the calculated values are presented in Table 1.

Table 1. The values of ideality factor (n), saturation current (Io), and barrier height ($\emptyset_B$) obtained for the SBD with 1% PCDTBT:F4-TCNQ doping under dark and illuminated conditions.

	Dark			Illuminated		
	n	$I_o(A)$	$\emptyset_B(eV)$	*n*	$I_o(A)$	$\emptyset_B(eV)$
PCDTBT:F4-TCNQ	4.20	$9{,}49\text{x}10^{-8}$	0.82	6.25	$1{,}84\text{x}10^{-6}$	0.74

As seen in Table 1, under the influence of illumination, an increase in ideality factors and saturation currents is observed, while the $\emptyset_B$ values show a slight decrease. The increase in saturation currents is due to the generation of a greater number of charge carriers under the effect of light. This increase, coupled with the contribution of more charge carriers through quantum tunneling mechanisms, leads to a deviation from ideality in the diodes, resulting in higher ideality factors. Additionally, under illumination, charge carriers gain more energy, allowing them to encounter lower potential barriers. This observed phenomenon is attributed to the reconfiguration of charge carriers under illumination, the density of interface states, and the non-uniform distribution of barrier heights within the structure [1,18].

For the fabricated SBD, the rectification ratio (RR) was calculated using the ratio of the forward current to the reverse current. By comparing the current values at +3V and -3V bias voltages, the rectification ratio for the SBD with 1% PCDTBT:F4-TCNQ doping was found to be 1.37×10^3.

Figure 4 shows the I-V characteristics of the SBD fabricated with 1% PCDTBT:F4-TCNQ doping over the temperature range of 200K to 325K.

Figure 4. Temperature-dependent I-V characteristics of the heterojunction SBD with 1% PCDTBT:F4-TCNQ doping.

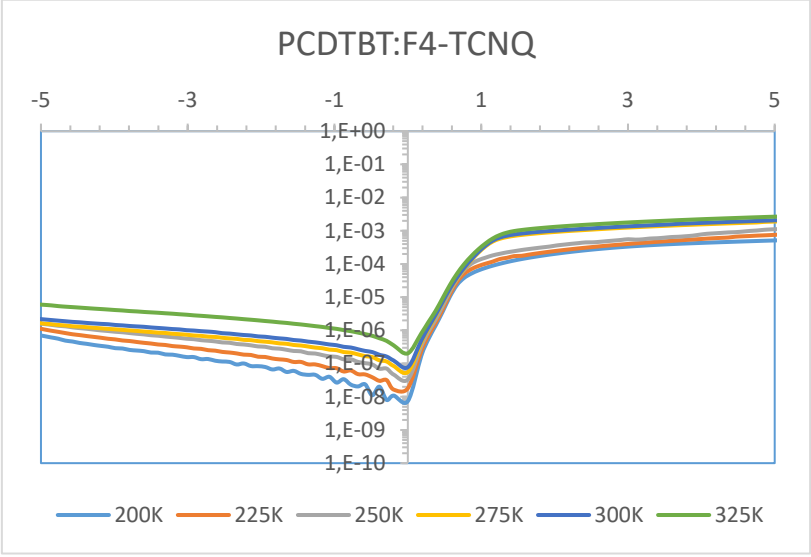

Using the I-V curves obtained at temperature intervals of 25K within the 200K to 325K range, the ideality factors, barrier heights, and saturation currents were determined. The values obtained are presented in Table 2.

Table 2. Values obtained from the temperature-dependent I-V curves of the diode with a 1% PCDTBT:F4-TCNQdoping ratio.

PCDTBT:F4-TCNQ	**200**	**225**	**250**	**275**	**300**	**325**
n	5.77	5.29	4.86	4.50	4.20	4.03
I_o(A)	3.51E-8	5.03E-8	6.89E-8	8.055E-8	9.49E-8	1.57E-7
$\emptyset_B$(eV)	0.55	0.61	0.68	0.75	0.82	0.87

Upon examining the data in Table 2, it is observed that with increasing temperature, the ideality factors decrease, while the barrier height and saturation currents increase. For the Schottky Barrier Diode (SBD) with a 1% PCDTBT:F4-TCNQ doping ratio, the ideality factor decreases from 5.77 to 4.03, the barrier height increases from 0.55 eV to 0.87 eV, and the saturation current rises from 3.51×10^{-8} A to 1.57×10^{-7} A.

Figure 5 presents the graphs depicting the variation in ideality factors and barrier heights with temperature for the Schottky Barrier Diode (SBD) with a 1% PCDTBT:F4-TCNQ doping ratio.

Figure 5. Temperature-dependent variation in the ideality factor and barrier height for the diode fabricated with a 1% PCDTBT:F4-TCNQ doping ratio.

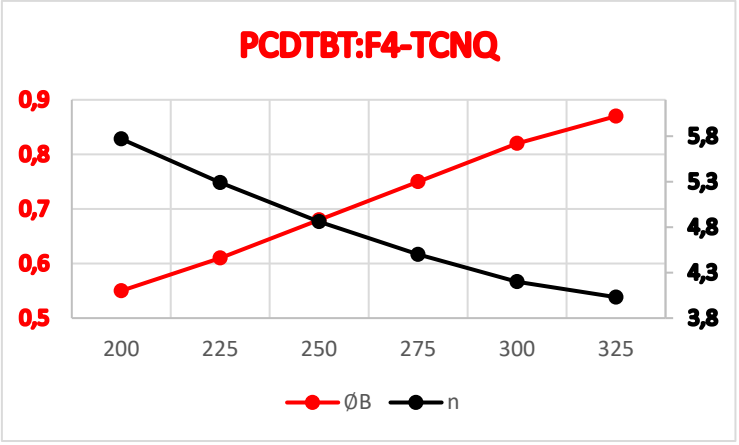

As the temperature increases, a decrease in the ideality factors of the diode is observed, while the barrier heights rise, consistent with findings in the literature [19,20]. This temperature-dependent behavior of the Schottky Barrier Diode (SBD) indicates that thermionic emission is not the sole mechanism governing current transport. At lower temperatures, charge carriers have less energy, resulting in a lower maximum barrier height that they can overcome. In this scenario, current tends to dominate in localized regions of the barrier heights, leading to an increase in the ideality factor. Furthermore, due to the insufficient energy of electrons, recombination decreases, causing a reduction in current values [19,20]. However, as the temperature rises, charge carriers gain significantly more energy, which leads to a proportional increase in the barrier height they can overcome.

4. CONCLUSION

In this study, an Au/PCDTBT:F4-TCNQ /n-Si Schottky Barrier Diode (SBD) with a 1% PCDTBT:F4-TCNQ doping ratio was fabricated. The current-voltage (I-V) measurements of the produced SBD were initially conducted in a closed-circuit cryostat under a vacuum of $1x10^{-4}$ mbar, in both dark and illuminated conditions (1000 W/m²), within a voltage range of -5V to +5V. Subsequently, temperature-dependent measurements were performed within the same vacuum conditions, over a temperature range of 200K to 325K, and a voltage range of -5V to +5V.

The experiments conducted in both dark and illuminated conditions revealed an increase in current values under both reverse and forward bias when exposed to light. This increase in current can be attributed to several factors, including the generation of more electron-hole pairs due to illumination, the involvement of charge carriers from the forbidden energy gap in the conduction process, and the reduction in series resistance of the diode due to the light exposure.

Based on the results obtained from temperature-dependent measurements, it was observed that both reverse and forward bias current values increase with rising temperature. Additionally, an increase in temperature leads to a decrease in ideality factors and an increase in barrier heights. This phenomenon can be attributed to the fact that at lower temperatures, charge carriers have less energy, resulting in a lower barrier height that they can overcome, which in turn causes deviations from ideal diode behavior.

5. ACKNOWLEDGEMENT

This work was supported by the Düzce University Scientific Research Projects (Project No: BAP 2018.05.02.721).

REFERENCES

[1] Sze S.M., Ng K.K., "Physics of Semiconductor Devices", 3rd Ed., John Wiley & Sons, Hoboken, New Jersey (2007).

[2] Gaojie Lu, "Organic semiconductor", *University of Rochester* (2006).

[3] Tüzün Özmen Ö., "Effects of PCBM concentration on the electrical properties of the Au/P3HT:PCBM/n-Si (MPS) Schottky barrier diodes", *Microelectronics Reliability*, 54 (2014) 2766–2774.

[4] So F., "Organic Electronics; Materials, Processing, Devices and Applications", *CRC Press, Boca Raton*. (2010).

[5] R. Hackam, P. Piarrop., "Electrical Properties of Nickel-LowcDoped n-Type Gallium Arsenide Schottky-Barrier Diodes", *IEEE Transactions On Electron Devices*, ED-19, No. 12 (1972) 1231-1238

[6] S. Demirezen, Z. Sönmez, U. Aydemir, S. Altındal.," Effect of series resistance and interface states on the IeV, CeV and G/ueV characteristics in Au/Bi-doped polyvinyl alcohol (PVA)/n-Si Schottky barrier diodes at room temperature", *Current Applied Physics*, 12 (2012) 266-272.

[7] Li S.S., "Semiconductor Physical Electronics", 2nd Ed., Springer, (2006)

[8] Rhoderick E.H., Williams R.H., "Surfaces, Interfaces and Schottky Barriers, Metal-Semiconductor Contacts", 2nd Ed., *Clarendon Press, Oxford*, (1988).

[9] Wilson A. H., *Proc. R. Soc. Lond. A*, 133 (1931) 458.

[10] Sharma B.L., "Metal-Semiconductor Contacts Schottky Barrier Junctions and Their Applications", *Plenum Press, New York and London*, (1984).

[11] Özdemir A.F., Aldemir D.A., Kökçe A., Altındal S., *Synthetic Metals*, 159 (2009) 1427.

[12] Demirezen S., Altındal Ş., *Current Applied Physics*, 10 (2010) 1188.

[13] Rhoderick E.H., Williams R.H., "Metal-Semiconductor Contacts", 2nd Ed., Oxford *University Press, Oxford*, (1988).

[14] Liu J., Shao S., Fang G., Meng B., Xie Z., Wang L.," High-Efficiency Inverted Polymer Solar Cells with Transparent and Work-Function Tunable MoO_3-Al Composite Film as Cathode Buffer Layer", *Adv. Mater.* 24 (2012), 2774–2779.

[15] Han X., Wu Z., Sun B., *Organic Electronics*, 14 (2013) 1116.

[16] İ. Taşçıoğlu, U. Aydemir, Ş. Altındal ve T. Tunç, "Illumination dependent admittance characteristics of Au/Zinc Acetate doped Polyvinyl Alcohol (PVA: Zn)/n-Si Schottky Barrier Diodes (SBDs)", *International Congress On Advances In Applied Physics and Materials Science,* c. 1400, ss. 307-311, 2011.

[17] S. Alialy, H. Tecimer, H. Uslu ve Ş. Altındal, "A comparative study on electrical characteristics of Au/n-Si Schottky Diodes with and without Bi-doped PVA interfacial layer in dark and under illumination at room temperature", *Journal of Nanomedicine and Nanotechnology,* c. 4, sayı. 3, 1000167, 2013.

[18] S. Altındal Yerişkin, H. Uslu, T. Tunç ve Ş. Altındal, "Illumination effect on admittance measurements of

Polyvinyl Alcohol (Co, Zn-Doped)/n-Si Schottky Barrier Diodes in wide frequency and applied bias voltage range", *International Advances in Applied Physics and Materials Science Congress & Exhibition*, 2011, c.1400, ss. 541-545.

[19] H.C Card ve E.H. Rhoderick, "Studies of tunnel MOS diodes I. Interface effects in silicon Schottky diodes", *Journal of Physics D: Applied Physics*, c. 4, ss.1589-1601, 1971.

[20] R.T. Tung, "Comment on Numerical study of electrical transport in homogeneous Schottky diodes" *Journal of Applied Physics*, c. 88, sayı 3, ss. 7366-7368, 2000.

KATKILI/KATKISIZ METAL OKSİT (MO) NANOPARTİKÜL (NP) ÜRETİMİ VE BAZI FİZİKSEL ÖZELLİKLERİNİN İNCELENMESİ[1]

Fatih ERGÜL[2]

Sinan TEMEL[2]

Fatma Özge GÖKMEN[3]

1. GİRİŞ

Nanoteknolojinin hızlı gelişimi, metal bazlı nanoparçacıkların (MNP'ler) muazzam üretimine yol açmaktadır. MNP'lerin toprak ve su iyileştirme, tarımsal amaçlar, kozmetikler, boyalar ve farmasötikler vb. gibi geniş uygulamaları vardır (Tiwari vd., 2022). Metal oksit NP'lerin yüzeyindeki atom sayısı, NP'lerin boyutunun küçülmesiyle artar, bu da reaktivitelerini artırır ve topaklanma eğilimiyle sonuçlanır. NP'lerin daha küçük boyutuyla ilişkili dezavantajlar, uygun fiziksel, kimyasal veya biyolojik yöntemler kullanılarak yüzeylerinin modifiye edilmesiyle aşılabilir (Kumar vd., 2022). Yüzey modifikasyonu, kontrollü aglomerasyon ile stabilitelerini artırmak için NP'lerin yüzeyine inorganik bir kabuk veya organik moleküllerin kaplanmasıyla yapılabilir (Kumar vd., 2022).

---

[1] Bu çalışma Fatih ERGÜL'ün Yüksek Lisans tezi kapsamında hazırlanmıştır.

[2] Yüksek Lisans Öğrencisi, Bilecik Şeyh Edebali Üniversitesi Lisansüstü Eğitim Enstitüsü Fizik Anabilim dalı, 3703475@ogrenci.bilecik.edu.tr ORCID: 0009-0004-7816-9065.

[2] Doç. Dr., Bilecik Şeyh Edebali Üniversitesi, Fen Fakültesi Fizik Bölümü, sinan.temel@bilecik.edu.tr, ORCID: 0000-0002-0889-9490.

[3] Doç. Dr., Bilecik Şeyh Edebali Üniversitesi, Meslek Yüksekokulu, Üretimde Kalite Kontrol Bölümü, fatmaozge.gokmen@bilecik.edu.tr, ORCID: 0000-0002-5548-8790.

Günümüzde, başta metal ve metal oksit nanopartiküller olmak üzere çeşitli nanopartiküller ve bunların olası uygulamaları üzerine araştırmalar ortaya çıkmaktadır. Bu uygulamalardan biri, potansiyometrik sensörlerin analitik parametrelerini iyileştirmek için bunların kullanılmasıdır (Pietrzak vd., 2022). Günümüzde nanopartikül elde etmek için birçok yöntem geliştirilmiştir. Bunlar kolayca fiziksel (fiziksel buhar fazı biriktirme, mekanik öğütme, püskürtme, lazer ablasyon), kimyasal (kimyasal buhar fazı biriktirme, kimyasal indirgeme, elektrosentez) ve biyolojik (bakteri, mantar, yosun kullanılarak biyolojik sentez) yöntemler olarak ayrılabilir. Bununla birlikte, başlangıç malzemesinin türüne bağlı olarak, hepsi iki yöntem grubuna atanabilir: aşağıdan yukarıya yaklaşım (küçük boyutlardaki basit maddelerden nanoyapılar oluşturmak) ve yukarıdan aşağıya yaklaşım (esas olarak mekanik yöntemler aracılığıyla ayrışma sonucunda makroskopik malzemeden nanoparçacıklar elde etmek) (Khan vd., 2019). Çeşitli morfolojilere sahip MO nanopartikülleri (NP'ler) enerji depolama makineleri, sensörler, kaplamalar, yağlama, elektrokimya, çevresel iyileştirme ve benzeri geniş kapsamlı uygulamalar için araştırılmıştır (Qumar vd., 2022). Adsorban özelliklerini kullanım bu alanların en önemlilerinden biridir. Moleküllerin boyutu kütleden nano ölçeğe düştüğünde, yüzey-hacim oranında üstel bir artışa neden olur. Boyutu en aza indirerek ve etkileşim için organik moleküllerin yüzeylerine aktif kenarlar ekleyerek, yüzey enerjisi veya adsorban kompozitler geliştirilir. Bununla birlikte, nanomateryaller, organik kirleticileri sudan uzaklaştırmak için daha hacimli muadillerine kıyasla önemli adsorpsiyon kabiliyeti sergiler. Ayrıca, MO NP'ler, tek başlarına veya nanokompozitler halinde, organik kirleticileri hızlı ve verimli bir şekilde gidermek için tasarlanmış son derece seçici adsor- bentler olarak yakın zamanda benzersiz bir perspektif ortaya koymuştur (Qumar vd., 2022). Ayrıca, geçiş metal oksitleri (TMO'lar) ve nanokompozitleri organik kirleticileri yok etmek için güçlü bir fotokatalitik reaksiyona sahiptir. Doğru yapı,

kristal ve yüzey aidiyetine sahip MO bazlı nanokompozitler, büyük bant aralığı enerjili (Eg) yarı iletkenler olarak işlev görür ve organik kirleticilerin bozunması için toksik olmama ve suda kararlılık gibi olumlu nitelikler sergiler.

Metal-oksit nanopartikül üretim yöntemleri arasında; birlikte çökeltme işlemi, hidrotermal işlem, mikrodalga ışınlama, darbeli lazer biriktirme, katı hal reaksiyon işlemi, sol-jel işlemi, sprey piroliz tekniği, çözelti yakma, mekanik bilyalı öğütme ve mikrodalga destekli solvo-termal yöntemler yer almaktadır (Saleem vd., 2022). Sol-jel işleminin homojen olmayan bileşimde ince manyetik nanopartiküller sağlar, ayrıca daha iyi bir kontrol oranını olanaklı hale getirir. Basit bir hazırlama tekniğidir. Diğer bir yöntem ise, kimyasal birlikte çökeltme işlemidir. Nanopartiküllerin (NP'ler) büyük ölçekli hazırlanması, basit laboratuvar ekipmanı ve kendi içinde basitlik, düşük maliyet, dopant konsantrasyonunun etkili ve kolay ayarlanması gibi olağanüstü avantajları nedeniyle daha fazla dikkat çekmiştir (Saleem vd., 2022). Nano boyutta metal oksitlerin üretimi arasında, çökeltme yönteminin basit, ekonomik ve ölçeklenebilir olduğu, çünkü NP'lerin boyutu, şekli, kristal yapısı ve yüzey reaktivitesi gibi içsel özelliklerinin sentez sırasında kontrol edilebildiği bildirilmektedir (Tran vd., 2018). Metal oksitler, özellikle geçiş metalleri, manyetik, optik, elektrik, katalizör ve çeşitli alanlarda potansiyel uygulama gibi çekici özelliklere sahiptir (Vara ve Dave, 2019). Metal oksitlerin on yıllardır katalizör olarak sıklıkla çalışıldığı da incelenen literatürlerde görülmüştür (Chatudvedi ve Dave, 2012). Oksit nanoparçacıkları, yanma hızlarını artıran herhangi bir yığılma göstermezler. Mikro ve nanometre boyutundaki partikül (metal) oksitler arasındaki karşılaştırmada, katalizörün katalitik verimliliği nanometre aralığında keskin bir şekilde artmıştır (Vara ve Dave, 2019). Nano boyuttaki metal oksitlerin bir diğer yaygın kullanım alanı da adsorpsiyon prosesleri içerisinde geliştirilmiş yeni nesil adsorban

olarak kullanımıdır (Kumar vd., 2022). Atık sulardan ağır metal iyonlarını uzaklaştırmak için kullanılan membran filtrasyonu, kimyasal çökeltme, adsorpsiyon, iyon değişimi ve birlikte çökeltme gibi çeşitli yöntemler arasında adsorpsiyon en etkili ve güvenli yöntem olarak kabul edilmektedir (Maheshwari ve Gupta, 2016). Geleneksel olarak, tarımsal yan ürünler, meyve atıkları, aktif karbon ve modifiye biyopolimerler gibi birçok doğal ve ticari adsorban, suyun iyileştirilmesi için adsorban olarak kullanılmıştır. Ancak, yüksek üretim maliyetleri, düşük adsorpsiyon kapasiteleri ve adsorpsiyon sonrası bertaraflarına ilişkin sınırlı bilgi nedeniyle kullanımları sınırlıdır (Hua vd., 2012). Bu nedenle, atık sulardan ağır metal iyonlarını uzaklaştırmak için alternatif bir adsorban malzeme bulmaya ihtiyaç vardır. Son yıllarda, nanopartiküllerin küçük boyutları, geniş yüzey alanları ve daha yüksek aktif bölgeleri nedeniyle mükemmel bir adsorban olduğu bildirilmiştir (Pradhan vd., 2017).

Bu çalışmanın özgün değeri, geçiş metalleri kullanılarak elde edilen metal oksit nanopartiküllerinin aynı akademik çıktı da bir arada kıyaslanabilir olmasıdır. Literatüre bakıldığında, katkılamaların benzer yöntemler ile reaksiyon edilip kendi içinde karşılaştırılması mevcuttur. Bu çalışmada aynı metodlar farklı metal öncülerine uygulanıp katkılamanın gerçekleştirilmesi amaçlanmıştır.

2. MATERYAL YÖNTEM

2.1.Metal Oksitler

Metaller, doğada genellikle kararsız yapıdadır. Bu nedenle metaller, kararlı yapıya sahip olmak amacıyla oksijen ile tepkimeye girerek metal oksit bileşenine dönüşürler. Metal oksitler, günümüzde en yaygın kullanılan bileşiklerin başında gelmektedir ve birçok farklı kimyasal ve atomik bileşimlere

sahiptir. Metal oksitlerin fiziksel yapısı çoğunlukla, katı, kristalin ve metalik özellik göstermektedir. Fakat genellikle oda sıcaklığında metal oksitler kırılgan yapıda bulunmaktadır. Metal oksitler birçok farklı özelliği yapısında bulundurmaktadır. Bunlara; yüksek ve kimyasal mukavemet, faz geçirgenliği, yüksek kararlılık, farklı kristal bileşimler, yüksek kaynama ve erime, optik ve elektriksel özellikler örnek verilebilir.

Metal oksitler fiziksel yapılarına göre, metal ya da geçiş metali içeren bileşikler olarak iki grupta incelenirler. Yapısında metal bulunan metal oksitlere, Silisyum Dioksit (SiO_2) ve Magnezyum Oksit (MgO) örnek olarak verilebilir. Yapısında geçiş metali bulunan metal oksitlere ise Titanyum Monoksit (TiO), Krom Dioksit (CrO_2), Kobalt Oksit (CoO), Bakır Oksit (CuO) ve Nikel Oksit (NiO) bileşikleri örnek verilebilir.

Metal oksitler diğer bileşenlerden farklı olarak yüksek işlevsellik özelliği gösterdiği bilinmektedir (Pal, 2020). Bu nedenle başta malzeme biliminde, kimya alanında ve aynı zamanda endüstriyel uygulamalarda sıklıkla kullanılmaktadır.

2.2.Metal Oksit (MO) Nanopartiküller

Nanopartiküller, fiziksel ve kimyasal yapılarına dikkat edilerek 100 nanometre boyutundan küçük olacak şekilde sentezlenmektedir (Wang vd., 2009). Nanopartiküllerin sahip olduğu avantajlı yapısından dolayı günümüzde, endüstriyel ve bilimsel çalışmalarda sıklıkla kullanılmaktadır. Nanopartiküllerin kuantum etkisi ve yüzey alanı partiküllerin boyutuna bağlı olarak değişmekte ve elektrik, optik ve manyetik alanları partiküllerin boyutu küçüldükçe daha reaktif hal kazanmaktadır (Warheit, 2018). Günümüzde birçok farklı alanda nanopartiküller kullanılsa da metal ve metal oksit temelli nanopartiküller sıklıkla kullanılan partiküllerin başında gelmektedir.

Metal oksit nanopartiküller, metal elementlerinin oksijen ile birleşerek oluşturduğu bileşiklerin nanometre ölçeğindeki

parçacıklarını ifade etmektedir. Metal oksit nanopartiküller, genellikle 1 ila 100 nanometre arasında bir boyuta sahiptir. Metal oksit nanopartiküller, geniş bir uygulama yelpazesine sahip olup, çeşitli endüstriyel, tıbbi ve bilimsel alanlarda kullanılmaktadır (Vance vd., 2015).

2.2.1. CoO Nanopartiküller

Metal oksit nanopartikülleri nano boyutta, kimyasal kararlılığa ve geniş yüzey alanına sahip olmaları sebebiyle araştırmacılar tarafından sıklıkla tercih edilmektedir (Sethuraman vd., 2018). Geçiş metali oksitleri içerisinde Kobalt Oksitler (CoO) p tipi bir yarı iletken olup, 1.2 eV ile 1.7 eV arasında bir bant aralığına sahiptir (Kaur vd., 2006). Tablo 1' de fizikokimyasal özellikleri sunulmuştur. Şekil 1'de ise CoO nanopartiküllerin atomik gösterimini temsil etmektedir. Kırmızı toplar oksijeni (O) elementini kahverengi toplar ise kobalt (Co) elementini ifade etmektedir.

CoO nanopartiküller, nano yapılarının kolaylıkla optimize edilmesi, mükemmel katalitik özellik göstermesi ve maliyetinin düşük olması nedeniyle günümüzde sıklıkla kullanılmaktadır. Aynı zamanda yüksek elektriksel ve termal iletkenliğe sahip olmasından dolayı metal oksit nanopartikülleri içerisinde en yayın kullanılan nano malzemedir (Tuncsoy, 2020).

CoO nanopartikülleri sahip olduğu yüksek hacim ve yüzey oranları nedeniyle birçok farklı alanlarda kullanılmaktadır. Örnek olarak manyetik depolama işlemleri (Wang vd., 2007), lityum iyonu temelli elektrotlar (Xu vd., 2011) ve güneş pilleri (Sahay vd., 2012) verilebilir.

Şekil 1. Coo Nanopartikülün Atomik Gösterimi

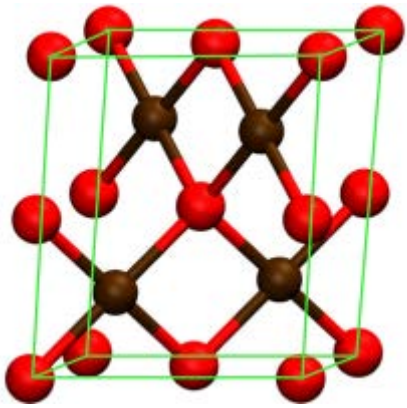

Kaynak: (Gattinoni ve Michaelides, 2015).

Tablo 1. Coo Nanopartikülün Fizikokimyasal Özellikleri

IUPAC Numarası	Cobalt(II)Oxide
Molar Kütle	79.545 g mol^{-1}
Erime Noktası	1326°C
Kaynama Noktası	2000°C
Yoğunluk	6.31 g cm^{-3}

Kaynak: (Yoon vd., 2000)

2.2.2. NiO Nanopartiküller

Demir grubu metallerinden olan nikel (Ni), sahip olduğu manyetik yapısından dolayı oldukça geniş kullanım alanına sahiptir. Günümüzde NiO nano partiküller; nano çubuk, nano tüp ve nano prizma gibi çeşitli formlarda üretilmektedir (Ati vd., 2013). NiO nanopartikülleri genellikle iletken, katalitik ve manyetik malzemelerin üretiminde ve geliştirilmesinde kullanılmaktadır. Örneğin; katı oksit yakıt pillerinde ve optik sensörlerde anot katmanı olarak kullanılmaktadır (Karaduman, 2017). Şekil 2'de NiO nanopartiküllerin atomik gösterimi bulunmaktadır. Tablo 2'de ise NiO nanopartiküllerin fizikokimyasal özellikleri özet şeklinde sunulmuştur.

NiO nanopartiküllerin birçok farklı üretim yöntemi bulunmaktadır. Bunlar; mekanik öğütme, piroliz, hidrazin yöntemi, nikel tuzların kimyasal redüksiyonu, sonokimyasal yöntem ve son olarak elektrokimyasal çöktürme yöntemleridir (Alonso vd., 2011).

Şekil 2. Nio Nanopartiküllerin Atomik Gösterimi

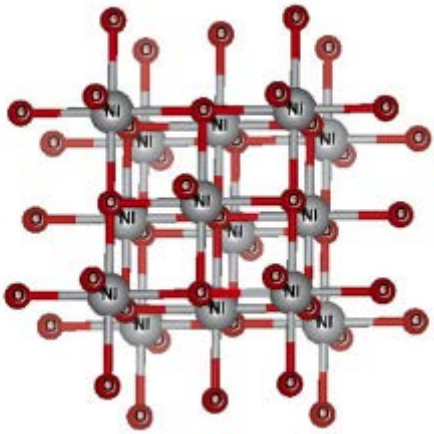

Kaynak: (Goel vd., 2020).

Tablo 2. Nio Nanopartikülün Fizikokimyasal Özellikleri

IUPAC Numarası	Nickel(2+); Oxygen(2-)
Molar Kütle	74.69 g mol^{-1}
Erime Noktası	1955°C
Kaynama Noktası	--
Yoğunluk	6.67 g cm^{-3}

Kaynak: (Goel vd., 2020).

3. DENEYSEL ÇALIŞMALAR

3.1.CoO Nanopartikül Sentezi

Kobalt (II) nitrat [Co(NO3)2·6H2O)]'ın sodyum hidroksit (NaOH) ile sulu ortamda indirgenerek çökeltilmesiyle CoO nanopartikülleri, elde edilmiştir. Bu amaçla, 0.5 M kobalt (II)

nitrat çözeltisi hazırlanmıştır. Bu çözelti 6 saat 70°C'de karıştırılmıştır. Karışıma 0.1 M NaOH çözeltisi damla damla ilave edilerek çökelti elde edilmiştir. Elde edilen çökelti Whatman süzgeç kağıdı ile süzülmüştür. Süzüntü su ve etanol ile 3 kez yıkanmıştır. Yıkamadan sonra süzüntü etüvde 24 saat 60°C'de kurutulmuştur. Kurutulan örnek 300°C'de 5 saat süreyle hava ortamında tavlanarak CoO nanopartiküller elde edilmiştir.

3.2.NiO Nanopartikül Sentezi

Nikel (II) nitrat [Ni(NO3)2·6H2O)]'ın sodyum hidroksit (NaOH) ile sulu ortamda indirgenerek çökeltilmesiyle NiO nanopartikülleri, elde edilmiştir. Bu amaçla, 0.5 M nikel (II) nitrat çözeltisi hazırlanmıştır. Bu çözelti 6 saat 70°C'de karıştırılmıştır. Karışıma 0.1 M NaOH çözeltisi damla damla ilave edilerek çökelti elde edilmiştir. Elde edilen çökelti Whatman süzgeç kağıdı ile süzülmüştür. Süzüntü su ve etanol ile 3 kez yıkanmıştır. Yıkamadan sonra süzüntü etüvde 24 saat 60°C'de kurutulmuştur. Kurutulan örnek 300°C'de 5 saat süreyle hava ortamında tavlanarak NiO nanopartiküller elde edilmiştir.

3.3.Karakterizasyon

Yapısal ve yüzeysel analizler sırasıyla XRD ve FESEM cihazları ile yapılmıştır. XRD cihazı Panalytical Empreyan ve FESEM cihazı SUPRA 40VP, Carl Zeiss model/marka ile gerçekleştirilmiştir. XRD analizi 2-theta açısı 10 - 90° aralığında gerçekleştirilmiştir. FESEM görüntüleri 15kV ve 15kX büyültmelerde elde edilmiştir. EDX analizi ile elementel dağılım sonuçları elde edilmiştir.

3.4.Analiz sonuçları

Şekil 3'de CoO nanopartikül üretimi için kullandığımız Kobalt (II) nitrat [Co(NO3)2·6H2O)] tuzunun XRD spektrumu verilmiştir. Şekil 4'de ise sentez sonucu elde ettiğimiz CoO nanopartiküllerin XRD spektrumu görünmektedir.

Şekil 3. Kobalt (II) Nitrat Tuzunun XRD Spektrumu

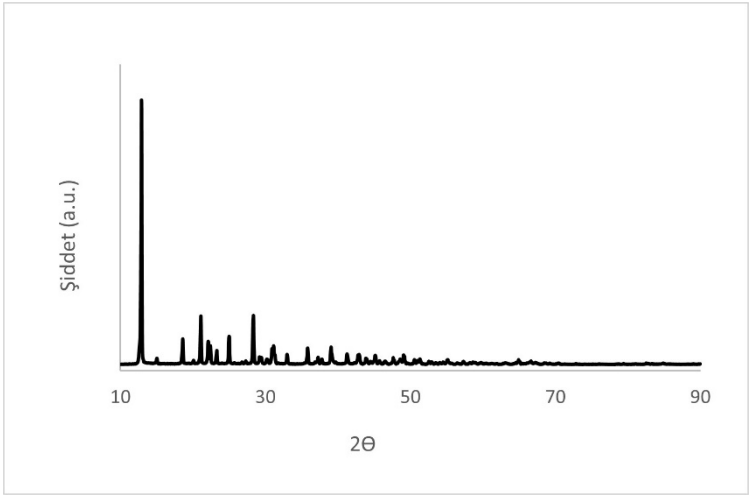

Şekil 4. Sentez Sonucu Elde Edilen CoO Nanopartiküllerin XRD Spektrumu

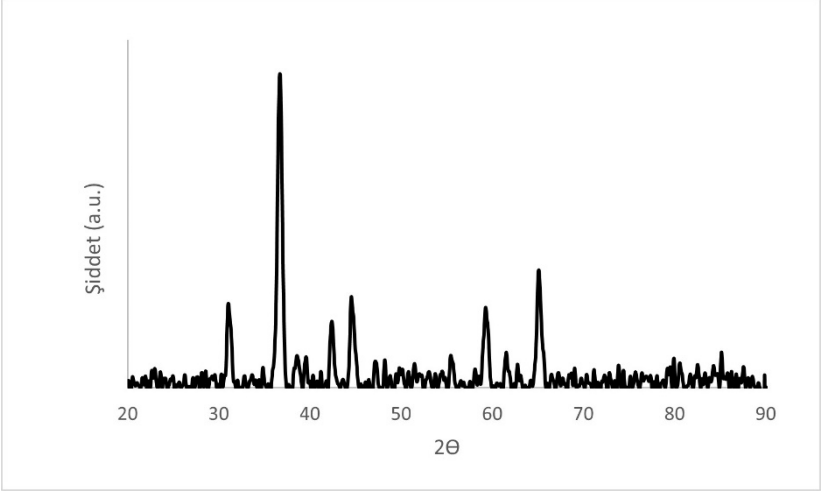

Spektrumlardan görüldüğü gibi Kobalt (II) nitrat [Co(NO3)2·6H2O)] tuzu kullanılarak başlatılan sentez sonucunda saf CoO nanopartikül elde edilmiştir. CoO nanopartiküllerin spektrumunda yer alan tüm piklerin, 98-017-

3830 referans numaralı kübik yapıda CoO yapısının ASTM kartı ile birebir uyumlu olduğu görülmüştür.

Şekil 5'de NiO nanopartikül üretimi için kullandığımız Nikel (II) nitrat [Ni(NO3)2·6H2O)] tuzunun XRD spektrumu verilmiştir. Şekil 6'da ise sentez sonucu elde ettiğimiz NiO nanopartiküllerin XRD spektrumu görünmektedir.

Spektrumlardan görüldüğü gibi Nikel (II) nitrat [Ni(NO3)2·6H2O)] tuzu kullanılarak başlatılan sentez sonucunda saf NiO nanopartikül elde edilmiştir. NiO nanopartiküllerin spektrumunda yer alan tüm piklerin, 98-005-3930 referans numaralı kübik yapıda NiO yapısının ASTM kartı ile birebir uyumlu olduğu görülmüştür.

Şekil 5. Nikel (II) Nitrat Tuzunun XRD Spektrumu

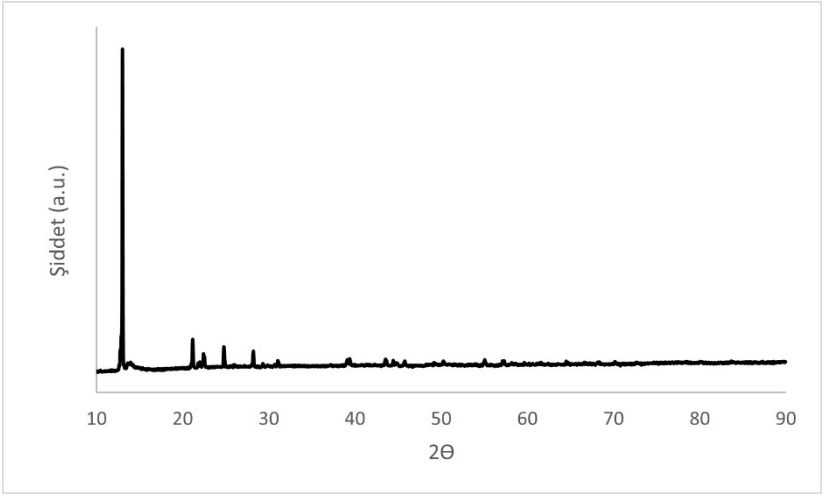

Şekil 6. Sentez Sonucu Elde Edilen NiO Nanopartiküllerin XRD Spektrumu

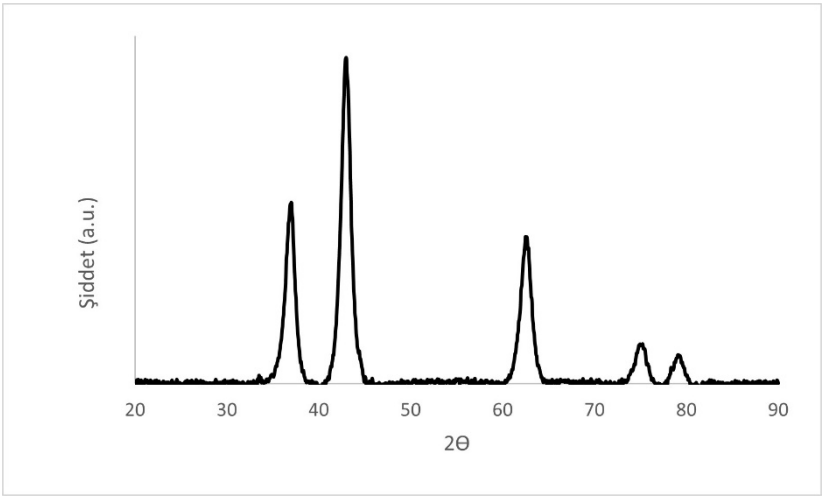

Tablo 3'de ise XRD spektrumundan alınan veriler ile Debye-Scherrer Formülü kullanılarak hesaplanan ortalama tane boyutu değerleri verilmiştir. Tablodan görüleceği gibi hem CoO hem de NiO partiküller nano yapıdadır. Yapısal analiz sonuçlarına göre CoO ve NiO nanopartikül üretiminin başarılı bir şekilde gerçekleştirildiği görülmektedir.

Tablo 3. Ortalama Tane Boyutu Değerleri

Yapı	Ortalama Tane Boyutu (nm)
CoO	43,6
NiO	16,1

Şekil 7'de CoO'e ait FESEM görüntüsü verilmiştir. Tablo 4'de ise CoO EDX sonuçları listelenmiştir.

Şekil 7. CoO'e Ait FESEM Görüntüsü

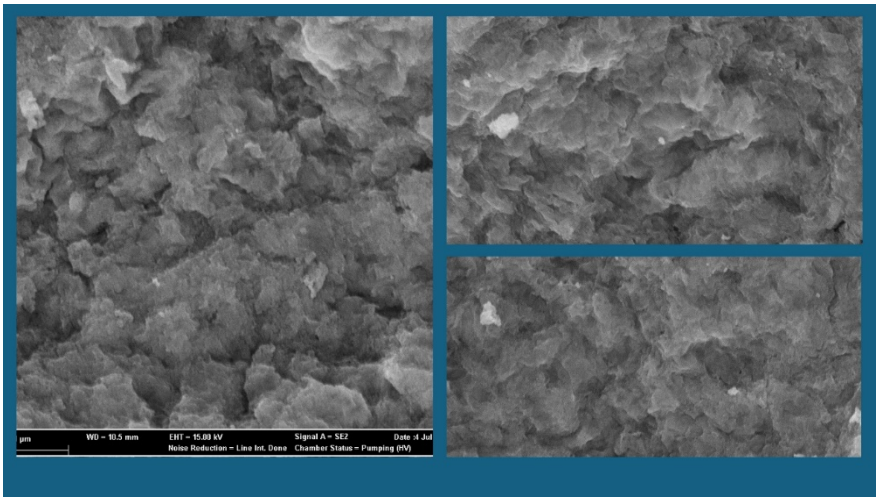

Tablo 4. CoO EDX Sonuçları

Element	Atomik Yüzde (at.%)
Co	57,07
O	42.93

FESEM görüntülerinden görüleceği gibi elde edilen CoO homojen yapıdadır. EDX sonuçları da yapıda herhangi bir safsızlık olmadığını teyit etmiştir. Görüntülerden hesaplanan ortalama tane boyutu değerleri de XRD sonuçlarını desteklemektedir. Sentez sonucu saf ve homojen yapıda CoO nanopartikül yapısı elde edilmiştir.

Şekil 8'de NiO'e ait FESEM görüntüsü verilmiştir. Tablo 5'de ise NiO EDX sonuçları listelenmiştir.

Şekil 8. NiO'e Ait FESEM Görüntüsü

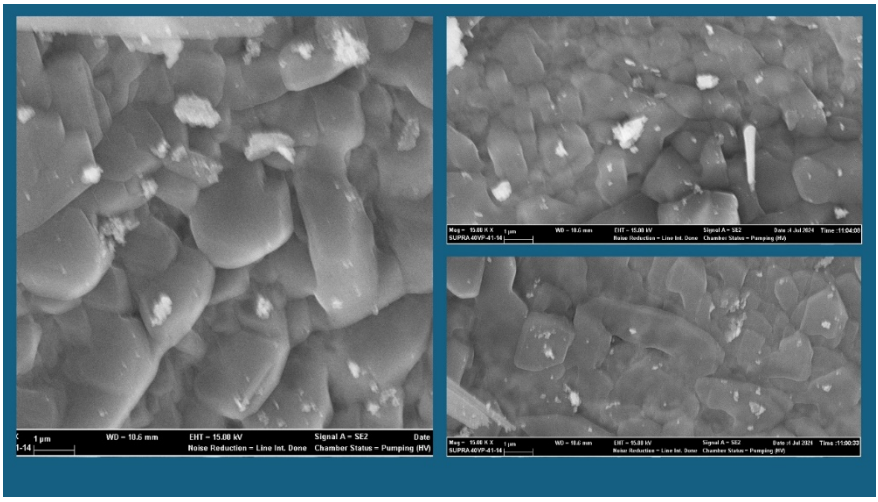

Tablo 5. NiO EDX Sonuçları

Element	Atomik Yüzde (at.%)
Ni	51,81
O	48.19

FESEM görüntülerinden görüleceği gibi elde edilen NiO homojen yapıdadır. EDX sonuçları da yapıda herhangi bir safsızlık olmadığını teyit etmiştir. Görüntülerden hesaplanan ortalama tane boyutu değerleri de XRD sonuçlarını desteklemektedir. Sentez sonucu saf ve homojen yapıda NiO nanopartikül yapısı elde edilmiştir.

4. SONUÇ

Yapılan çalışma kapsamında CoO ve NiO nanopartiküller sulu ortamda indirgenerek çökeltilme yöntemiyle sentezlenmiştir. Elde edilen nanopartiküllerin yapısal ve yüzeysel özellikleri incelenmiş ve başarılı bir sentez olup olmadığı araştırılmıştır. Kobalt (II) nitrat [Co(NO3)2·6H2O)] tuzu kullanılarak başlatılan sentez sonucunda saf CoO nanopartikül ve Nikel (II) nitrat

[Ni(NO3)2·6H2O)] tuzu kullanılarak başlatılan sentez sonucunda saf NiO nanopartikül elde edilmiştir. CoO nanopartiküllerin spektrumunda yer alan tüm piklerin, kübik yapıda CoO yapısının, NiO nanopartiküllerin spektrumunda yer alan tüm piklerin, kübik yapıda NiO yapısının ASTM kartı ile birebir uyumlu olduğu görülmektedir. XRD spektrumundan alınan veriler ile Debye-Scherrer Formülü kullanılarak hesaplanan ortalama tane boyutu değerleri hem CoO hem de NiO partiküller nano yapıda olduğunu göstermiştir. Yapısal analiz sonuçlarına göre CoO ve NiO nanopartikül üretiminin başarılı bir şekilde gerçekleştirildiği görülmektedir. FESEM görüntülerinden görüleceği gibi elde edilen CoO ve NiO homojen yapıdadır. EDX sonuçları da bu yapılarda herhangi bir safsızlık olmadığını teyit etmiştir. Görüntülerden hesaplanan ortalama tane boyutu değerleri de XRD sonuçlarını desteklemektedir. Yüzeysel analiz bulguları da sentez sonucu saf ve homojen yapıda CoO ve NiO nanopartikül yapılarının elde edildiğini göstermiştir.

Çalışmanın devamında, elde edilen nanopartiküllerin ikili ve Grafen katkılanarak üçlü sentezleri de gerçekleştirilecektir. Bu ikili ve üçlü yapılar yüksek sıcaklıklarda (1200°C) ısıl işleme tabi tutularak numunelerin Zeta Potansiyeli, XPS ve TEM analizleri de yapılarak uygulama alanları incelenecektir.

KAYNAKÇA

Alonso, F., Riente, P., & Yus, M. (2011). Nickel nanoparticles in hydrogentransfer reductions: Characterization and nature of the catalyst. Applied Catalyst, 379-391.

Ati, A. A., Othaman, Z., & Samavati, A. (2013). Influence of cobalt on structural and magnetic properties of nickel ferrite nanoparticles. Journal of Molecular Structure, 177-182.

Chaturvedi S., Dave P.N., (2012). Nano-metal oxide: potential catalyst on thermal decomposition of ammonium perchlorate, J. Exp. Nanosci. 7, 205–231.

Gattinoni, C., & Michaelides, A. (2015). Atomistic details of oxide surfaces and surface oxidation: the example of copper and its oxides. Surface Science Reports, 70(3), 424-447.

Goel, R., Jha, R., & Ravikant, C. (2020). Investigating the structural, electrochemical, and optical properties of p-type spherical nickel oxide (NiO) nanoparticles. Journal of Physics and Chemistry of Solids, 144, 109488.

Hua, M., Zhang, S., Pan, B., Zhang, W., Lv, L., Zhang, Q., (2012). Heavy metal removal from water/wastewater by nanosized metal oxides: a review. J. Hazard Mater. 211 (212), 317–331.

Karaduman, E. (2017). Kobalt-nikel nanopartiküllerinin ve karbon içerikli nanokompozitlerinin sentezi ve incelenmesi. Yıldız Teknik Üniversitesi, Fen Bilimleri Enstitüsü, Biyomühendislik Bölümü, Yüksek Lisans Tezi.

Kaur, M., Muthe, K. P., Despande, S. K., Choudhury, S., Singh, J. B., Verma, N., ... & Yakhmi, J. V. (2006). Growth and branching of CuO nanowires by thermal oxidation of copper. Journal of Crystal Growth, 289(2), 670-675.

Khan I., Saeed K., Khan I., (2022). Nanoparticles: properties, applications and toxicities, Arab, J. Chem. 12, 908–931.

Kumar A.K, Yeshwanth M., Kumar K.B., Panwar J., Gupta S., (2022). Functionalized Cu-based metal oxide nanoparticles with enhanced Cd+2 adsorption capacity and their ecotoxicity assessment by molecular docking, Journal of Environmental Management 307, 114523.

Maheshwari, U., Gupta, S., (2016). Performance evaluation of activated neem bark for the removal of Zn(II) and Cu(II) along with other metal ions from aqueous solution and synthetic pulp & paper industry effluent using fixed-bed reactor. Process Saf. Environ. Protect. 102, 547–557.

Manjunath, A., Irfan, M., Anushree, K. P., Vinutha, K. M., & Yamunarani, N. (2016). Synthesis and Characterization of CuO Nanoparticles and CuO Doped PVA Nanocomposites. Advances in Materials Physics and Chemistry, 06(10).

Pal, D. (2020). Synthesis of metal oxide nanoparticles-A general overview. Indian J, (59), 1513–1528.

Pietrzak K., Krstulovic N., Blazeka D., Car J., Malinowski S., Wardak C., (2022). Metal oxide nanoparticles as solid contact in ion-selective electrodes sensitive to potassium ions, Talanta 243, 123335.

Pradhan, S.K., Panwar, J., Gupta, S., (2017). Enhanced heavy metal removal using silveryttrium oxide nanocomposites as novel adsorbent system. J. Environ. Chem. Eng. 5, 5801–5814.

Qumar U., Hassan J.Z., Bhatti R. A., Raza A., Nazir G., Nabgan W., Ikram M., (2022). Journal of Materials Science & Technology 131, 122–166.

Sahay, R., Sundaramurthy, J., Kumar, P. S., Thavasi, V., Mhaisalkar, S. G., & Ramakrishna, S. (2012). Synthesis and characterization of CuO nanofibers, and investigation for its suitability as blocking layer in ZnO NPs based dye sensitized solar cell and as photocatalyst in organic dye degradation. Journal of Solid State Chemistry, 186, 261-267.

Saleem S., Jameel M.H., Akhtar N., Nazir N., Ali A., Zaman A., Rehman A., Butt S., Sultana F., Mushtaq M., Zeng J.H., Amami M., Althubeiti K., (2022). Modification in structural, optical, morphological, and electrical properties of zinc oxide (ZnO) nanoparticles (NPs) by metal (Ni, Co) dopants for electronic device applications, Arabian Journal of Chemistry, 15, 103518.

Sethuraman, R. G., Venkatachalam, T., & Kirupha, S. D. (2018). Fabrication and characterization of Zn doped CuO nanofiber using newly designed nanofiber generator for the photodegradation of methylene blue from textile effluent. Materials Science-Poland, 36(3), 520-529.

Tiwari E., Singh N., Khandelwal N., Ganie Z.A., Choudhary A., Monikh F.A., Darbha G.K., (2022). Impact of nanoplastic debris on the stability and transport of metal oxide nanoparticles: role of varying soil solution chemistry, Chemosphere 308, 136091.

Tran, Q.H., Nguyen, V.Q., Le, A.-T., (2018). Corrigendum: silver nanoparticles: synthesis, properties, toxicology, applications and perspectives. Adv. Nat. Sci. Nanosci. Nanotechnol. 9, 049501.

Tuncsoy, B. (2020). Bakır oksit nanopartiküllerinin Galleria mellonella larvaları üzerine immün ve metabolik etkileri. Karaelmas Fen ve Mühendislik Dergisi, 10(1), 53-60.

Vance, M. E., Kuiken, T., Vejerano, E. P., McGinnis, S. P., Hochella Jr, M. F., Rejeski, D., & Hull, M. S. (2015). Nanotechnology in the real world: Redeveloping the nanomaterial consumer products inventory. Beilstein Journal of Nanotechnology, 6(1), 1769-1780.

Vara J.A., Dave P.N., (2019). Metal oxide nanoparticles as catalyst for thermal behavior of AN based composite solid propellant, Chemical Physics Letters 730, 600–607.

Wang, S. Q., Zhang, J. Y., & Chen, C. H. (2007). Dandelion-like hollow microspheres of CuO as anode material for lithium-ion batteries. Scripta Materialia, 57(4), 337-340.

Wang, F., Gao, F., Lan, M., Yuan, H., Huang, Y., & Liu, J. (2009). Oxidative stress contributes to silica nanoparticle-induced cytotoxicity in human embryonic kidney cells. Toxicology In Vitro, 23(5), 808-815.

Warheit, D. B. (2018). Hazard and risk assessment strategies for nanoparticle exposures: how far have we come in the past 10 years? F1000Research, 7.

Xu, M., Wang, F., Zhao, M., Yang, S., Sun, Z., & Song, X. (2011). Synthesis of copper oxide nanostructures via a composite-Hydroxide-mediated approach: Morphology control and the electrochemical performances as anode material for lithium ion batteries. Physica E: Low-dimensional Systems and Nanostructures, 44(2), 506-510.

Yoon, K. H., Choi, W. J., & Kang, D. H. (2000). Photoelectrochemical properties of copper oxide thin films coated on an n-Si substrate. Thin solid films, 372(1-2), 250-256.

TİP 2 DİYABET TEDAVİSİNDE KULLANILAN MİGLİTOL MOLEKÜLÜ VE OLASI RADİKALLERİNİN DOCKİNG ÇALIŞMASI

Halil Uğur TAŞDEMİR[1]

1. GİRİŞ

Miglitol molekülü kompleks karbonhidratların glikozo dönüşümünü engelleyen Tip-2 diyabet tedavisinde kullanılan bir ilaç etken maddesidir. Miglitol molekülü önemli bir ilaç etken maddesi olduğundan dolayı literatürde miglitol molekülü ile ilgili çalışmalar mevcuttur. Örneğin Pistara ve arkadaşları Miglitol molekülünün moleküler docking çalışmasını gerçekleştirmişlerdir (Pistarà, ve diğerleri, 2011). Miglitol molekülünün Tip-2 diyabet hastalığını tedavi edici etkisi Scott ve Spencer tarafından çalışılmıştır (Scott & Spencer, 2000). Katsura ve arkadaşları Miglitol molekülünün farmakolojik özelliklerini fareler üzerinde araştırmışlardır (Katsura, Yukiharu, & Toji, 2001). Paulraj ve Muthu da miglitol molekülünün spektroskopik özelliklerini ve moleküler yapısını teorik ve deneysel metotlarla açığa çıkarmışlardır (Paulraj & Muthu, 2013).

Son yıllarda ortaya çıkan virüs ve bakteriler yeni ilaçlara gereksinimi arttırmıştır. Kovid-19 salgını bu durumun en iyi örneğidir. Yeni ilaçlar geliştirilirken kullanılan mevcut ilaçlar göz önüne alınır. Genelde bir ilacın geliştirilmesine teorik hesaplamalar basamağı ile başlanır. Öncelikle etken maddenin moleküler yapısı teorik hesaplama metotları kullanılarak ortaya çıkarılır çünkü moleküler yapı ele alınan molekülün elektriksel ve

[1] Dr., Necmettin Erbakan Üniversitesi Ahmet Keleşoğlu Eğitim Fakültesi, Fizik Eğitimi, halilugurtasdemir@gmail.com, ORCID: 0000-0002-6205-0092.

spektroskopik özellikleri ile yakından ilişkilidir. Bu anlamda birinci adım olarak ele alınan molekülün moleküler yapısının doğru bir şekilde açığa çıkarılması gerekir. Moleküler yapıları tahmin edebilmek için Yoğunluk Fonksiyonelleri Metodu (DFT) teorik hesaplamalarda yaygın bir şekilde kullanılır (Hehre, Radom, Schleyer, & Pople, 1986; Foresman & Frisch, 1996; Ruud, ve diğerleri, 1994; Osmialowski, Kolehmainen, & Gawinecki, 2001; Dega-Szafran, Katrusiak, & Szafran, 2006; Tasdemir, Türkkan, Sayin, & Ozmen, 2016). Ortaya çıkarılan moleküler yapı kullanılarak molekülün elektriksel ve spektroskopik özellikleri teorik hesaplama yöntemleri ile hesaplanır. DFT metodu bir molekülün elektriksel ve spektroskopik özelliklerini hesaplamada oldukça başarılı bir yöntemdir (Castro & Figueroa-Villar, 2002; Sayin, Dereli, Turkkan, Yuksel, & Birey, 2011; Kolandaivel & Senthilkumar, 2001). Moleküler yapısı ortaya çıkarılan molekülün ne derece etkili olabileceğini araştırmak için protein ve DNA gibi makromoleküller ile etkileşimi incelenir. Bu inceleme simülasyon ve hesaplama yöntemleri ile gerçekleştirilir. Bu incelemeye göre sentezlenecek ilaç etken maddesinin ne şekilde olması gerektiğine karar verilir.

Bu çalışmada ilaç etken maddesi olan miglitol molekülünün ve miglitol molekülünde oluşabilecek iki radikal türünün moleküler docking çalışması teorik hesaplama metotları ve simülasyon programları kullanılarak gerçekleştirilmiştir.

2. MİGLİTOL MOLEKÜLÜNÜN MOLEKÜLER YAPISI

Miglitol molekülünün moleküler yapısı literatüre uygun bir şekilde Gaussian 03 programı kullanılarak B3LYP/6-311++G (d, p) metot baz seti kombinasyonu yardımıyla açığa çıkarılmıştır (Paulraj & Muthu, 2013) (Frisch, ve diğerleri, 2003) (Becke,

1993) (Stephens, Devlin, Chabalowski, & Frisch, 1994) (Lee, Yang, & Parr, 1994). Hesaplama sonucunda elde edilen kararlı yapı Şekil 1 de verilmiştir. Miglitol molekülünün moleküler yapısı incelendiğinde molekül içi hidrojen bağı oluştuğu söylenebilir. Buna göre H22 ve O12 atomları arasındaki mesafe 2.03 A^0 olarak hesaplanmıştır. Bu mesafe hidrojen bağı mertebesindedir. Molekül içi hidrojen bağı moleküldeki kararlılığı etkileyen faktörlerden biridir (Espinosa, Molins, & Lecomte, 1998) .

Şekil 1. Miglitol Molekülünün Hesaplama Sonucunda Elde Edilen Moleküler Yapısı

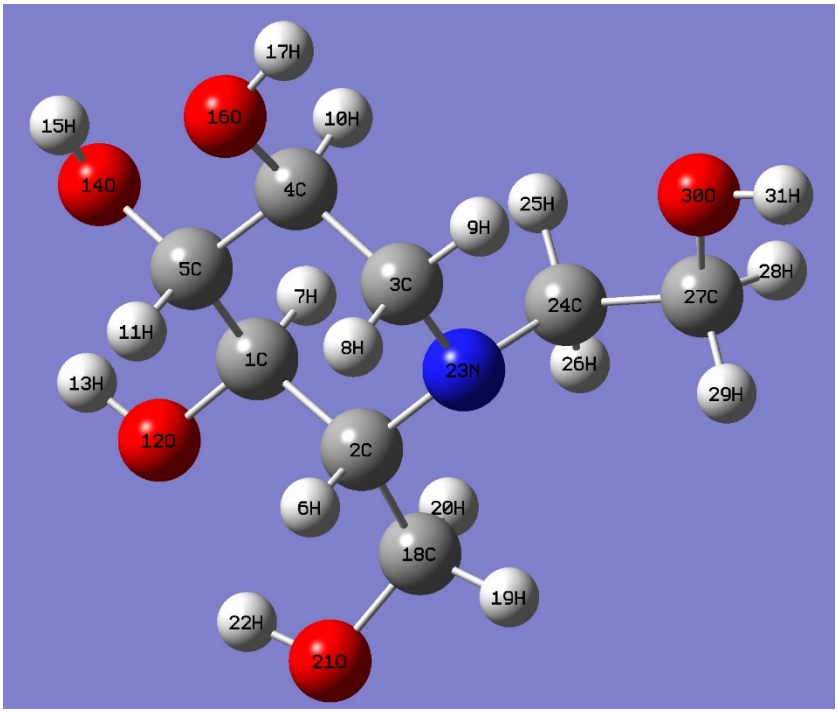

Eşleşmemiş elektrona sahip atom molekül veya iyonlara radikal denir. Karbon merkezli radikaller alkil tipi, oksijen merkezli radikaller ise alkoksi tipi radikaller olarak isimlendirilirler (Bernhard, Close, Hüttermann, & Zehner, 1977;

Tasdemir, Sayin, Türkkan, & Ozmen, 2016). Miglitol molekülünde alkoksi tipi radikal oluşturmak için H22 numaralı Hidrojen atomu koparılmıştır. Oluşan radikalin en kararlı hali bulabilmek için DFT/ B3LYP/6-311++ G (d, p) metot baz seti kombinasyonu kullanılmıştır. Alkoksi tipi radikal Rad1 olarak adlandırılmıştır. Oluşan alkoksi tipi radikalin hesaplama sonucunda bulunan en kararlı yapısı Şekil 2 gösterilmiştir.

Şekil 2. Alkoksi (Rad1) ve Alkil (Rad2) Tipi Radikallerin Hesaplama Sonucunda Bulunan En Kararlı Yapıları

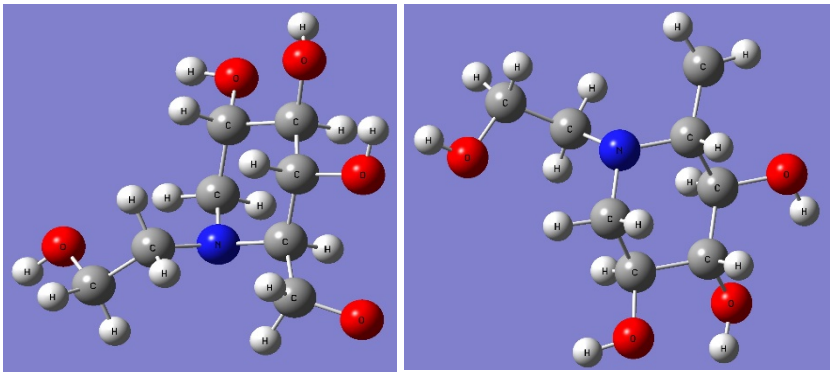

Rad1 Rad2

Alkil tipi radikal oluşturmak için miglitol molekülünde O21 ve H22 (OH) atomları koparılmıştır. Oluşan bu radikal Rad2 olarak adlandırılmıştır. Rad2 radikalinin en kararlı yapısını bulmak için de Rad1 radikalinin hesaplamasında kullanılan metot ve baz seti kombinasyonu kullanılmıştır. Hesaplama sonucunda Rad2 radikalinin bulunan en kararlı yapısı Şekil 2 de gösterilmiştir. Miglitol molekülünün N-terminal Human Maltase-Glucoamylase (PDB ID: 3L4W) enzimi ile docking çalışması literatürde mevcuttur (Sim, ve diğerleri, 2010). Teorik hesaplama sonucunda bulunan miglitol molekülünün ve olası iki radikalinin 3L4W enzimi ile docking çalışmaları Auto Dock Vina programı kullanılarak gerçekleştirilmiştir (Trott & Olson, 2010). Bu docking çalışmalarının simülasyonları Şekil 3'te verilmiştir.

Şekil 3. Miglitol Molekülünün ve Olası İki Radikalinin 3L4W Enzimi ile Moleküler Docking Hesaplamalarının Gösterimi

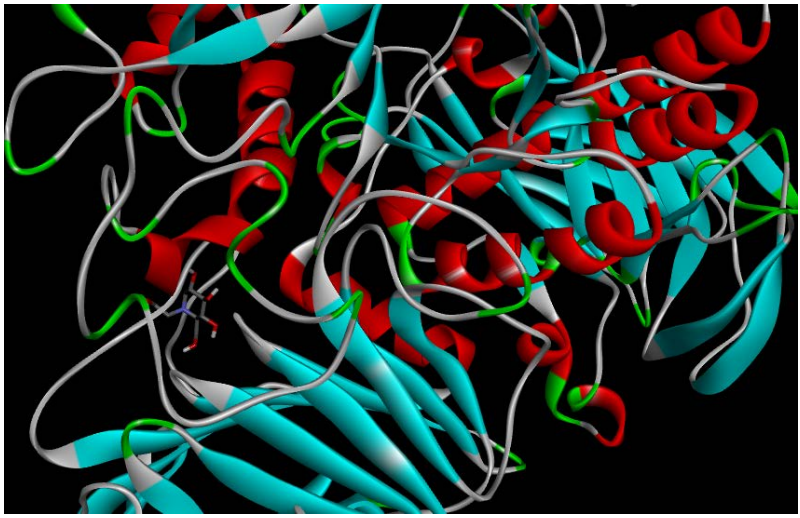

Miglitol

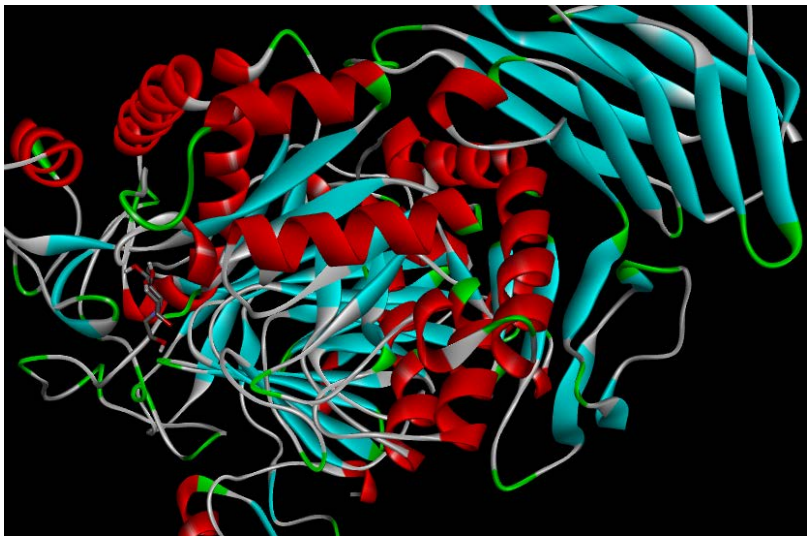

Rad1

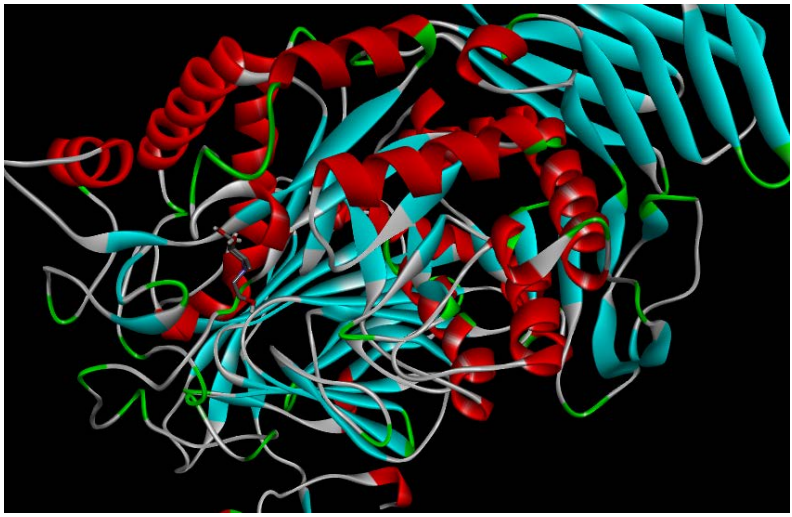

Rad2

Miglitol molekülünün ve olası iki radikalinin 3L4W enzimindeki aminoasitler ile etkileşimi Şekil 4'te verilmiştir

Şekil 4. Miglitol ve İki Olası Radikalinin (Rad1 ve Rad2) 3L4W Enzimindeki Aminoasitler ile Etkileşiminin 2 Boyutlu Gösterimi

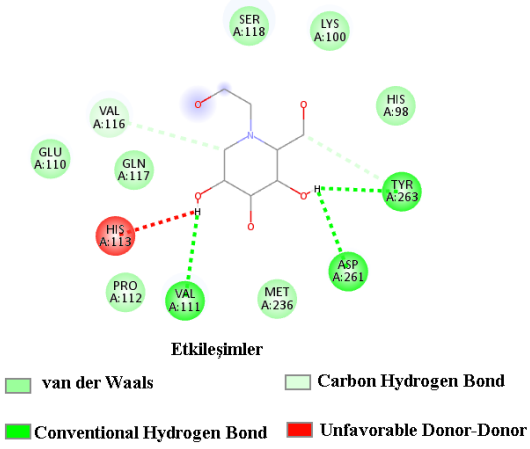

Miglitol

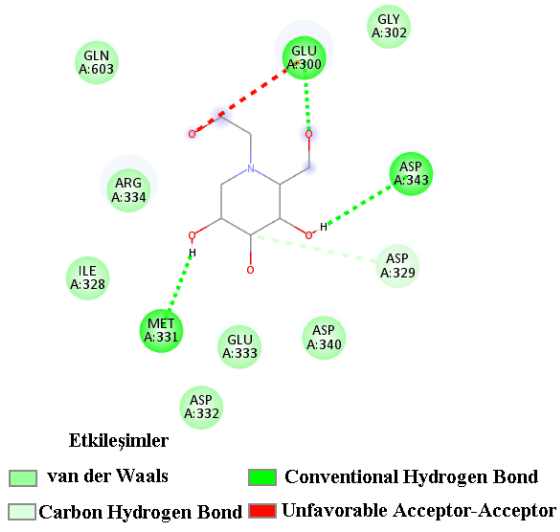

Rad1

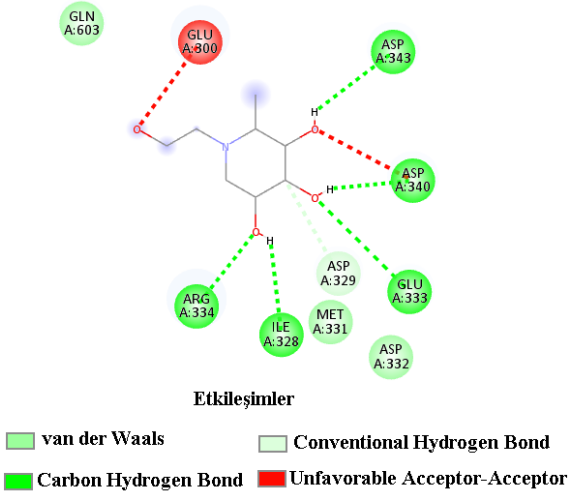

Rad2

Moleküler docking hesaplamalarının sonuçlarına göre miglitol molekülü için hesaplanan bağlanma afinite enerjisi-5.2 kcal/mol, Rad1 için hesaplanan bağlanma afinite enerjisinin değeri de -5.2 kcal/mol iken Rad2 için hesaplanan bağlanma

afinite enerji değeri -5.3 kcal/ mol dür. Miglitol molekülü ve olası iki radikalleri için bağlanma afinite enerjileri arasında çok büyük fark bulunmamakla birlikte bağlandıkları kısımdaki etkileştikleri aminoasit gruplarının farklılık gösterdiği Şekil 4 ten görülmektedir. Afinite bağlanma enerjisi en düşük olan Rad2 radikalidir. Buna göre Rad2 radikalinin 3L4W enzimi ile etkileşimi miglitol molekülüne göre daha iyidir. Miglitol molekülünün, Rad1 ve Rad2 radikallerinin etkileştiği aminoasit gruplarının farklılık göstermesi biyolojik aktivitenin farklı olabileceği anlamına gelebilmektedir.

3. SONUÇ

Kovid-19 pandemisi yeni ilaçlara gereksinimi bütün dünyaya göstermiştir. Yeni ilaçlar mevcut ilaçların dönüştürülmesi ile de gerçekleştirilir. Bu anlamda ilaç tasarımı ve yeni ilaç sentezi günümüzde ve gelecekte önemli bir konu olmaya devam edecektir. Yapılan bu çalışmada Tip-2 diyabet tedavisinde kullanılan miglitol molekülünün ve radikallerinin biyolojik aktivitelerinin birbirleriyle kıyaslanması teorik olarak gerçekleştirilmiştir. Kıyaslama sonuçlarına göre miglitol molekülünden elde edilecek radikaller daha farklı etkileşimler gerçekleştirmektedir. Buna göre ileride miglitol molekülünden elde edilecek radikallerin etkileri deneysel olarak incelenebilir. Böylece şu anda ilaç etken maddesi olarak kullanılan miglitol molekülünden daha aktif yeni ilaç etken maddelerinin sentezlenmesi için gelecekte yapılacak çalışmalara ışık tutulmuştur.

KAYNAKÇA

Becke, A. (1993). Density-functional thermochemistry. III. The role of exact Exchange. *J. Chem. Phys, 98*, 5648-5652.

Bernhard, W., Close, D., Hüttermann, J., & Zehner, H. (1977). The alkoxy radical, RCH2Ȯ , as a free radical product in x-irradiated single crystals of nucleosides and nucleotides. *J. Chem. Phys, 67*, 1211-1219.

Castro, A. T., & Figueroa-Villar, J. D. (2002). Molecular Structure, ConformationalAnalysis and Charge Distribution ofPralidoxime: Ab Initio and DFT Studies. *International Journal of Quantum Chemistry, 89*, 135-146.

Dega-Szafran, Z., Katrusiak, A., & Szafran, M. (2006). X-ray, NMR and DFT studies of the complex of 1,4-dimethylpiperazine mono-betaine with p-hydroxybenzoic acid. *Journal of Molecular Structure, 785*(1-3), 160-166.

Espinosa, E., Molins, E., & Lecomte, C. (1998). Hydrogen bond strengths revealed by topological analyses of experimentally observed electron densities. *Chemical Physics Letters,, 285*, 170-173.

Foresman, J. B., & Frisch, A. (1996). *Exploring Chemistry with Electronic Structure Methods: A Guide to Using Gaussian.* Pittsburgh: Gaussian.

Frisch, M. J., Trucks, G. W., Schlegel, H. B., Scuseria, G. E., Robb, M. A., Cheeseman, J. R., . . . Pople, J. (2003). *Gaussian 03, Revision C.02.* Wallingford CT: Gaussian, Inc.

Hehre, W. J., Radom, L., Schleyer, P. R., & Pople, J. A. (1986). *Ab Initio Molecular Orbital Theory.* New York: John Wiley & Sons.

Katsura, T., Yukiharu, N., & Toji, M. (2001). Pharmacological Properties of Miglitol, an α Glucosidase Inhibitor, in Rats. . *Japanese Pharmacology & Therapeutics, 29*(6), 623-633.

Kolandaivel, P., & Senthilkumar, K. (2001). Ab initio and DFT studies on structure and stability of aliphatic aldoxime molecules. *Journal of Molecular Structure: THEOCHEM, 535*(1-3), 61-70.

Lee, C., Yang, W., & Parr, R. (1994). Development of the Colle-Salvetti correlationenergy formula into a functional of the electron density. *Phys. Rev. B, 37*, 785-789.

Osmialowski, O., Kolehmainen, E., & Gawinecki, R. (2001). GIAO/DFT calculated chemical shifts of tautomeric species. 2-Phenacylpyridines and (Z)-2-(2-hydroxy-2-phenylvinyl)pyridines. *Magnetic Resonance in Chemistry, 39*(6), 334-340.

Paulraj, E. I., & Muthu, S. (2013). Spectroscopic studies (FTIR, FT-Raman and UV), potential energy surface scan, normal coordinate analysis and NBO analysis of (2R,3R,4R,5S)-1-(2-hydroxyethyl)-2-(hydroxymethyl) piperidine-3,4,5-triol by DFT methods. *Spectrochimica Acta Part A: Molecular and Biomolecular Spectroscopy, 108*, 38-49.

Pistarà, V., Rescifina, A., Punzo, F., Greco, G., Barbera, V., & Corsaro, A. (2011). Design, Synthesis, Molecular Docking and Crystal Structure Prediction of New Azasugar Analogues of α-Glucosidase. *Eur. J. Org.*, 7278-7287.

Ruud, K., Helgaker, T., Kobayashi, R., Jorgensen, P., Bak, K. L., & Jensen, H. J. (1994). Multiconfigurational self-consistent field calculations of nuclear shieldings using

London atomic orbitals. *Journal of Chemical Physics, 100*(11), 8178-8185.

Sayin, U., Dereli, O., Turkkan, E., Yuksel, H., & Birey, M. (2011). EPR study of gamma irradiated 2,5-di-tert-butyl-hydroquinone single crystals. *Radiat.Phys. Chem, 80*, 38-43.

Scott, L. J., & Spencer, C. M. (2000). Miglitol A Review of its Therapeutic Potential in Type 2 Diabetes Mellitus. *Drugs, 59*(3), 521-549.

Sim, L., Jayakanthan, K., Mohan, S., Nasi, R., Johnston, B., Pinto, B., & Rose, D. (2010). New Glucosidase Inhibitors from an Ayurvedic Herbal Treatment for Type 2 Diabetes: Structures and Inhibition of Human Intestinal Maltase-Glucoamylase with Compounds from Salacia reticulata. *Biochemistry, 49*, 443-451.

Stephens, P., Devlin, F., Chabalowski, C., & Frisch, M. (1994). Ab initio calculation of vibrational absorption and circular dichroism spectra using density functional force fields. *J. Phys. Chem, 98*, 11623-11627.

Tasdemir, H. U., Türkkan, E., Sayin, U., & Ozmen, A. (2016). EPR study of gamma-irradiated 2-Bromo-4' -methoxyacetophenone single crystal. *Radiation Effect & Defect in Solids, 171*, 214-222.

Tasdemir, H., Sayin, U., Türkkan, E., & Ozmen, A. (2016). EPR investigation of gamma irradiated single crystal guaifenesin: A combined experimental and computational study. *Radiation Physics and Chemistry, 121*, 61-68.

Trott, O., & Olson, A. (2010). AutoDock Vina: improving the speed and accuracy of docking with a new scoring function, efficient optimization and multithreading . *Journal of Computational Chemistry, 31(2,* 455-461.

MAVİ IŞIK FİLTRELİ GÖZLÜK KULLANIMININ GÖZ SAĞLIĞI ÜZERİNDE OLUŞTURDUĞU OLUMLU VE OLUMSUZ ETKİLERİN BELİRLENMESİ[1]

Aslı TURAL[2]

Dilara DURUKAN[2]

Ezgi KIRAN[2]

Ezgi Nur ÖZCAN[3]

Özge ERDEM[4]

1. GİRİŞ

Gelişen teknoloji ile bireylerin ekran karşısında geçirdiği zaman da artmaktadır. Bu durum göz sağlığını olumsuz etkilemekle birlikte göz sağlığı üzerine yapılan çalışmaları da arttırmıştır. Dünya genelinde yaşanan pandemi nedeniyle okullarda eğitim-öğretimin çevrimiçi yöntemlerle yapılması bireylerin küçük yaşlarda televizyon, bilgisayar, tablet, dizüstü bilgisayar ve telefon ekranları karşısında mavi ışığa maruz

[1] Bu çalışma, TÜBİTAK 2209-A Üniversite Öğrencileri Araştırma Projeleri Destek Programı tarafından 2023 yılı/1.dönem 1919B012307786 proje numarası ile desteklenen "Mavi Işık Filtreli Gözlük Kullanımının Göz Sağlığı Üzerinde Oluşturduğu Olumlu ve Olumsuz Etkilerin Belirlenmesi" isimli projeden üretilmiştir.

[2] Optisyen, Bayburt Üniversitesi, Sağlık Hizmetleri MYO, Tıbbi Hizmetler ve Teknikler Bölümü, turalasli1@gmail.com, Durukandilara12@gmail.com, EzgEf2121@hotmail.com

[3] Öğrenci, Bayburt Üniversitesi, Sağlık Hizmetleri MYO, Tıbbi Hizmetler ve Teknikler Bölümü, Ezginurozcan90@gmail.com

[4] Doç. Dr., Bayburt Üniversitesi, Sağlık Hizmetleri MYO, Tıbbi Hizmetler ve Teknikler Bölümü, ozgeerdem@bayburt.edu.tr, ORCID: 0000-0003-4542-941X.

kalmalarına ve bunun sonucu olarak da göz yorgunluğunun artmasına neden olmuştur. Son yıllarda giderek artan uykusuzluk, göz yorgunluğu, gözlerde kuruluk gibi göz rahatsızlıkları bireyleri mavi ışık filtreli gözlük kullanımına sevk etmektedir.

Mavi ışık, görünür ışık bölgesinin 380-500 nm arasında yer alan bir elektromanyetik dalgadır. Güneşten yayılan mavi-mor ışık göz bebeklerinin ışığa tepkimesi ve odaklama yapabilmesi bakımından yararlı iken, bilgisayar, telefon, tablet gibi LED kaynaklı teknolojiler kullanan cihazlardan yayılan yüksek enerjili mavi ışık ise zararlıdır. Mavi ışık filtreli gözlük kullanımı ile mavi ışığın göz üzerinde oluşturabileceği zararlardan özel filtreler yardımıyla belirli bir ölçüde korunmak mümkündür.

Bu bölümde, mavi ışık filtreli gözlük kullanımının bireylerin göz sağlığı üzerinde oluşturduğu olumlu ve olumsuz etkileri belirlemek üzere Optisyenlik alanında yapılan bir araştırma çalışmasından bahsedilmiştir.

2. ÇALIŞMA İÇERİĞİ

2.1. Materyal/Metot

Çalışmada, mavi ışık filtreli gözlük kullanımının bireylerin göz sağlığı üzerinde oluşturduğu olumlu ve olumsuz etkileri belirlemek için, Trabzon ilinde yer alan 20 optik müessese ve Trabzon'daki devlet hastanelerinde çalışan 8 göz doktoru ile izinleri dahilinde ses kaydı altında yarı-yapılandırılmış mülakat ile mavi ışık filtreli gözlük kullanan 18-45 yaş arası 50 katılımcı ile gönüllülük esasına uygun olarak yüz yüze anket yapılmıştır. Ankette toplam 12 adet demografik ve açık uçlu sorular kullanılmıştır. Optik müesseseler ve göz doktorları ile yapılan mülakatlarda ise sırasıyla 13 ve 9 adet açık uçlu soru kullanılmıştır. Mülakat sırasında duruma göre yeni sorular da

sorulmuştur. Çalışma konusunun belirlenmesi ve anket sorularının hazırlanması için literatürdeki kaynaklardan (Türkoğlu, Türkoğlu, & Kaya, 2013; Ateş & Aytaç 2019) yararlanılmıştır.

Araştırmada sorulara verilen cevaplar SPSS 22.0 ile frekans dağılımları incelenerek değerlendirilmiştir. Böylece, mavi ışık filtreli gözlük kullanımından doğan olumlu ve olumsuz etkiler ile mavi ışık filtreli gözlüğün hangi rahatsızlıklara karşı kullanıldığı/önerildiği hakkında bilgi edinilmiştir.

2.2. Bulgular

2.2.1. Anket Formlarından Elde Edilen Veriler

Anket çalışmasına katılan 50 katılımcının tamamı mavi ışık filtreli gözlük kullanmaktadır. Bu katılımcıların cinsiyet dağılımı Tablo 1'de verilmiştir. Buna göre, ankete katılanların cinsiyet dağılımının orantılı olduğu görülür.

Tablo 1. Anket Çalışmasına Katılanların Cinsiyet Dağılımı

	Sayı	Yüzde	Geçerli Yüzde	Kümülatif Yüzde
Erkek	26	52,0	52,0	52,0
Kadın	24	48,0	48,0	100,0
Toplam	50	100,0	100,0	

Anket çalışmasına katılanların yaş dağılımı Tablo 2'de verilmiştir. Buna göre, ankete katılanların belirtilen yaş aralıklarına göre yaklaşık olarak homojen bir yaş dağılımına sahip olduğu görülür.

Tablo 2. Anket Çalışmasına Katılanların Yaş Dağılımı

	Erkek	Kadın	Toplam Sayı	Yüzde	Geçerli Yüzde	Kümülatif Yüzde
18-25	7	10	17	34,0	34,0	34,0
26-35	9	5	14	28,0	28,0	62,0
36-45	10	9	19	38,0	38,0	100,0
Toplam	26	24	50	100,0	100,0	

Anket çalışmasına katılanların hangi tür gözlük kullandığı Tablo 3'de verilmiştir. Buna göre katılımcıların % 48'inin miyop ve % 40'ının ise miyop astigmat göz rahatsızlığına sahip olduğu tespit edilmiştir.

Tablo 3. Anket Çalışmasına Katılanların Göz Rahatsızlıkları

	Erkek	Kadın	Toplam Sayı	Yüzde	Geçerli Yüzde	Kümülatif Yüzde
Miyop	17	7	24	48,0	48,0	48,0
Hipermetrop	2	2	4	8,0	8,0	56,0
Astigmat	0	1	1	2,0	2,0	58,0
Miyop ve Astigmat	6	14	20	40,0	40,0	98,0
Hipermetrop ve Astigmat	1	0	1	2,0	2,0	100,0
Toplam	26	24	50	100,0	100,0	

Anket çalışmasına katılanların gözlük kullanım süreleri Tablo 4'de verilmiştir. Buna göre, katılımcıların % 54 gibi büyük bir kısmının 10 yıl ve üzeri zamandır gözlük kullandıkları belirlenmiştir.

Tablo 4. Anket Çalışmasına Katılanların Gözlük Kullanım Süreleri

	Erkek	Kadın	Toplam Sayı	Yüzde	Geçerli Yüzde	Kümülatif Yüzde
1 yıl-3 yıl	2	5	7	14,0	14,0	14,0
3 yıl-6 yıl	7	2	9	18,0	18,0	32,0
6 yıl-9 yıl	3	4	7	14,0	14,0	46,0
10 yıl ve üzeri	14	13	27	54,0	54,0	100,0
Toplam	26	24	50	100,0	100,0	

Anket çalışmasına katılanların mavi ışık yayan ekran karşısında geçirdikleri bir günlük ortalama süre Tablo 5'de verilmiştir. Buna göre, katılımcıların % 42'si 5-8 saat kadar bir zamanı ekran karşısında geçirmektedir.

Tablo 5. Anket Çalışmasına Katılanların Mavi Işık Yayan Ekran Karşısında Geçirdikleri Bir Günlük Ortalama Süre

	Erkek	Kadın	Toplam Sayı	Yüzde	Geçerli Yüzde	Kümülatif Yüzde
2 saat-5 saat	6	4	10	20,0	20,0	20,0
5 saat-8 saat	11	10	21	42,0	42,0	62,0
8 saat-10 saat	4	5	9	18,0	18,0	80,0
10 saat üzeri	5	5	10	20,0	20,0	100,0
Toplam	26	24	50	100,0	100,0	

Anket çalışmasına katılanların mavi ışık filtreli gözlük kullanımını tercih etme nedenleri Tablo 6'da verilmiştir. Buna göre, katılımcıların % 40'ı ekran karşısında fazla vakit geçirdikleri için, % 16'sı meslek gereği ve % 14'ü ekran karşısında göz yorgunluğunu önlediği için mavi ışık filtreli gözlük kullandıklarını belirtmişlerdir.

Tablo 6. Anket Çalışmasına Katılanların Mavi Işık Filtreli Gözlük Kullanımını Tercih Etme Nedenleri

	Erkek	Kadın	Toplam Sayı	Yüzde	Geçerli Yüzde	Kümülatif Yüzde
Doktor tavsiyesi	1	1	2	4,0	4,0	4,0
Optisyen tavsiyesi	1	0	1	2,0	2,0	6,0
Meslek gereği	4	4	8	16,0	16,0	22,0
Ekran karşısında fazla vakit geçirme	11	9	20	40,0	40,0	62,0
Ekran karşısında zararlı ışınlarda gözü koruması	1	5	6	12,0	12,0	74,0
Ekran karşısında göz yaşarmasını önlemesi	1	1	2	4,0	4,0	78,0
Ekran karşısında göz yorgunluğunu önlemesi	5	2	7	14,0	14,0	92,0
Ekran karşısında göz/baş ağrısını önlemesi	1	1	2	4,0	4,0	96,0
Ekran karşısında göz kuruluğunu önlemesi	1	0	1	2,0	2,0	98,0
Ekran karşısında parlamayı önlemesi	0	1	1	2,0	2,0	100,0
Toplam	26	24	50	100,0	100,0	

Anket çalışmasına katılanlar, mavi ışık filtreli gözlük kullanımının göz sağlıkları üzerindeki olumlu etkilerini Tablo 7'deki gibi tanımlamışlardır. Buna göre, katılımcıların % 42'si mavi ışık filtreli gözlüğün göz yorgunluğunu azalttığını, % 16'sı ekran karşısında parlamayı önlediği ve zararlı ışınlardan koruduğunu ve yine % 16'sı göz-baş ağrısını ve göz sulanmasını önlediğini belirtmişlerdir. Katılımcılar mavi ışık filtreli gözlüğün olumsuz etkilerinin sorulduğu soruya genel olarak, "Olumsuz etkisi yoktur/rastlamadım/bilmiyorum" diye cevaplar vermişlerdir. 3 kadın ve 4 erkek katılımcı mavi ışık filtreli gözlüğün olumsuz etkilerinden bahsederken "Etrafı sarımtırak göstermesi/soluk göstermesi", 1 kadın katılımcı "Baş ağrısı yapması", 2 erkek katılımcı "Nadiren göz kuruluğu yapması" diye belirtmişlerdir.

Tablo 7. Anket Çalışmasına Katılanların Belirttiği Mavi Işık Filtreli Gözlük Kullanımının Göz Sağlığı Üzerindeki Olumlu Etkileri

	Erkek	Kadın	Toplam Sayı	Yüzde	Geçerli Yüzde	Kümülatif Yüzde
Gözleri dinlendirici etkisi	2	2	4	8,0	8,0	8,0
Göz kuruluğunu azaltması	2	1	3	6,0	6,0	14,0
Göz yorgunluğunu azaltması	12	9	21	42,0	42,0	56,0
Ekran karşısında parlamayı önleme ve zararlı ışınlarda koruma	2	6	8	16,0	16,0	72,0
Göz-baş ağrısını ve göz sulanmasını önlemesi	3	5	8	16,0	16,0	88,0
Göz sağlığına faydalı olup yaşam kalitesini arttırması	3	1	4	8,0	8,0	96,0
Normal gözlükten farkı yok	1	0	1	2,0	2,0	98,0
Cevapsız	1	0	1	2,0	2,0	100,0
Toplam	26	24	50	100,0	100,0	

2.2.2. Optisyenlik Müesseseleri ile Yapılan Yarı-Yapılandırılmış Mülakatlardan Elde Edilen Veriler

20 adet optisyenlik müessesesi ile yapılan yarı-yapılandırılmış mülakat sonucu özellikle üç soruya verilen cevapların frekans dağılımları çeşitlilik göstermiştir. Bu sorular aşağıda verilmiştir:

Soru A: *Hangi şikâyetlerle gelen müşterilere mavi ışık filtreli cam önerilir?*

Soru B: *Mavi ışık filtreli cam kullanımının avantaj ve dezavantajları nelerdir?*

Soru C: *Mavi ışık filtreli cam kullanan müşterilerinizden aldığınız olumlu-olumsuz geri dönütler nelerdir?*

A sorusuna verilen cevaplar Tablo 8'de verilmiştir. Tablo 8'den görüleceği üzere, optik müesseseler müşterilerin % 25'inin göz yorgunluğu ve baş ağrısı nedeniyle, diğer % 25'inin mavi ışığa hassasiyet nedeniyle, % 20'sinin doktorun yazdığı reçete nedeniyle, diğer % 20'sinin ise göz yorgunluğu ve göz sulanması/yanması/kızarması nedeniyle mavi ışık filtreli gözlük kullanmak istediklerini belirtmişlerdir.

Tablo 8. A Sorusuna Verilen Cevaplar

	Sayı	Yüzde	Geçerli Yüzde	Kümülatif Yüzde
Göz yorgunluğu ve baş ağrısı	5	25,0	25,0	25,0
Doktorun yazdığı reçeteye göre	4	20,0	20,0	45,0
Mavi ışığa hassasiyet	5	25,0	25,0	70,0
Göz yorgunluğu ve göz sulanması/yanması/kızarması	4	20,0	20,0	90,0
Göz kuruluğu	1	5,0	5,0	95,0
Göz yorgunluğu	1	5,0	5,0	100,0
Toplam	20	100,0	100,0	

B sorusuna verilen cevaplar (avantaj-dezavantaj) Tablo 9 ve Tablo 10'da verilmiştir. Tablo 9'dan optik müesseselere göre, mavi ışık filtreli gözlüğün avantajları arasında öne çıkan

cevapların; göz yorgunluğu ve baş ağrısını önlemesi (% 40) ile ekran ışığını süzüp zararlı ışınlardan koruması (% 30) olduğu görülür. Tablo 10'da, optisyenlik müesseselerine göre mavi ışık filtreli gözlüğün dezavantajları arasında sarımtırak bir görüntü oluşturması (% 30) öne çıkmaktadır. Bunun yanında, % 60 oranında dezavantajı yoktur cevabı verilmiştir.

Tablo 9. B Sorusuna Verilen Cevaplar (Avantajlar)

	Sayı	Yüzde	Geçerli Yüzde	Kümülatif Yüzde
Göz yorgunluğu ve baş ağrısını önlemesi	8	40,0	40,0	40,0
Ekran ışığını süzüp zararlı ışınlardan koruması	6	30,0	30,0	70,0
Gözü dinlendirmesi	1	5,0	5,0	75,0
Ekran karşısında kalma süresini arttırması	1	5,0	5,0	80,0
Gözlerde kızarma ve sulanmayı önlemesi, uyku düzensizliğini gidermesi	1	5,0	5,0	85,0
Yaşam kalitesini arttırır.	3	15,0	15,0	100,0
Toplam	20	100,0	100,0	

Tablo 10. B Sorusuna Verilen Cevaplar (Dezavantajlar)

	Sayı	Yüzde	Geçerli Yüzde	Kümülatif Yüzde
Sarımtırak bir görüntü oluşması	6	30,0	30,0	30,0
Göz kuruluğu yapması	1	5,0	5,0	35,0
Fotoğraf çekiminde parlaması	1	5,0	5,0	40,0
Dezavantajı yok	12	60,0	60,0	100,0
Toplam	20	100,0	100,0	

C sorusuna verilen cevaplar (olumlu-olumsuz geri dönüt) ise Tablo 11 ve Tablo 12'de verilmiştir. Tablo 11'den müşterilerin optik müesseselere verdikleri olumlu geri dönütler arasında % 50 oranında yaşam kalitesini yükseltmesi, genellikle olumlu dönütler alınması ve yeniden tercih edilmesi cevabı öne çıkmıştır. % 20 oranında ise göz yorgunluğu ve baş ağrısını gidermesi cevabı verilmiştir. Olumsuz geri dönütler arasında ise,

% 30 oranında sarımtırak bir görüntü oluşturması cevabı verilmiştir. Bunun yanında, optik müesseseler % 55 oranında olumsuz geri dönüt almadıklarını belirtmişlerdir.

Tablo 11. C Sorusuna Verilen Cevaplar (Olumlu Geri Dönüt)

	Sayı	Yüzde	Geçerli Yüzde	Kümülatif Yüzde
Göz yorgunluğu ve baş ağrısını gidermesi	4	20,0	20,0	20,0
Bilgisayar ışığını süzüp zararlı ışınlardan koruması	3	15,0	15,0	35,0
Gözlerdeki kızarma ve yaşarmayı gidermesi	1	5,0	5,0	40,0
Parlamayı önleyip net görüş sağlaması	1	5,0	5,0	45,0
Yaşam kalitesini yükseltmesi, genellikle olumlu dönütler alınması ve yeniden tercih edilmesi	10	50,0	50,0	95,0
Geri dönüt alınmadı	1	5,0	5,0	100,0
Toplam	20	100,0	100,0	

Tablo 12. C Sorusuna Verilen Cevaplar (Olumsuz Geri Dönüt)

	Sayı	Yüzde	Geçerli Yüzde	Kümülatif Yüzde
Olumsuz geri dönüt alınmadı	11	55,0	55,0	55,0
Sarımtırak bir görüntü oluşması	6	30,0	30,0	85,0
Göz kuruluğu yapması	1	5,0	5,0	90,0
Geri dönüt alınmadı	1	5,0	5,0	95,0
%30-40 olumsuz geri dönüt oluyor	1	5,0	5,0	100,0
Toplam	20	100,0	100,0	

2.2.3. Uzman Göz Doktorları ile Yapılan Yarı-Yapılandırılmış Mülakatlardan Elde Edilen Veriler

Trabzon İl Sağlık Müdürlüğünden alınan izine dayanarak Trabzon Merkezdeki iki devlet hastanesinde Uzman/Operatör Göz Doktoru olarak çalışan doktorlardan 8'i ile yarı-yapılandırılmış mülakat gerçekleştirilmiştir. Elde edilen cevaplar, mülakattaki örneklem sayısının az olması nedeni ile kümülatif dağılımda belirtilmemiştir. Araştırmada yol gösterici olması bakımından doktorlar ile yapılan mülakatlardan elde edilen cevaplar aşağıda listelenmiştir:

a) Mavi ışık filtreli gözlük kullanımı retinayı zararlı ışınlardan koruyarak göz yorgunluğu, göz ağrısı ve göz kuruluğunu önler.

b) Mavi ışık filtreli gözlükler, daha çok ekran karşısında fazla zaman geçiren meslek gruplarına önerilir.

c) Mavi ışık filtreli gözlük kullanılmadığı takdirde, kuru göz sendromu, ARMD (maküla dejenerasyonu), göz yorgunluğu gibi rahatsızlıklar ortaya çıkabilir.

d) Kırma kusuru yüksek olan hastalara (katarakt, sarı nokta hastalıkları), genetik olarak retina dejenerasyonuna yatkın olan hastalara ve çocuk hastalara mavi ışık filtreli gözlük kullanımı önerilmemektedir.

e) Mavi ışık filtresi hem dereceli hem de VP camlara uygulanabilmektedir.

3. SONUÇ

Yapılan çalışmadan elde edilen sonuçlara göre, mavi ışık filtreli gözlük kullanımına daha çok ekran karşısında fazla zaman (5-8 saat) geçiren meslek gruplarında çalışanlarda ve ekran

karşısında göz yorgunluğu/sulanması/yanması/kızarması gibi şikayetleri olan bireylerde rastlanmaktadır. Çocuk yaştaki bireyler ile göz kırma kusuru yüksek olan ve retina dejenerasyonuna genetik yatkınlığı olan bireylere mavi ışık filtreli gözlük kullanımı önerilmemektedir. Mavi ışık filtreli gözlüğün göz yorgunluğunu azalttığı, ekran karşısında parlamayı engellediği ve gözü zararlı ışınlardan koruduğu, göz-baş ağrısı ve göz sulanmasını önlediği tespit edilmiştir. Mavi ışık filtreli gözlüğün bu çalışmada tespit edilen olumsuz etkisi ise renk kalitesine etki ederek sarımtırak bir görüntü oluşturmasıdır. Mavi ışığa karşı hassasiyeti olan ve ekran karşısında fazla zaman harcayan bireyler mavi ışık filtreli gözlük kullanmadıkları takdirde ileriki zamanlarda kuru göz sendromu, ARMD (maküla dejenerasyonu) ve göz yorgunluğu gibi rahatsızlıklar yaşayabilirler.

KAYNAKÇA

Ateş, E., & Aytaç, N. (2019). Adana İl Sağlık Müdürlüğünde Bilgisayar Kullanan Çalışanlarda Göz Kuruluğu Sıklığının Değerlendirilmesi. 3. International 21. National Public Health Congress-2019.

Türkoğlu, K., Türkoğlu, M. E., & Kaya, E. (2013). Gözlük Kullanıcılarının Sorunları, Beklentileri ve Çözüm Önerileri. Suleyman Demirel University The Journal of Visionary, 4 (8), 63-82.

GÖZLÜK KULLANIMI VE SATIŞLARINI MEVSİMSEL OLARAK ETKİLEYEN FAKTÖRLERİN BELİRLENMESİ VE ÇÖZÜM ÖNERİLERİ[1]

Nimet ÖKMEN[2]

Emine TATAR[3]

Kerime AKYOL[3]

Berat ÖĞÜT[2]

Özge ERDEM[4]

1. GİRİŞ

Dört mevsim boyunca kullanılan gözlükler göz sağlığımızı korurken bir yandan da bazı sorunlara yol açar. Kış aylarında sürekli optik gözlük kullanmak zorunda olanların en büyük problemi, camların buğulanmasıdır. Kış mevsiminde en çok tercih edilen camlar, polarize camlardır. Bunun sebebi, polarize camların karlı havalarda buğulanmayı önlemesi, fazla ışığı azaltması ve böylece rahat bir görüş alanı sağlamasıdır. Yaz mevsiminde ise, fazla ışıklı ortamlarda koyulaşarak kişiyi ışıktan koruduğu için fotokromatik camlar daha çok tercih edilir. Gözlük

[1] Bu çalışma, TÜBİTAK 2209-A Üniversite Öğrencileri Araştırma Projeleri Destek Programı tarafından 2023 yılı/1.dönem 1919B012307603 proje numarası ile desteklenen "Gözlük kullanımı ve satışlarını mevsimsel olarak etkileyen faktörlerin belirlenmesi ve çözüm önerileri" isimli projeden üretilmiştir.

[2] Optisyen, Bayburt Üniversitesi, Sağlık Hizmetleri MYO, Tıbbi Hizmetler ve Teknikler Bölümü, nimetokmen23@gmail.com, beratogut161@icloud.com

[3] Öğrenci, Bayburt Üniversitesi, Sağlık Hizmetleri MYO, Tıbbi Hizmetler ve Teknikler Bölümü, emime.ttr4618@gmail.com, akyolkerime8@gmail.com

[4] Doç. Dr., Bayburt Üniversitesi, Sağlık Hizmetleri MYO, Tıbbi Hizmetler ve Teknikler Bölümü, ozgeerdem@bayburt.edu.tr, ORCID: 0000-0003-4542-941X.

kullanıcılarının mevsimsel olarak karşılaştıkları pek çok problem vardır. Aşırı soğuk ve sıcak ortamlar, sisli hava, kar ve yağmur yağışı, don olayları gibi aniden değişen ya da uzun süren olumsuz hava şartları rahat bir şekilde gözlük kullanımını engeller. Mevsimsel olarak oluşan ve gözlük kullanıcılarını pek çok açıdan etkileyen çatlama, buğulanma, kayma gibi dezavantajlı durumların belirlenmesi ve bu sorunlara uygun çözüm önerileri getirilmesi hem gözlük kullanıcılarına uzun süreli ve ergonomik gözlük kullanım imkânı sağlayacak hem de gözlük satışlarını iyileştirecek bir yöntemdir.

Bu projede, anket çalışması yapılarak gözlük satışlarında 18-45 yaş arası 70 adet gözlük kullanıcısının mevsimsel olarak gözlük kullanımında karşılaştıkları sorunlar belirlenmiştir. Belirlenen sorunların gözlük satışları üzerine etkisini araştırmak için 30 adet optisyenlik müessesesi ile yarı-yapılandırılmış mülakat yapılmıştır. Elde edilen veriler analiz edilerek tespit edilen mevsimsel problemlere çözüm önerileri sunulmuştur.

2. ÇALIŞMA İÇERİĞİ

2.1. Materyal/Metot

Çalışmanın örneklemini Erzurum ve Bayburt illerindeki 18-45 yaş arası toplam 70 adet gözlük kullanıcısı ile Diyarbakır ve Muğla illerinde gözlük satışı yapan toplam 30 adet optisyenlik müessesesi oluşturmaktadır. Çalışmada kullanılan ankette toplam 10 adet demografik ve açık uçlu soru yer almıştır. Anketler gönüllülük esasına uyularak yüzyüze yapılmıştır. Optik müesseseler ile yapılan mülakatlarda ise 6 adet açık uçlu soru kullanılmıştır. Mülakatlar, izin dahilinde ses kaydı altında yapılmıştır. Mülakat sırasında duruma göre yeni sorular da sorulmuştur. Çalışma konusunun belirlenmesi ve anket sorularının hazırlanması için literatürdeki kaynaklardan (Türkoğlu, Türkoğlu, & Kaya, 2013; Ateş & Aytaç 2019)

yararlanılmıştır. Araştırmada sorulara verilen cevaplar SPSS 22.0 ile frekans dağılımları incelenerek değerlendirilmiştir.

2.2. Bulgular

2.2.1. Anket Formlarından Elde Edilen Veriler

Çalışmada, 18-45 yaş arası Bayburt ve Erzurum'da yaşayan toplam 70 adet gözlük kullanıcısına uygulanan anket formlarından elde edilen veriler analiz edilmiş ve sonuçlar aşağıda tablolar halinde sunulmuştur.

Bayburt ve Erzurum illerinde anket çalışmasına katılan gözlük kullanıcılarının cinsiyet dağılımı Tablo 1'de verilmiştir. Buna göre, ankete katılanların cinsiyet dağılımının (% 52,86 erkek, % 47,14 kadın) yaklaşık olarak orantılı olduğu görülür.

Tablo 1. Anket Çalışmasına Katılanların Cinsiyet Dağılımı

	Sayı	Yüzde (%)	Geçerli Yüzde	Kümülatif Yüzde
Erkek	37	52,86	52,86	52,86
Kadın	33	47,14	47,14	100,00
Toplam	70	100,00	100,00	

Bayburt ve Erzurum illerinde anket çalışmasına katılanların yaş dağılımı Tablo 2'de verilmiştir. Buna göre ankete katılım isteğinin ağırlıklı olarak 18-25 (% 37,15) ve 26-35 (% 35,71) yaş gruplarında olduğu görülür.

Tablo 2. Anket Çalışmasına Katılanların Yaş Dağılımı

	Erkek	Kadın	Toplam Sayı	Yüzde (%)	Geçerli Yüzde	Kümülatif Yüzde
18-25	10	16	26	37,15	37,15	37,15
26-35	16	9	25	35,71	35,71	72.86
36-45	11	8	19	27,14	27,14	100,00
Toplam	37	33	70	100,00	100,00	

Anket çalışmasına katılanların göz rahatsızlıkları Bayburt ve Erzurum illeri için sırasıyla Tablo 3 ve Tablo 4'de verilmiştir. Buna göre toplam anket katılımcı sayısının (70 kişi) yaklaşık %

35'inin miyop ve % 26'sının ise astigmat göz rahatsızlığına sahip olduğu tespit edilmiştir. Bayburt ilinde miyop göz rahatsızlığı, Erzurum ilinde ise miyop ile astigmat göz rahatsızlıkları öne çıkmıştır.

Tablo 3. Bayburt İlinde Anket Çalışmasına Katılanların Göz Rahatsızlıkları

	Erkek	Kadın	Toplam Sayı	Yüzde (%)
Miyop	8	7	15	21,43
Hipermetrop	3	0	3	4,28
Astigmat	4	4	8	11,43
Miyop ve astigmat	3	4	7	10,00
Hipermetrop ve astigmat	2	0	2	2,86
Toplam	20	15	35	50,00

Tablo 4. Erzurum İlinde Anket Çalışmasına Katılanların Göz Rahatsızlıkları

	Erkek	Kadın	Toplam Sayı	Yüzde (%)
Miyop	8	2	10	14,29
Hipermetrop	4	4	8	11,43
Astigmat	3	7	10	14,29
Miyop ve Astigmat	1	5	6	8,57
Hipermetrop ve Astigmat	1	0	1	1,42
Toplam	17	18	35	50,00

Anket çalışmasına katılanların gözlük kullanım süreleri Bayburt ve Erzurum illeri için Tablo 5 ve Tablo 6'da verilmiştir. Buna göre, Bayburt ve Erzurum illerindeki katılımcılar sırasıyla ağırlıklı olarak 6-9 yıldır ve 3-6 yıldır gözlük kullanmaktadırlar.

Tablo 5. Bayburt İlinde Anket Çalışmasına Katılanların Gözlük Kullanım Süreleri

	Erkek	Kadın	Toplam	Yüzde
1 yıl-3 yıl	5	3	8	11,43
3 yıl-6 yıl	1	4	5	7,14
6 yıl-9 yıl	8	4	12	17,14
10 yıl ve üzeri	6	4	10	14,29
Toplam	20	15	35	50,00

Tablo 6. Erzurum İlinde Anket Çalışmasına Katılanların Gözlük Kullanım Süreleri

	Erkek	Kadın	Toplam	Yüzde
1 yıl-3 yıl	3	4	7	10,00
3 yıl-6 yıl	7	10	17	24.29
6 yıl-9 yıl	1	2	3	4,28
10 yıl ve üzeri	6	2	8	11,43
Toplam	17	18	35	50,00

Anket çalışmasına katılanların kullandıkları gözlük camı çeşitleri Bayburt ve Erzurum illeri için sırasıyla Tablo 7 ve Tablo 8'de verilmiştir. Buna göre, her iki il için de gözlük kullanıcılarının yaklaşık yarısının kullandıkları gözlük çeşidi hakkında bilgilerinin olmadığı tespit edilmiştir. Katılımcıların diğer yarısı ise verdikleri cevaplarda organik, kaplamalı, mineral ve mavi ışık filtreli gözlük camları kullandıklarını belirtmişlerdir.

Tablo 7. Bayburt İlinde Anket Çalışmasına Katılanların Kullandıkları Gözlük Camı Çeşitleri

	Erkek	Kadın	Toplam	Yüzde
Mineral cam	2	0	2	2,86
Organik cam	3	4	7	10,00
Kaplamalı cam	5	4	9	12.85
Mavi ışık korumalı cam	0	0	0	0,00
Cevapsız	10	7	17	24,29
Toplam	20	15	35	50,00

Tablo 8. Erzurum İlinde Anket Çalışmasına Katılanların Kullandıkları Gözlük Camı Çeşitleri

	Erkek	Kadın	Toplam	Yüzde
Mineral cam	3	2	5	7,14
Organik cam	3	4	7	10,00
Kaplamalı cam	2	3	5	7,14
Mavi ışık korumalı cam	0	1	1	1,43
Cevapsız	9	8	17	24,29
Toplam	17	18	35	50,00

Anket çalışmasına katılanların kullandıkları çerçeve çeşitleri, Bayburt ve Erzurum illeri için sırasıyla Tablo 9 ve Tablo 10'da verilmiştir. Buna göre her iki il için de katılımcılar, ağırlıklı olarak kemik ve metal çerçeve kullandıklarını belirtmişlerdir. Toplam katılımcı sayısının (70 kişi) % 41,46'sı kemik çerçeve cevabını verirken, % 29,99'u metal çerçeve cevabını vermiştir.

Tablo 9. Bayburt İlinde Anket Çalışmasına Katılanların Kullandıkları Çerçeve Çeşitleri

	Erkek	Kadın	Toplam	Yüzde
Kemik çerçeve	6	5	11	15,72
Metal çerçeve	6	3	9	12,85
Faset çerçeve	1	0	1	1,42
Nilör çerçeve	4	0	4	5,72
Cevapsız	3	7	10	14,29
Toplam	20	15	35	50,00

Tablo 10. Erzurum İlinde Anket Çalışmasına Katılanların Kullandıkları Çerçeve Çeşitleri

	Erkek	Kadın	Toplam	Yüzde
Kemik çerçeve	9	9	18	25,74
Metal çerçeve	5	7	12	17,14
Faset çerçeve	1	0	1	1,42
Nilör çerçeve	2	1	3	4,28
Cevapsız	0	1	1	1,42
Toplam	17	18	35	50,00

Anket çalışmasına katılanların gözlük kullanımı sırasında mevsimsel olarak karşılaştıkları sorunlar, Bayburt ve Erzurum

illeri için sırasıyla Tablo 11 ve Tablo 12'de listelenmiştir. Bunun için katılımcılara gözlük kullanırken en sık karşılaştıkları sorunlardan 3 tanesini mevsimi ile birlikte belirtmeleri istenmiştir. Bu kısımda katılımcılardan bazıları sadece bir sorun belirtmiş ya da ilgili soruyu cevapsız bırakmışlardır. Tablolar incelendiğinde, her iki il için de katılımcıların en çok kış ve yaz mevsimlerinde sorun yaşadıkları tespit edilmiştir. Kış şartlarının ağır geçtiği her iki il için gözlük kullanıcılarının kış mevsiminde sıklıkla gözlük camının buğulanması sorunu ile karşılaştıkları görülür. Yaz mevsimi sıcaklığının Ege ve Akdeniz bölgelerindeki illere göre nispeten daha düşük olduğu ve yazın kurak geçtiği her iki ilde yaz mevsiminde daha çok gözlüğün/çerçevenin terleme yapması, terleme nedeniyle gözlüğün yüzden kayması ve oksitlenme sorunlarının öne çıktığı tespit edilmiştir.

Tablo 11. Bayburt İlinde Anket Çalışmasına Katılanların Gözlük Kullanımı Sırasında Mevsimsel Olarak Karşılaştıkları Sorunlar

	İlkbahar	Yaz	Sonbahar	Kış
Buğulanma	0	0	0	26
Islanma nedeniyle görüş netliğinin bozulması	2	0	2	6
Yüzde iz çıkması/burnu, kulağı sıkma	0	0	0	0
Tozlanma/kirlenme	1	3	1	1
Terleme yapması	0	5	0	0
Camın/çerçevenin düşmesi/kayması	0	3	0	0
Parlama/yansıma yapması	0	2	0	0
Kaşıntı yapması	1	0	0	0
Oksitlenme	0	4	0	0
Toplam	4	17	3	33

Tablo 12. Erzurum İlinde Anket Çalışmasına Katılanların Gözlük Kullanımı Sırasında Mevsimsel Olarak Karşılaştıkları Sorunlar

	İlkbahar	Yaz	Sonbahar	Kış
Buğulanma	0	0	1	21
Islanma nedeniyle görüş netliğinin bozulması	0	0	1	3
Yüzde iz çıkması/burnu, kulağı sıkma	0	5	0	1
Tozlanma/kirlenme	0	1	0	5
Terleme yapması	0	8	0	0
Camın/çerçevenin düşmesi/kayması	0	4	0	0
Parlama/yansıma yapması	0	1	0	0
Kaşıntı yapması	0	1	0	0
Oksitlenme	0	6	0	0
Toplam	0	26	2	30

2.2.2. Optisyenlik Müesseseleri ile Yapılan Yarı-Yapılandırılmış Mülakatlardan Elde Edilen Veriler

Muğla ve Diyarbakır illerindeki toplam 30 adet optik müessese ile yapılan yarı-yapılandırılmış mülakatlardan elde edilen cevaplar aşağıda listelenmiştir:

a) Muğla ili katılımcılarına göre, gözlük satışı daha çok ilkbahar, yaz ve sonbahar aylarında artar. Diyarbakır ili katılımcılarına göre ise yaz ve kış aylarında gözlük satışında artış görülür. Numaralı ve numarasız güneş gözlüğü satışı Muğla'da yazın artarken, Diyarbakır'da yaz ve kış aylarında artar. Her iki il için de optik gözlük satışı, daha çok okul döneminde ve kış aylarında görülür. Sıklıkla antirefle kaplamalı, kolormatik, ultraviyole/mavi ışık korumalı, progresif ve polarize camlar ile ince çerçeveli gözlükler tercih edilir.

b) Muğla ve Diyarbakır illeri katılımcılarına göre, kış aylarında güneş gözlüğü satışı azalırken, numaralı gözlük satışı okul döneminde artar. Ayrıca, Muğla ili katılımcılarına göre kış

aylarında kolormatik cam satışı azalıp mavi ışık korumalı cam satışı artar.

c) Muğla ve Diyarbakır illeri katılımcılarına göre, cam/çerçeve/gözlük sapı kırılması, cam değiştirme, vida gevşemesi, çerçeve tamiri gibi sorunlar ile her mevsim karşılaşılır. Muğla ili katılımcılarına göre, yazın daha çok terleme nedeniyle gözlüğün kayması ve oksitlenme, çerçevenin yüze bol gelmesi nedeniyle burunluk değişimi gibi sorunlar öne çıkar. Diyarbakır ili katılımcılarına göre yazın daha çok cam üzerindeki kaplamanın bozulması ve çizilme sorunları olurken kış aylarında ise buğulanma sorunu görülür.

d) Muğla ve Diyarbakır ili katılımcılarına göre, gözlük kullanıcılarının karşılaştıkları sorunlara karşı yapılanlar şöyledir: Çerçeve kırılmalarına karşı müşterilere esnek çerçeveler önerilir. Kırılma ve çizilmelere karşı dirençli camlar önerilir. Oksitlenme ve terleme sorununa karşı hafif kemik çerçeveler önerilir. Cam çizilmesine karşı daha zor aşınan kaplamalar önerilir. Gözlük temizliği ve kullanımı hakkında bilgi verilir. Çerçeve tamiri ve cam değişimi yapılır. Ayrıca Diyarbakır ili katılımcılarına göre kışın buğulanmalara karşı sprey ve kaplamalar önerilir.

e) Muğla ili katılımcılarına göre, Muğla'nın turistik sıcak bir il olması nedeniyle güneş ışınlarından korunma yazın gözlük satışını olumlu etkileyen en önemli faktördür. Diyarbakır ili katılımcılarına göre ise, kışın kötü hava şartları ile yazın il dışına göç verilmesi gözlük satışını olumsuz etkiler.

f) Muğla ili katılımcılarına göre, güneş gözlüğü fiyatları kışın daha düşük iken optik gözlüklerin fiyatı mevsime göre değişmemektedir. Diyarbakır katılımcılarına göre ise, kışın güneş gözlüğü fiyatları ve yaz aylarında ise optik gözlük fiyatları indirimlidir.

3. SONUÇ

Bu çalışmadan elde edilen verilere göre, birbirine benzer iklime sahip olan Bayburt ve Erzurum illerinde en çok kış ve yaz mevsimlerinde gözlük kullanımında problemler ile karşılaşıldığı belirlenmiştir. Kış mevsiminde gözlük camının buğulanması, yaz mevsiminde ise gözlüğün/çerçevenin terleme yapması, terleme nedeniyle gözlüğün yüzden kayması ve oksitlenme sorunlarının yaşandığı tespit edilmiştir.

Birbirinden farklı iklime sahip olan Diyarbakır ve Muğla illerinde ise gözlük kullanımında farklı problemlerin yaşandığı tespit ediliştir. Yaz ve kış aylarında sıcaklık farkı daha fazla olan Diyarbakır ilinde yazın sıcaklığa bağlı olarak cam kaplaması bozulması sorunu, kışın ise buğulanma sorunu öne çıkmıştır. Yaz ve kış aylarındaki sıcaklık farkının az olduğu ve kış mevsiminin ılıman geçtiği Muğla ilinde ise, kışın öne çıkan belirgin bir sorun yoktur. Buna karşılık, yazın terleme nedeniyle burunluğun/çerçevenin kirlenmesi/gevşemesi ile yüzden kayması ve çerçevede oksitlenme problemleri görülmektedir. Her iki ilin coğrafi şartlarının farklılığı, Muğla ilinin tatil beldesi olması, Diyarbakır ilinin yazın göç vermesi ve kışın kötü hava şartlarına sahip olması gözlük satışlarını etkileyen faktörler olarak tespit edilmiştir.

Çalışmada belirlenen gözlük kullanımında ve satışında mevsimsel olarak karşılaşılan sorunlara çözüm önerileri aşağıda maddeler halinde verilmiştir.

a) Yaz mevsiminde yansımayı azaltma ve böylece net bir görüş sağlama amacıyla, fazla ışıklı ortamlarda koyulaşarak kişiyi ışıktan koruyan fotokromik camlar, parlama önleyici (yansıtıcı olmayan) kaplamalar, UV korumalı camlar ve asetat çerçeveler tercih edilebilir. Ayrıca, kahverengi, siyah ve mor renkli camlar güneş ışığından maksimum koruma sağlayan ve en sağlıklı bulunan güneş gözlüğü cam kategorisinde yer alır.

b)Yazın terleme nedeniyle oluşan oksitlenme sorunlarının önlenmesi için, kalitesiz metalden yapılan çerçeveler yerine korozyona dayanıklı titanyum kaplama çerçeveler ve ince kemik çerçeveler önerilebilir.

c) Yaz ve kış mevsiminde faset ve nilör gibi rim halkası hiç olmayan ya da yarım olan çerçevelerde kullanılan misina hava şartları ve kötü kullanım sonucu yıpranır. Bu gözlükler çatlamaya/kırılmaya daha meyillidir. Bu durumda, gözlük kullanmaya alışana kadar ve küçük yaşlarda esnek yapılı tam çerçevelerin kullanımı önerilebilir. Ayrıca trivex camlar kırılmaya oldukça dirençli olduğundan, özellikle faset çerçeveler için tercih edilebilir. Böylece sapların takıldığı yerde camda çatlama oluşması engellenir.

d) Kış mevsiminde karlı/yağmurlu havalarda ve ani sıcaklık değişimlerinde en iyi antirefle kaplamalı camlar dahi buğulanmaktadır. Buğulanmayı önlemek için antifog (buğu önleyici) spreyler ve zerofog kaplamalı camlar kullanılabilir. Ayrıca, camda oluşan buğulanma, mikrofiber cam temizleme bezleri ile temizlenmelidir.

e) Kışın yansıma ve parlamayı azaltması, zararlı ışınları absorbe etmesi ve böylece rahat bir görüş alanı sağlaması bakımından polarize camlar ve yansıma önleyici kaplamaya sahip güneş gözlükleri tercih edilebilir. Polarize güneş gözlüğü karlı yüzeylerde ve su yüzeyinde oluşan yansıma ve parlamaları engeller, yansıyan ışınların neden olduğu yorgunluk hissini azaltarak daha rahat bir görüş sağlar.

f) Dayanıklı bir güneş gözlüğü kullanmak isteyenlere polikarbon ve trivex camlar önerilebilir. Polikarbon, hem hafiftir hem de darbe direnci yüksek bir plastik malzemedir. Ayrıca, ek kaplamaya ihtiyaç duymadan yapısı gereği UV koruma sağlar. Trivex camlar da, özel bileşimi sayesinde, mineral ve organik camlara göre kırılmaya çok daha dirençlidir. Bu camlar, özellikle

spor yapanlara, tehlikeli iş ortamlarında çalışanlara ve çocuklara önerilebilir. Yine, İsviçre teknolojisi ile üretilen TR90 termoplastik malzemeden yapılan çerçeveler, hafiflik, esneklik ve dayanıklılık bakımından tercih edilebilir. Bu malzeme oldukça esnek olduğundan baskı altında bükülebilir ve yüzü rahatça kavrar.

g) Yazın toz vb. nedenle camlarda görülen çiziklere karşı toz ve kir tutmayan mineral camlar, organik camlara kıyasla, tercih edilebilir. Organik camlar yapısı gereği kolayca tozlanır ve hızlı kirlenir. Mineral camlar tozdan ve sıcaktan daha az etkilenir ve yüksek optik kaliteye sahiptir. Ayrıca, günümüzde polikarbonat ve trivex malzemeden yapılan çoğu gözlük camı, çizilmeye dayanıklı bir kaplamaya sahiptir. Bunun yanında, tozlanan camlar ılık su ile nazikçe ovalanarak temizlenmelidir, güçlü kimyasallar ve alkol kullanmak cam yüzeyindeki kaplamaya zarar verebilir.

h) Yazın ve kışın optik gözlük kullanan ve tv, dizüstü bilgisayar, bilgisayar, tablet ekranı karşısında fazla zaman geçiren bireylere mavi ışık filtreli camlar önerilebilir. Bu camlar, ekrandan yayılan ışığı yüksek oranda filtreleyerek göz yorgunluğu, göz kuruluğu, baş ağrısı, uyku problemi gibi sorunları engeller.

j) Gözlük kullanıcılarına, optik müesseselerdeki satışlar sırasında gözlük temizliği ve bakımı ile yüz şekline uygun gözlük seçimi hakkında bilgi verilebilir ve gözlük temizleme kitleri önerilebilir. Böylece, göz sağlığını koruyarak hem gözlük kullanımını kolaylaştıracak hem de gözlük kullanım süresini uzatacak önlemler alınması mümkündür.

KAYNAKÇA

Ateş, E., & Aytaç, N. (2019). Adana İl Sağlık Müdürlüğünde Bilgisayar Kullanan Çalışanlarda Göz Kuruluğu Sıklığının Değerlendirilmesi. 3. International 21. National Public Health Congress-2019.

Türkoğlu, K., Türkoğlu, M. E., & Kaya, E. (2013). Gözlük Kullanıcılarının Sorunları, Beklentileri ve Çözüm Önerileri. Suleyman Demirel University The Journal of Visionary, 4 (8), 63-82.

DETERMINATION OF THE OPTIMUM SAMPLE GEOMETRY IN GAMMA-RAY SPECTROMETRY: EXPERIMENTAL AND MONTE CARLO SIMULATION METHOD

Esra UYAR[1]

Saim Egemen YÜCEL[2]

Gökçen ASLAN AYDEMİR[3]

1. INTRODUCTION

Gamma (γ) decay occurs when a nucleus transitions from an excited state—where it possesses excess energy—to a more stable or lower-energy state. This excited state typically arises after an alpha (α) or beta (β) decay has taken place. Unlike α, β, or spontaneous fission, γ decay is not a form of decay that alters the number or type of nucleons within the nucleus. Instead, it involves the transition of the nucleus from an excited state to its ground state without changing the identity of the nucleus (Tanır, Bölükdemir and Koç, 2013). Gamma radiation, in essence, is a type of electromagnetic radiation, much like radio waves, microwaves, and visible light. However, it is found on the higher energy, shorter wavelength end of the electromagnetic spectrum.

Gamma rays interact with the crystal atoms inside a detector in three main ways: photoelectric absorption, Compton

[1] Gazi University, Faculty of Sciences, Department of Physics, Ankara, Turkey.

[2] Ankara University, Faculty of Engineering, Department of Physics Engineering, Tandoğan, Ankara, Turkey

[3] Gazi University, Graduate School of Natural and Applied Sciences, Department of Advanced Technologies, Ankara, Turkey

scattering, and pair production. In all three cases, free electrons are produced. These electrons lose their energy by ionizing and exciting the atoms in the detector medium, generating numerous electron-hole pairs (Gilmore, 2013). To obtain comprehensive information about incoming gamma rays, it is essential that they are fully absorbed within the detector. Consequently, the photoelectric effect is the preferred interaction mechanism in gamma spectroscopy. This preference arises because, during the photoelectric effect, an incoming gamma photon transfers its energy to an electron bound to an atom. As a result, the electron is ejected and becomes free, while the photon is absorbed by the electron and thereby annihilated. In the event of Compton scattering, an incoming photon interacts with a loosely bound, nearly free electron, ejecting the electron from its orbit. As the electron becomes free, the photon continues its motion with a change in direction and reduced energy, but it is not annihilated. Unlike photoelectric absorption and Compton scattering, pair production results from the interaction between a gamma ray and the atom as a whole. This interaction occurs within the Coulomb field of the nucleus and leads to the conversion of the gamma ray into an electron-positron pair. When a photon with energy greater than 1022 keV interacts with the atomic nucleus, it is annihilated, and in its place, an electron-positron pair is created.

Gamma-ray spectrometry is a widely used and useful technique for the identification and quantification of radionuclides found in samples of different geometries. High Purity Germanium (HPGe) detectors are used in this technique for their exceptional energy resolution, which allows for highly accurate measurements (Uyar and Bölükdemir, 2022). With HPGe detectors, natural and artificial radionuclides found in all kinds of geological, biological and environmental samples that emit gamma radiation are identified and their radioactivity values are determined (Azbouche, Mohamed and Hakim,

2015). However, the efficiency of an HPGe detector, especially its Full Energy Peak Efficiency (FEPE), is significantly influenced by the geometry of the sample being analyzed. This paper explores how varying the shape and size of the sample affects the FEPE, providing practical recommendations for optimizing experimental setups in gamma-ray spectroscopy.

FEPE is a crucial metric in gamma-ray spectroscopy, indicating how effectively a detector captures the complete energy of incoming gamma-ray photons (Priya et al., 2023). The efficiency of gamma-ray detectors, is closely related to time management in experimental setups and data analysis processes (Chuong et al., 2004). Efficiently managing time during measurements can significantly impact the quality of the data obtained. For instance, optimal time allocation allows researchers to conduct longer counting times when necessary, enhancing the statistical significance of the results and improving the detector's ability to accurately capture gamma-ray events. Several factors can affect this efficiency, including the distance between the sample and detector, the energy of the gamma rays, and, critically, the sample's geometry.

In previous studies, it has been established that the relationship between sample geometry and FEPE is not merely a theoretical concern; practical experiments have demonstrated that optimizing sample shape and positioning can efficiency substantial improvements in measurement accuracy. Differences in sample geometry can lead to significant variations in detection efficiency, potentially resulting in inaccurate data if not properly accounted for. This issue becomes particularly important when dealing with small or irregularly shaped samples, where the relationship between the sample’s geometry and the detector’s efficiency is even more pronounced.

The calculation of FEPE value can be determined experimentally or by the Monte Carlo (MC) method. Using Monte Carlo method simulations is a crucial method in gamma-ray spectroscopy, especially when direct experimental measurements are difficult or not feasible. MC simulations allow for the detailed modeling of gamma photon interactions with the detector, taking into account variables such as detector geometry, sample shape, and photon energy (Lépy et al., 2019, Subercaze et al., 2022). By simulating a vast number of photon interactions, these calculations provide insight into the efficiency of the detector under various conditions. This method not only aids in optimizing detector design and predicting performance but also serves as a valuable tool for refining experimental setups. Importantly, comparing the results of MC simulations with experimental data is essential for validating the accuracy of the simulations (Barba-Lobo et al., 2024). Such comparisons help identify any discrepancies and refine the simulation models, ultimately enhancing the precision and reliability of FEPE measurements in both research and practical applications.

In this study, we focus on how different sample volume in cylindrical shaped geometry affects FEPE in gamma-ray spectroscopy experiments. The choice of sample geometry can significantly influence the efficiency with which the detector interacts with gamma photons, thereby impacting the accuracy of the measurements. By examining these various geometries, we aim to offer valuable insights that can help improve the accuracy and reliability of gamma spectroscopy experiments, particularly when dealing with different material types and shapes (Uyar, Özgür and Dikmen, 2023). By employing both experimental and Monte Carlo simulation methods, we aim to elucidate the complex interplay between sample geometry and detection efficiency.

In gamma-ray spectrometry laboratories, samples are prepared using appropriate containers depending on the amount of sample to be analyzed. In this study, the effect of sample geometry on the efficiency value, which is one of the important parameters determined by the user, was investigated and the optimum sample geometry for a certain amount of sample was investigated. The effect of sample geometry was examined by investigating in which size container a certain amount of sample in the laboratory would be prepared and analyzed to obtain higher efficiency counts. For this purpose, the same amount of sample was prepared in three different sized sample containers and efficiency values were obtained in the energy range of 46.5 keV and 1836 keV. The efficiency values were determined both experimentally and by two different Monte Carlo simulation methods, and the two methods were compared.

2. MATERIALS AND METHODS

2.1.The HPGe Detector

In this study, an Ortec GEM-C40P4 coaxial HPGe detector from the GEM series, featuring a 0.9 mm carbon fiber window and 40% relative efficiency, was utilized. The performance specifications and geometric details provided by the manufacturer are listed in Table 1. To minimize background radiation from sources like cosmic rays, 40K, and radionuclides from the uranium-thorium decay chain, the detector was shielded with a 10 cm thick lead layer, and graded with 1.6 mm copper and 1 mm tin liners. It also had a movable cover for additional protection. The detector was operated using the Ortec DSPEC 50, a digital signal processor, which was controlled by the MaestroPro Advanced Spectroscopy Software. This software was employed for spectral analysis and peak area calculations.

Table 1. The performance specifications and geometric characteristics of the detectors provided by the manufacturer

Performance specifications	**HPGe**
FWHM at 1.33 MeV, ^{60}Co	1.7 keV
FWHM at 122 keV, ^{57}Co	686 eV
Peak-to-Compton ratio, ^{60}Co	77:1
(Nominal) Efficiency at 1.33 MeV, ^{60}Co	47 %
FWTM/FWHM, ^{60}Co	1.9
FWFM/FWHM, ^{60}Co	2.5
High voltage bias and polarity	+2600V
Geometric characteristics	
Crystal diameter	63.9 mm
Crystal length	63.5 mm
Core diameter	8.8 mm
Core length	50 mm
Crystal to window distance	4 mm
End cap window	0.9 mm /Carbon fiber
Outer dead layer thickness	700 μm/Li
Inner dead layer thickness	0.3 μm/B

This detector provides sufficient performance for low and high energy gamma rays, allowing reliable measurements in a wide energy range. It can be said that thanks to these features, sensitive and accurate results can be obtained in areas such as nuclear physics, radiation safety and environmental monitoring.

2.2.Certified Reference Material

Firstly, the energy calibration of the detector was performed with standard point sources having energies between 59.5 keV and 1837 keV. The point sources used are ^{241}Am (38.2 kBq), ^{133}Ba (44.0 kBq), ^{137}Cs (40.7 kBq), ^{57}Co (43.0 kBq), ^{60}Co (41.5 kBq), ^{54}Mn (41.2 kBq), ^{22}Na (41.5 kBq), and ^{88}Y (39.8 kBq) purchased from Eckert&Ziegler. The active surface dimensions of each point source are 1 mm and the overall dimensions 23.5 x 11 x 2 mm. The relative uncertainties of all point sources are 3%.

In this study, certified reference material containing multi-radionuclides was used, the properties of which are given in Table 2. Table 2 summarizes the gamma-ray energies of different

radioisotopes and the certified activity values of these isotopes. Isotopes in different energy ranges allow to evaluate the performance of detectors in both low and high energy ranges. Thus, energy accuracy and activity calibrations of detectors can be optimized by using these reference materials, which contributes to obtaining more sensitive and reliable results.

In order to examine the efficiency change in a wide energy range, a multinuclide source containing nuclides with gamma-ray energies between 46.5 keV and 1836 keV was prepared in three different geometries.

Table 2. Gamma-ray energy, and certified activity values of reference material

Reference material	Gamma-ray energy (Radionuclide)	Certified activity values for radionuclides (kBq)
Sand matrix* (SiO_2)	46.5 keV (^{210}Pb)	84.4
	59.5 (^{241}Am)	8.47
	88.0 (^{109}Cd)	112.1
	122.1 (^{57}Co)	4.53
	165.9 (^{139}Ce)	5.74
	391.7 (^{113}Sn)	22.0
	661.7 (^{137}Cs)	19.95
	898.0 (^{88}Y)	45.3
	1173.2 (^{60}Co)	23.6
	1332.5 (^{60}Co)	23.6
	1836.1 (^{88}Y)	45.3

*This source was purchased from Eckert and Ziegler Nuclitec GMBH.

2.3.Experimental

The experimental part of the study includes the investigation of the effect of the sample container geometry on the full energy peak efficiency. For this purpose measurements were made using a multinuclide source distributed in a sand matrix supplied by Eckert&Ziegler Nuclitec GMBH. Samples prepared in three different geometries from multinuclide standard sources were repeated three times at the end cap and center of the detector at times when good counting statistics were obtained.

Figure 1. Schematic representation of the sample container with

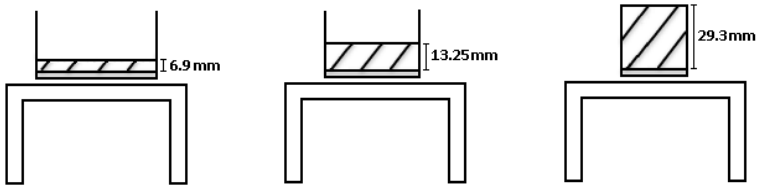

a) b) c)

a) 100 ml volume, **b)** 60 ml volume, **c)** 15 ml volume

In the study true coincidence summing (TCS) and self-absorption corrections. which are among the correction factors that need to be calculated for accurate and precise results in gamma-ray spectrometry were included in the calculations. Self-absorption correction factors were determined by averaging the linear attenuation coefficients (μ) obtained from GESPECOR and NIST XCOM (Photon Cross Sections Database). TCS correction factors were obtained using the GESPECOR Monte Carlo simulation program.

2.4.Monte Carlo Simulations

Two types of Monte Carlo simulation software are used in gamma-ray spectrometry: general purpose codes (GEANT4, MCNP, PENELOPE) and dedicated purpose codes such as GECPECOR (Sima, Arnold and Dovlete, 2001), DETEFF (Díaz, Cornejo and Jurado, 2008), and ANGLE (). Dedicated codes are designed with a user-friendly interface and can be applied to derive computational results directly from input data.

Monte Carlo programs are essential tools in the simulation of complex physical systems, particularly in scenarios where analytical solutions are difficult or impossible to obtain. In the context of High-Purity Germanium (HPGe) detectors, these programs are invaluable for accurately modeling the interaction of gamma rays with the detector material. By simulating millions

of individual photon interactions, Monte Carlo methods can predict the detector's response to various source geometries and energies with high precision. This level of detail is crucial for tasks such as determining full energy peak efficiency (FEPE), which depends on factors like source position, detector geometry, and the presence of any attenuating materials.

In HPGe detector simulations, understanding and accurately predicting FEPE is critical because it directly affects the quantification of radionuclide activities in gamma-ray spectrometry. Monte Carlo simulations allow researchers to account for complex effects like photon scattering, absorption, and coincidence summing, which are often challenging to measure experimentally. By providing a virtual environment where these factors can be meticulously controlled and varied, Monte Carlo programs help bridge the gap between theoretical models and experimental reality, ensuring that the efficiency values obtained are reliable and representative of actual detector performance. This capability is especially important when high precision is required, such as in environmental monitoring, nuclear medicine, and radiological safety assessments.

Computational methods are used to evaluate matrix and density effects and coincidence summation effects for full calibration of the gamma-spectrometry system or to generate efficiency curves for arbitrary measurement conditions.

2.4.1. GESPECOR

GESPECOR (Germanium SPectra CORrection) is a specialized Monte Carlo-based software designed for gamma-ray spectrometry. Its primary function is to calculate key correction factors such as efficiency, matrix effects, and coincidence summing effects for various gamma-ray detection setups (Sima and Arnold, 2002). The software is versatile, supporting different types of High-Purity Germanium (HPGe) detectors, including

coaxial, planar, and well-type configurations, as well as Ge(Li) detectors. It also accommodates a range of source geometries like point sources, cylindrical or spherical sources, and Marinelli beakers.

One of GESPECOR's standout features is its ability to accurately compute the full energy peak efficiency (FEPE) while accounting for matrix effects and coincidence summing effects-critical parameters that influence the accuracy of gamma-ray spectrometry (Arnold and Sima, 2004). The software delivers these results with well-defined uncertainties, enhancing its reliability for researchers and professionals in the field. Its user-friendly interface simplifies the execution of complex calculations, making it accessible even for non-experts.

Originally developed to handle self-attenuation and coincidence summing corrections, GESPECOR has evolved to provide comprehensive solutions for efficiency calculations across different detector geometries and measurement configurations. The methods employed in the software are based on the work of Sima, Arnold and Dovlete, 2001), and the tool has become a go-to for correcting for effects that cannot be easily accounted for experimentally. Its ability to simulate detector responses under various conditions is especially valuable when experimental calibration is not feasible.

In our research, GESPECOR was instrumental in accounting for true coincidence summing effects and efficiency values in specific isotopes and generating theoretical efficiency values. We then compared these values with our experimental results to ensure accuracy. The software allowed us to supplement and validate our findings, ensuring that the data obtained from gamma-ray spectrometry were both accurate and reproducible.

By integrating GESPECOR into our analysis process, we ensured that our gamma-ray spectrometry measurements were

robust, contributing to the overall reliability and consistency of our research. This combination of computational and experimental approaches allowed us to cross-verify results, providing a strong foundation for the conclusions drawn from our work.

3. RESULTS AND DISCUSSION

In this study, a certain amount (28.7 grams) of certified multinuclide standard source with sand matrix composition was prepared in three different sized sample containers and the change in efficiency was investigated. The efficiency values obtained from the experimental and simulation programs are given in Table 3-5.

Table 3. Experimental and Monte Carlo simulated FEPEs with GESPECOR for 100 ml volume container.

Nuclide	Energy (keV)	Experimental FEPE (U_{exp} %)	GESPECOR MC calculated FEPE	*% Difference from Experimental FEPE
Pb-210	46.5	0.1537	0.1607	4.6
Am-241	59.5	0.2073	0.2162	4.3
Cd-109	88.0	0.2109	0.2208	4.7
Co-57	122.1	0.1828	0.1903	4.1
Ce-139	165.9	0.1332	0.1367	2.6
Sn-113	391.7	0.0722	0.0739	2.4
Cs-137	661.7	0.0463	0.0472	1.9
Y-88	898.0	0.0315	0.0312	1.1
Co-60	1173.2	0.0251	0.0252	0.3
Co-60	1332.5	0.0227	0.0229	0.9
Y-88	1836.1	0.0172	0.0174	1.2

In Table 3, where the experimental and Monte Carlo simulated FEPE values with GESPECOR are given for a 100 ml volume container, it is seen that the difference between the

experimental value and the simulated value varies between 0.9-4.7 %.

A very good agreement is observed between GESPECOR simulations and experimental results; the differences are generally below 5%. This shows that GESPECOR software can produce accurate simulations and model real experimental conditions to a large extent.

Table 4. Experimental and Monte Carlo simulated FEPEs with GESPECOR for 60 ml volume container

Nuclide	Energy (keV)	Experimental FEPE (U_{exp} %)	GESPECOR MC calculated FEPE	*% Difference from Experimental FEPE
Pb-210	46.5	0.2151	0.2246	4.4
Am-241	59.5	0.2177	0.2262	3.9
Cd-109	88.0	0.2226	0.2295	3.1
Co-57	122.1	0.1939	0.2020	4.2
Ce-139	165.9	0.1446	0.1505	4.1
Sn-113	391.7	0.0764	0.0785	2.7
Cs-137	661.7	0.0485	0.0492	1.5
Y-88	898.0	0.0325	0.0330	1.7
Co-60	1173.2	0.0260	0.0261	0.4
Co-60	1332.5	0.0233	0.0233	0.4
Y-88	1836.1	0.0173	0.0174	0.6

Table 4 presents the comparison of FEPE calculated by experimental and GESPECOR MC simulations on various nuclides for a 60 ml volume container. The difference between the experimental data and the simulation results according to the energy levels of the nuclide is shown in the % difference column. According to the results in the table, the differences between the FEPE values calculated by GESPECOR and the experimental data are generally low and range from 0.4% to 4.4%.

Table 5. Experimental and Monte Carlo simulated FEPEs with GESPECOR for 15 ml volume container

Nuclide	Energy (keV)	Experimental FEPE (U_{exp} %)	GESPECOR MC calculated FEPE	*% Difference from Experimental FEPE
Pb-210	46.5	0.0763	0.0800	4.9
Am-241	59.5	0.1228	0.1287	4.8
Cd-109	88.0	0.1240	0.1278	3.1
Co-57	122.1	0.1076	0.1115	3.6
Ce-139	165.9	0.0809	0.0834	3.2
Sn-113	391.7	0.0413	0.0427	3.4
Cs-137	661.7	0.0283	0.0290	2.5
Y-88	898.0	0.0188	0.0192	2.3
Co-60	1173.2	0.0162	0.0165	1.6
Co-60	1332.5	0.0145	0.0148	1.7
Y-88	1836.1	0.0103	0.0104	1.1

In Table 5, where the experimental and Monte Carlo simulated FEPE values with GESPECOR are given for a 15 ml volume container, it is seen that the difference between the experimental value and the simulated value varies between 1.1-4.9 %. It was observed that GESPECOR simulations provide good agreement with experimental data for a 15 ml volumetric container and offer high accuracy especially at high energy levels.

Fig. 2. Comparison of experimental efficiency curve graph for all sample containers

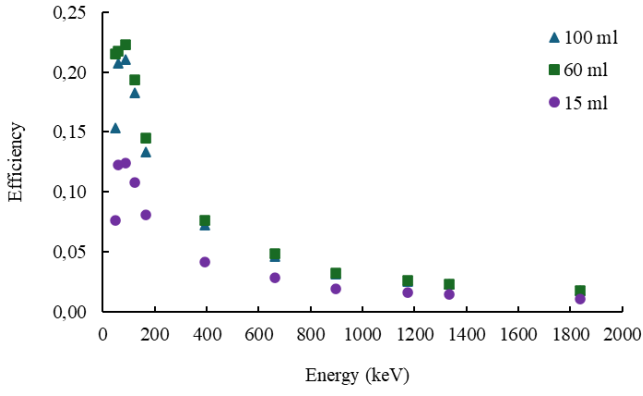

In Fig. 2, the graph of the calculated experimental efficiency curve for all sample containers is shown. As seen in the figure, the highest efficiency values were obtained using the 60 ml sample container.

As a result, the container volume has a large impact on the detection efficiency, especially at low energies, while this effect decreases as the energy increases. This can be explained by the decrease in interaction probabilities at higher energies. The optimized geometry likely allows for better photon interactions within the material, leading to more effective detection of gamma rays. In the low-energy region (below ~200 keV), the efficiencies for all sample sizes are relatively higher, with the 60 ml sample achieving the highest values. This is due to better absorption of lower-energy gamma photons, which is consistent with typical detector behavior.

4. CONCLUSIONS

The motivation of this study was to investigate the effect of optimum sample geometry on full energy peak efficiency (FEPE) in gamma-ray spectrometry. Using both experimental methods and Monte Carlo simulations, the impact of different sample container volumes (100 ml, 60 ml, 15 ml) on efficiency was analyzed. The results revealed that sample geometry significantly influences efficiency, with larger container volumes generally resulting in higher FEPE values. However, if the sample amount is limited, the height and diameter of the selected sample container become important. According to the results obtained in this study, when comparing larger volume containers such as 60 ml (44 mm inner diameter and 13.25 mm height) and 100 ml (56 mm inner diameter and 6.9 mm height), it was observed that not only an increase in sample height or a larger diameter, but both having optimal values, improves the efficiency.

By determining the optimum sample geometry, the differences between experimental and Monte Carlo simulated efficiencies were calculated to be within the range of 0.4%-4.9%. The fact that this difference is less than 5% for 11 different gamma-ray energies in the range of 46.5 keV to 1836.1 keV indicates that the experimental and simulation results are in good agreement.

In conclusion, the study emphasized that determining the optimum geometry requires the sample to have sufficient height and diameter. Proper selection of these parameters enhances the efficiency of gamma photon interaction with the detector, thus improving the accuracy of the measurements.

REFERENCES

Arnold, D., & Sima, O. (2004). Application of GESPECOR software for the calculation of coincidence summing effects in special cases. *Applied Radiation and Isotopes*, *60*(2-4), 167-172. https://doi.org/10.1016/j.apradiso.2003.11.011

Azbouche, Ahmed, Mohamed Belgaid, ve Hakim Mazrou. 2015. "Monte Carlo Calculations of the HPGe Detector Efficiency for Radioactivity Measurement of Large Volume Environmental Samples". *Journal of Environmental Radioactivity* 146:119-24. doi: 10.1016/j.jenvrad.2015.04.015.

Barba-Lobo, A., Expósito-Suárez, V. M., Suárez-Navarro, J. A., & Bolívar, J. P. (2024). A new methodology for efficiency calibration of uncharacterized Ge detectors by using characterized Ge detectors. *Radiation Physics and Chemistry*, 221, 111763. https://doi.org/10.1016/j.radphyschem.2024.111763

Chuong, H. D., Huynh Duy Khang, N., Thi Ngoc Trang, L., Thi Truc Linh, N., Thanh Sang, T., Thanh Dat, N., & Duc Tam, H. (2024). A comparative study on full-energy peak efficiency calibration methods for HPGe detector: Virtual point detector, curve fitting, and machine learning models. *Nuclear Instruments and Methods in Physics Research Section A: Accelerators, Spectrometers, Detectors and Associated Equipment*, *1058*, 168941. https://doi.org/10.1016/j.nima.2023.168941

Díaz, N. C., & Vargas, M. J. (2008). DETEFF: An improved Monte Carlo computer program for evaluating the efficiency in coaxial gamma-ray detectors. *Nuclear Instruments and Methods in Physics Research Section A: Accelerators, Spectrometers, Detectors and Associated*

Equipment, *586*(2), 204-210. https://doi.org/10.1016/j.nima.2007.11.072

Gilmore, G. (2013). *Practical Gamma-ray Spectrometry 2nd Edition*, England: John Wiley & Sons Ltd.

Lépy, M. C., Thiam, C., Anagnostakis, M., Galea, R., Gurau, D., Hurtado, S., Zhang, M. (2019). A benchmark for Monte Carlo simulation in gamma-ray spectrometry. *Applied Radiation and Isotopes*, *154*, 108850. https://doi.org/10.1016/j.apradiso.2019.108850

Priya, M. R., Thilagam, L., Renuga, S., & Mohapatra, D. K. (2023). Estimation of photopeak efficiency for IAEA gamma standards of different geometries using HPGe and 3″x3″ NaI(Tl) gamma spectrometry systems. *Nuclear and Particle Physics Proceedings*, *341*, 44-47. https://doi.org/10.1016/j.nuclphysbps.2023.09.016

Sima, O., & D. Arnold. 2002. "Transfer of the Efficiency Calibration of Germanium Gamma-Ray Detectors Using the GESPECOR Software". *Applied Radiation and Isotopes* 56(1-2):71-75. doi: 10.1016/S0969-8043(01)00169-5.

Sima, O., D. Arnold, & C. Dovlete, (2001). "GESPECOR: A Versatile Tool in Gamma-Ray Spectrometry".

Subercaze, A., Sauzedde, T., Domergue, C., Destouches, C., Philibert, H., Fausser, C., Zoia, A. (2022). Effect of the geometrical parameters of an HPGe detector on efficiency calculations using Monte Carlo methods. *Nuclear Instruments and Methods in Physics Research Section A: Accelerators, Spectrometers, Detectors and Associated Equipment*, *1039*, 167096. https://doi.org/10.1016/j.nima.2022.167096

Tanır, A.G., Bölükdemir, M.H., Koç, K. (2013), *Radyasyon ve Radyasyondan Korunma Fiziği, İkinci. Ed.,* Ankara: Palme Yayınevi.

Uyar, E., & Bölükdemir, M. H. (2022). The effect of front edge on efficiency for point and volume source geometries in p-type HPGe detectors. *Nuclear Engineering and Technology*, *54*(11), 4220-4225. https://doi.org/10.1016/j.net.2022.06.009

Uyar, E., Özgür, M., & Dikmen, H. (2023). *Effect of Sample Position on Efficiency in Gamma-Ray Spectroscopy*. Turkish Journal of Nuclear Sciences, 36-2, 14-20.

ADVANCES IN WİDE BANDGAP SEMICONDUCTOR DIODES (SiC, GaN): A REVOLUTION IN POWER ELECTRONICS

İlhan CANDAN[1]

Sezai ASUBAY[2]

1. INTRODUCTION

Power electronics play a pivotal role in modern technologies, from consumer electronics to industrial machinery, renewable energy systems, and electric vehicles (EVs) (Abu-Rub, Malinowski, & Al-Haddad, 2014; Chan & Chau, 1997). Central to power electronics are semiconductor diodes, which perform critical tasks such as current rectification, switching, and voltage regulation. Traditional silicon (Si) diodes have long been the standard for these applications (Iannaccone, Sbrana, Morelli, & Strangio, 2021). However, as the demand for more efficient, higher-performance devices continues to grow, silicon is reaching its physical limits in terms of efficiency, speed, and thermal management. In response, wide bandgap (WBG) semiconductors, particularly silicon carbide (SiC) and gallium nitride (GaN), have emerged as the next generation of materials capable of overcoming these limitations (Nguyen et al., 2021).

Wide bandgap semiconductors offer several advantages over conventional silicon-based devices, including higher breakdown voltages, faster switching speeds, and superior

[1] Arş. Gör Dr.; Dicle Üniversitesi Fen Fakültesi Fizik Bölümü. ilhan.candan@dicle.edu.tr ORCID: 0000-0001-9489-5324.

[2] Prof. Dr., Dicle Üniversitesi Fen Fakültesi Fizik Bölümü. Sezai.asubay@gmail.com, ORCID: 0000-0003-2171-8479.

thermal conductivity. These properties make WBG diodes ideal for high-power, high-frequency, and high-temperature applications, driving their adoption in fields such as electric vehicles, renewable energy, telecommunications, and industrial automation. This chapter explores the advances in SiC and GaN diodes, their unique properties, key applications, and the challenges they face as they continue to revolutionize the power electronics landscape (Kizilyalli, Spahn, & Carlson, 2022).

Figure 1. Properties of Si, SiC, and GaN relevant materials

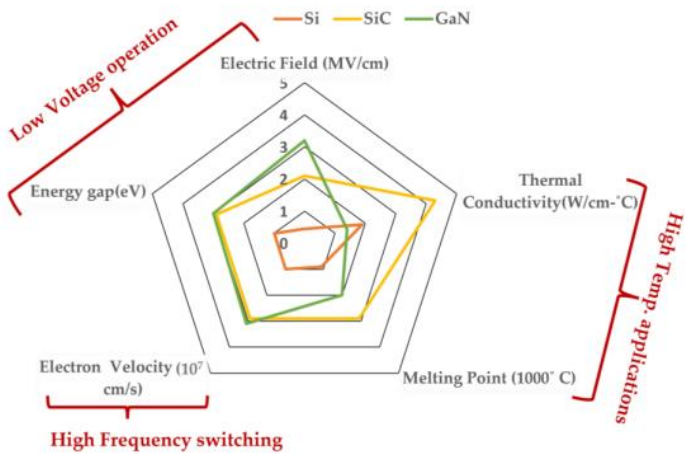

Source: (Rafin, Ahmed, & Mohammed, 2023).

Wide bandgap (WBG) semiconductor diodes, specifically silicon carbide (SiC) and gallium nitride (GaN), are revolutionizing the field of power electronics (Van Do, Trovão, Li, & Boulon, 2021). These advanced materials offer several advantages over traditional silicon-based devices, including higher breakdown voltages, faster switching speeds, and better thermal conductivity. As industries such as electric vehicles, renewable energy, telecommunications, and aerospace demand more efficient, compact, and high-performance power systems, SiC and GaN diodes have emerged as key enablers of this technological evolution (Roccaforte et al., 2018).

Power electronics are central to converting, controlling, and managing electrical energy in modern systems. Traditional silicon-based diodes, while effective for many years, face significant limitations, especially in high-power, high-frequency, and high-temperature applications. Silicon devices tend to suffer from higher power losses, slower switching speeds, and thermal management challenges, leading to inefficiencies in demanding applications like electric vehicle powertrains, high-voltage solar inverters, and high-speed telecommunications infrastructure (Rafin, Ahmed, Haque, et al., 2023).

In contrast, WBG semiconductors like SiC and GaN offer transformative benefits. SiC diodes excel in high-voltage, high-temperature environments, making them ideal for electric vehicles and renewable energy systems. GaN diodes, on the other hand, are favored for their rapid switching capabilities and high-frequency performance, critical for telecommunications and high-speed computing (Manandhar, 2021).

This chapter explores the technological advances in SiC and GaN diodes, examining their unique properties, applications, and the key challenges that remain. As the adoption of these materials grows, SiC and GaN diodes are poised to shape the future of power electronics, driving greater efficiency, reliability, and sustainability across a range of industries.

2. PROPERTIES OF WIDE BANDGAP SEMICONDUCTORS

The term "wide bandgap" refers to the energy difference between the valence band and the conduction band of a semiconductor material. A wider bandgap means that the material can operate at higher voltages and temperatures without experiencing significant energy losses or breakdown. Silicon, with a bandgap of 1.1 eV (electron volts), is limited in its ability

to handle extreme conditions. In contrast, SiC has a bandgap of 3.3 eV, and GaN has a bandgap of 3.4 eV, giving these materials significant advantages in high-power and high-temperature applications

Figure 2. SiC lattice's side view.

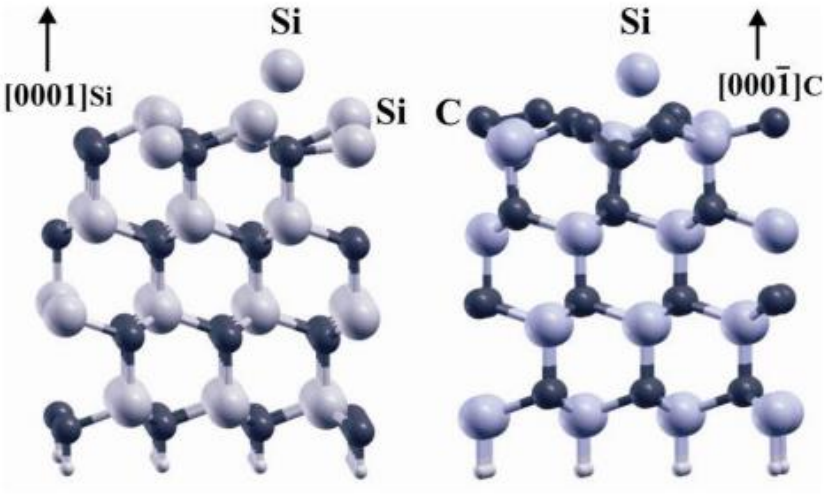

Source: (Ren & Zolper, 2003).

2.1.Breakdown Voltage

One of the key advantages of WBG semiconductors is their ability to withstand higher breakdown voltages. This property allows SiC and GaN diodes to handle higher electric fields without breaking down, making them ideal for high-voltage applications. For example, SiC diodes can operate at voltages exceeding 1,200 volts, compared to around 600 volts for silicon diodes (Agarwal, Burgard, Greiner, & Wendorff, 2016). This characteristic is crucial in applications like power inverters for electric vehicles and renewable energy systems, where high-voltage operation is necessary to maximize efficiency.

2.2.Switching Speed

SiC and GaN diodes also offer significantly faster switching speeds than their silicon counterparts (Singh, Chaudhary, & Khanna, 2022). Faster switching reduces energy losses due to heat, making power conversion more efficient. In high-frequency applications, such as telecommunications or power supplies, the ability to switch rapidly allows for smaller, lighter, and more efficient designs. GaN diodes, in particular, excel in high-frequency switching, making them well-suited for radiofrequency (RF) applications and other high-speed electronics.

2.3.Thermal Conductivity

Another critical advantage of WBG materials is their superior thermal conductivity. SiC, for example, has a thermal conductivity approximately three times higher than silicon (Ballestín-Fuertes, Muñoz-Cruzado-Alba, Sanz-Osorio, & Laporta-Puyal, 2021). This means that SiC diodes can dissipate heat more effectively, reducing the need for complex cooling systems and improving the reliability of the overall system. The ability to operate at higher temperatures also allows for more compact designs, as components can be placed closer together without the risk of overheating.

3. SILICON CARBIDE (SiC) DIODES

Silicon carbide has been a focus of research and development in power electronics for several decades due to its exceptional properties as shown in Figure 1. SiC diodes are particularly well-suited for high-power and high-voltage applications, making them a popular choice in industries such as electric vehicles, renewable energy, and industrial automation

Figure 3. Packing structure of SiC power module.

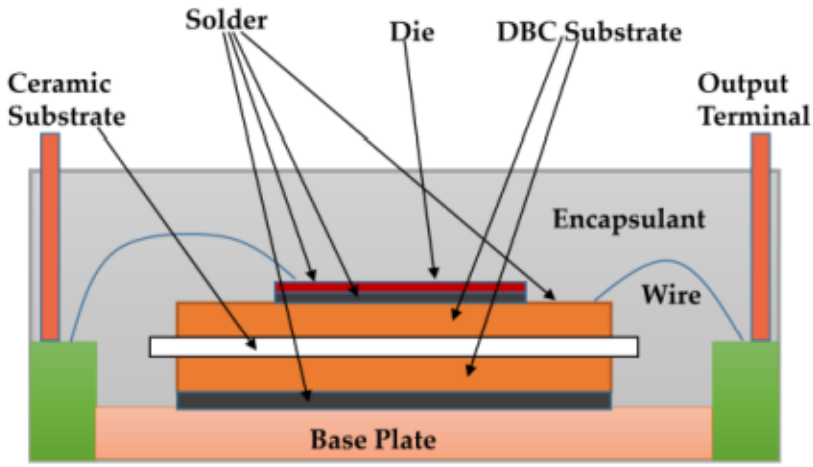

Source: (Tu et al., 2024).

3.1.Electric Vehicles

In electric vehicles, SiC diodes are used in power inverters that convert DC (direct current) from the battery into AC (alternating current) for the motor. SiC diodes' ability to operate at higher voltages and temperatures, combined with their low energy losses, allows for more efficient power conversion (Östling, Ghandi, & Zetterling, 2011). This improves the vehicle's overall energy efficiency, extending its driving range and reducing battery size as seen in Figure 3. Additionally, SiC diodes enable faster charging speeds by handling higher currents during the charging process.

3.2.Renewable Energy Systems

SiC diodes are also playing a critical role in the development of more efficient renewable energy systems. In photovoltaic (solar) inverters and wind turbine power converters, the high breakdown voltage and fast switching capabilities of SiC diodes enable better energy conversion, reducing losses and

improving the overall efficiency of these systems. This contributes to lower energy costs and more sustainable energy production (Pushpakaran, Subburaj, Bayne, & Mookken, 2016).

3.3.Industrial Automation

SiC diodes are increasingly used in industrial automation, where high-power devices such as motors, drives, and power supplies require efficient and reliable power conversion. SiC's ability to handle high voltages and temperatures makes it ideal for these demanding applications, where system reliability and efficiency are paramount (Chen & Huang, 2024).

4. GALLIUM NITRIDE (GaN) DIODES

Gallium nitride is another wide bandgap material that has gained significant attention in recent years due to its unique properties, particularly its ability to operate at high frequencies as demonstrated in Figure 4. GaN diodes are increasingly being used in applications where fast switching and high efficiency are critical, such as in telecommunications, data centers, and aerospace (Rais-Zadeh et al., 2014).

Figure 4. Si, 4H-SiC, and Wurtzite GaN critical material properties

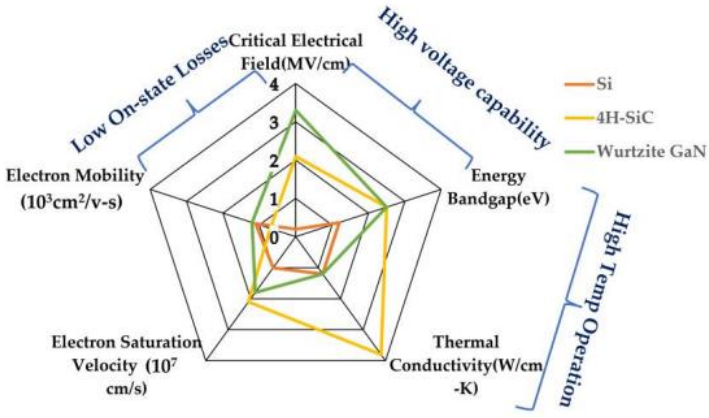

4.1.Telecommunications

GaN diodes are well-suited for high-frequency applications, making them a popular choice in telecommunications infrastructure, including base stations for 5G networks. GaN's ability to switch at high frequencies with minimal energy losses allows for more efficient signal amplification and processing, which is critical for the high-speed data transmission required in modern communication systems (Collaert, 2024).

4.2.Data Centers

In data centers, where power consumption is a major concern, GaN diodes offer a way to improve the efficiency of power supplies and reduce overall energy consumption. GaN's fast switching speeds and low losses make it possible to design more compact and efficient power supplies, helping to address the growing demand for energy-efficient data center infrastructure (Zhang, Shan, Li, Li, & Wang, 2023).

4.3.Aerospace and Defense

GaN diodes are also finding applications in aerospace and defense, where high-frequency operation and efficiency are critical for radar systems, satellite communications, and electronic warfare systems. GaN's ability to handle high-power RF signals with minimal distortion makes it ideal for these demanding applications (Raturi, Choudhuri, & Chinnamuthu, 2023).

5. KEY CHALLENGES AND FUTURE PROSPECTS

While SiC and GaN diodes offer significant advantages over traditional silicon devices, several challenges remain in their widespread adoption. One of the primary barriers is cost. WBG

materials are more expensive to produce than silicon, which has benefited from decades of investment and infrastructure development. However, as manufacturing processes improve and production volumes increase, the cost of SiC and GaN diodes is expected to decrease, making them more competitive with silicon-based devices.

Another challenge is the integration of WBG diodes into existing power systems. While SiC and GaN offer superior performance, their unique properties require careful consideration in circuit design, particularly in terms of thermal management and electromagnetic interference (EMI). Engineers must adapt to these new materials, which can increase the complexity and cost of system design.

Despite these challenges, the future of wide bandgap semiconductors is bright. As demand for high-efficiency, high-power electronics continues to grow, the advantages of SiC and GaN diodes will become increasingly important. Ongoing research is focused on improving the performance, cost, and reliability of these devices, as well as developing new applications in areas such as wireless charging, electric aviation, and energy storage.

6. CONCLUSION

Wide bandgap semiconductor diodes, particularly silicon carbide (SiC) and gallium nitride (GaN), represent a significant advancement in power electronics. Their superior properties, including higher breakdown voltages, faster switching speeds, and better thermal conductivity, make them ideal for high-power, high-frequency, and high-temperature applications. SiC diodes are already making a significant impact in electric vehicles, renewable energy, and industrial automation, while GaN diodes

are gaining traction in telecommunications, data centers, and aerospace.

Despite challenges related to cost and integration, the continued development of SiC and GaN technologies promises to revolutionize power electronics, enabling more efficient, reliable, and sustainable systems. As these materials become more affordable and widely adopted, they will play a critical role in shaping the future of industries ranging from transportation and energy to telecommunications and defense.

The emergence of wide bandgap (WBG) semiconductor diodes, particularly silicon carbide (SiC) and gallium nitride (GaN), marks a critical advancement in power electronics, enabling systems that are more efficient, compact, and reliable. These materials have far surpassed the capabilities of traditional silicon-based diodes, offering higher breakdown voltages, faster switching speeds, and superior thermal performance. These advantages are revolutionizing key industries like electric vehicles, renewable energy, telecommunications, and aerospace, where high-power, high-frequency, and high-temperature operations are essential.

SiC diodes, with their high-voltage and thermal capabilities, are driving the development of more efficient power systems in electric vehicles and renewable energy applications, contributing to greater energy efficiency and sustainability. GaN diodes, with their rapid switching and high-frequency performance, are enabling advancements in telecommunications infrastructure, data centers, and aerospace technologies, where speed and efficiency are paramount.

However, despite the remarkable progress, challenges remain. The higher cost of SiC and GaN materials compared to silicon has slowed their widespread adoption. Additionally, integrating these WBG diodes into existing systems requires

careful design considerations, particularly with regard to thermal management and circuit design. Yet, as manufacturing processes mature and production volumes increase, costs are expected to decline, enabling broader adoption.

The ongoing advancements in SiC and GaN technologies will continue to drive innovation in power electronics, shaping the future of numerous industries. These diodes are set to play an increasingly critical role in creating more efficient, reliable, and sustainable systems, supporting global efforts to reduce energy consumption and carbon emissions across a wide range of applications.

REFERENCES

Abu-Rub, H., Malinowski, M., & Al-Haddad, K. (2014). *Power electronics for renewable energy systems, transportation and industrial applications*: John Wiley & Sons.

Agarwal, S., Burgard, M., Greiner, A., & Wendorff, J. (2016). *Electrospinning*: de Gruyter.

Ballestín-Fuertes, J., Muñoz-Cruzado-Alba, J., Sanz-Osorio, J. F., & Laporta-Puyal, E. (2021). Role of wide bandgap materials in power electronics for smart grids applications. *Electronics, 10*(6), 677.

Chan, C. C., & Chau, K. (1997). An overview of power electronics in electric vehicles. *IEEE transactions on Industrial Electronics, 44*(1), 3-13.

Chen, Z., & Huang, A. Q. (2024). Extreme high efficiency enabled by silicon carbide (SiC) power devices. *Materials Science in Semiconductor Processing, 172*, 108052.

Collaert, N. (2024). Gallium nitride technologies for wireless communication. In *New Materials and Devices Enabling 5G Applications and Beyond* (pp. 101-137): Elsevier.

Iannaccone, G., Sbrana, C., Morelli, I., & Strangio, S. (2021). Power electronics based on wide-bandgap semiconductors: Opportunities and challenges. *IEEE Access, 9*, 139446-139456.

Kizilyalli, I. C., Spahn, O. B., & Carlson, E. P. (2022). Recent Progress in Wide-Bandgap Semiconductor Devices for a More Electric Future. *ECS Transactions, 109*(8), 3.

Manandhar, M. B. (2021). *Thermal Performance of AlGaN/GaN Based Power Switching Devices for Transformerless Inverters.* University of Denver,

Nguyen, N.-K., Nguyen, T., Nguyen, T.-K., Yadav, S., Dinh, T., Masud, M. K., . . . Ta, H. T. (2021). Wide-band-gap semiconductors for biointegrated electronics: Recent advances and future directions. *ACS Applied Electronic Materials, 3*(5), 1959-1981.

Östling, M., Ghandi, R., & Zetterling, C.-M. (2011). *SiC power devices—Present status, applications and future perspective.* Paper presented at the 2011 IEEE 23rd International Symposium on Power Semiconductor Devices and ICs.

Pushpakaran, B. N., Subburaj, A. S., Bayne, S. B., & Mookken, J. (2016). Impact of silicon carbide semiconductor technology in Photovoltaic Energy System. *Renewable and Sustainable Energy Reviews, 55*, 971-989.

Rafin, S. S. H., Ahmed, R., Haque, M. A., Hossain, M. K., Haque, M. A., & Mohammed, O. A. (2023). Power electronics revolutionized: A comprehensive analysis of emerging wide and ultrawide bandgap devices. *Micromachines, 14*(11), 2045.

Rafin, S. S. H., Ahmed, R., & Mohammed, O. A. (2023). *Wide band gap semiconductor devices for power electronic converters.* Paper presented at the 2023 Fourth International Symposium on 3D Power Electronics Integration and Manufacturing (3D-PEIM).

Rais-Zadeh, M., Gokhale, V. J., Ansari, A., Faucher, M., Théron, D., Cordier, Y., & Buchaillot, L. (2014). Gallium nitride as an electromechanical material. *Journal of Microelectromechanical Systems, 23*(6), 1252-1271.

Raturi, P., Choudhuri, B., & Chinnamuthu, P. (2023). Smart sensor systems for military and aerospace applications. In

Sensors for Next-Generation Electronic Systems and Technologies (pp. 239-253): CRC Press.

Ren, F., & Zolper, J. C. (2003). *Wide energy bandgap electronic devices*: World Scientific.

Roccaforte, F., Fiorenza, P., Greco, G., Nigro, R. L., Giannazzo, F., Iucolano, F., & Saggio, M. (2018). Emerging trends in wide band gap semiconductors (SiC and GaN) technology for power devices. *Microelectronic Engineering, 187*, 66-77.

Singh, S., Chaudhary, T., & Khanna, G. (2022). Recent advancements in wide band semiconductors (SiC and GaN) technology for future devices. *Silicon, 14*(11), 5793-5800.

Tu, C.-C., Hung, C.-L., Hong, K.-B., Elangovan, S., Yu, W.-C., Hsiao, Y.-S., . . . Hong, Y.-H. (2024). Industry perspective on power electronics for electric vehicles. *Nature Reviews Electrical Engineering*, 1-18.

Van Do, T., Trovão, J. P. F., Li, K., & Boulon, L. (2021). Wide-bandgap power semiconductors for electric vehicle systems: Challenges and trends. *IEEE Vehicular Technology Magazine, 16*(4), 89-98.

Zhang, Y., Shan, K., Li, X., Li, H., & Wang, S. (2023). Research and Technologies for next-generation high-temperature data centers–State-of-the-arts and future perspectives. *Renewable and Sustainable Energy Reviews, 171*, 112991.

FİZİK

yaz
yayınları

YAZ Yayınları
M.İhtisas OSB Mah. 4A Cad. No:3/3
İscehisar / AFYONKARAHİSAR
Tel : (0 531) 880 92 99
yazyayinlari@gmail.com • www.yazyayinlari.com